Part III

Shock Capturing Numerical Methods and Simulations of Free Surface Flow of Shallow Avalanches Over Curved & Twisted Channels

Chapter 6

High Resolution Shock-Capturing Numerical Methods

6.1 Solutions of the Model Equations

There are two fundamental aspects of research in science and technology. The first one is to understand the physics and nature of any physical phenomena and put it into a proper form as a number of mathematically expressible closed systems of equations. A system is commonly called a *model*. With the model equations at hand, in the form of equations of motion, the next important step is to *solve* them. Both steps are equally significant from a physical point view to applications in real life problems. There are three main ways of solving a set of model equations.

6.1.1 A Complete Analytical Solution

First, one would try to solve the full set of model equations involving all principal parameters (phenomenological, topographic and possibly others) and boundary and initial values. Such a solution, if we are able to compute it analytically and explicitly, is superior to all possible solutions because analytical solutions provide qualitative insight and usually enhance the physical understanding. Unfortunately, construction of analytical solutions is often almost impossible, at least for complicated geophysical flows. This is the actual case in the formulation of the original SH-theory and all of its further extensions [31, 34, 35, 46, 47, 48, 49, 51, 67, 86, 98, 99, 100, 101, 112, 113, 131]. This is clearly due to the complicated non-linear partial differential equations and the moving boundary conditions which together describe the dynamic behaviour of flow avalanches ranging from simple to complicated topographies. One must find a way to escape from this complication.

6.1.2 A Particular Solution

Due to nonlinearity special numerical techniques are required to solve the full system of hyperbolic equations presented in the last three Chapters. However, exact analytical solutions can be obtained for some special and significant cases to gain insight to the full system. Such special exact analytical solutions are important in three respects: (i) they can in many cases predict phenomena observable in nature, (ii) they help in comparing

with results obtained from other existing models and (*iii*) they are crucial to test the efficiency and applicability of numerical solutions.

In this second step one should simplify the complicated equations by some means, e.g. by substituting some typical values for the parameters, by considering the problem for some particular situation like steady state and homogeneous flow or by decreasing the dimension of the problem. In such a situation, one may then find exact analytical solutions of some particular type. Although this kind of solutions cannot describe the flow behaviour in a full form, they still are important to provide some qualitative insight into the behaviour of such flows. Furthermore, they may be useful to analyse numerical schemes. However, we are not going to discuss such particular solutions in this thesis. For detailed study on it we refer to IVERSON et al., PUDASAINI et al. and TAI [16, 55, 56, 98, 99, 105, 121].

6.1.3 Numerical Solution

Third, and today probably most popular and convenient, one seeks to solve the complicated system of equations by numerical techniques. With the growing development of hardware and software and with the rapid increase of numerical and scientific computing techniques this method became the dominant approach in analysing systems *expressible in standard mathematical form*. This is no different for the SH-theory. Its original equations [112] and all of its further developments have successfully been solved by applying different numerical techniques, and the results were tested against reliable indoor and outdoor laboratory experiments as well as natural events like avalanches, debris- and mud-flows and rockslides, and from good to excellent agreement was found between them, see e.g., [31, 32, 105, 131]. These procedures are so important in the development of the theory that we will discuss the numerical techniques and the experiments in detail in separate Chapters.

6.1.4 Numerical Difficulties

The governing depth-integrated equations presented at the end of Chapters 3, 4 and 5 can be solved numerically by using finite difference or other advanced numerical methods for several initial conditions and parameter values. Although these equations seem to be similar to the nonlinear shallow-water wave equations, their numerical integration in fact turns out to be quite troublesome. There are several reasons for that:

- When a pile of granular material is released from rest on a slope, often the material near the rear end tends initially to move up the slope. Similarly in the deposition at the rear end material is still approaching the deposited mass; often parts of the mass at the rear end moves backwards before it comes to a rest.

- Because the motion is dominantly advective and the convective acceleration terms decide critically about the stability of a numerical scheme we must be careful to use appropriate numerical schemes (e.g., upwinding in the EULERIAN finite discretisation) to avoid numerical instabilities.

- The SH-equations or their extensions are very close in structure to the water wave equations, but the geometries of the avalanches are different from those of the usual

water wave problem. Unlike the analogous water-wave problem, the material is in contact with the bed over a small portion of the bed, and the depth is zero elsewhere.

- The flow of a granular mass can be regarded as a moving interface and it embodies all the associated difficulties of such problems.

The major concern of this and the following chapter is the development of appropriate numerical methods that can solve our model equations in an excellent way.

6.2 Appropriate Numerical Modelling

In all the theories presented in Chapters 3, 4 and 5, the governing equations comprise of a *hyperbolic* system in three variables, the avalanche thickness and velocity components in the down slope and cross slope directions which are very similar to one another for the various geometric configurations. Thus, common principal integration schemes can with advantage be used for all. In the following chapters, we shall demonstrate this for different geometries illustrated in the previous chapters. In the past decade numerical techniques were developed to solve the SAVAGE-HUTTER-equations for typical moving boundary value problems of granular flows as illustrated in Figs. 3.5, 3.6 and 3.7 . These techniques are based on LAGRANGIAN *moving mesh finite-difference schemes*. In these LAGRANGIAN schemes *explicit artificial numerical diffusion was incorporated to maintain stability*. In doing so the quality of resolution deteriorates. In fact, the adequacy of these numerical solutions can be "challenged" because of uncontrolled spreading due to this diffusion. Without adding extra artifical diffusion the formation of the shock resulted in numerical instabilities of the LAGRANGIAN moving grid technique [67, 131]. This also occurs for an EULERIAN integration technique if the central difference scheme is employed [130]. Other traditional high-order difference methods with the EULERIAN representation are likewise susceptible to numerical instabilities and cause non-physical oscillations in regions of large gradients of the variables [129]. The usual way to deal with these types of instabilities and oscillations is also to incorporate artificial diffusion into the numerical scheme. However, if this is applied uniformly over the problem domain, and sufficient diffusion is added to dampen spurious oscillations, then the solution is smeared out elsewhere. Although traditional first-order finite difference methods, e.g. the upstream schemes, are monotonic and stable, due to inherent numerical diffusion, they are strongly dissipative, causing the solution to become also smeared out and often grossly inaccurate.

Successful modelling of strongly convective hyperbolic equations is one of the most challenging problems in computational fluid mechanics, particularly when large gradients of the physical variables occur, e.g. for a moving front or possibly arising shock waves in a granular avalanche. Shock formation is an essential mechanism in granular flows on an inclined surface merging into a horizontal run-out zone or encountering an obstacle when the velocity becomes subcritical from its supercritical state. It is therefore natural to apply conservative high-resolution numerical techniques that are able to resolve the steep gradients and moving fronts, often observed in experiments and field events but not captured by the LAGRANGIAN finite difference scheme and traditional EULERIAN finite difference schemes. The development of high-resolution shock-capturing schemes has a long history, see e.g. [68, 74, 121, 122, 124, 125, 130, 132]. We choose a recent high-resolution approach,

namely the non-oscillatory central (NOC) schemes first introduced by Nessyahu & Tadmor [85], in which different cell reconstruction techniques – the TVD (Total Variation Diminishing) limiters [74] and an ENO (Essentially Non-Oscillatory) cell reconstruction scheme [38] – are applied, respectively. The numerical results obtained with the high-resolution schemes and the traditional finite difference schemes are compared. Of the numerical methods under consideration here the NOC scheme with the Minmod limiter demonstrates to be the most suitable to handle the problem of avalanche dynamics.

In this Chapter we will develop some high resolution numerical methods that can essentially capture shock phenomena encountered in geophysical flows like avalanches and debris movements over simple curved chutes in the laboratory as well as over complex non-trivial natural terrains.

6.3 Traditional Numerical Methods

In this section we will present some traditional numerical schemes that are used in different literatures to solve hyperbolic systems of equations. We will also point out why these schemes are not appropriate in our case that leads to the development of high-order shock-capturing numerical methods.

6.3.1 First Order Schemes

We start with a very simple case of a one-dimensional conservative equation. For simplicity, the x-t plane of time and space will be discretised by choosing an uniform and stationary mesh width $\triangle x$ and a time step $\triangle t$. However, most methods presented in this thesis are extendable to variable mesh grids. The discrete *mesh points* will be denoted by $(x_j,\, t^n)$ and are defined as

$$x_j = j\triangle x, \quad j = 0,\, 1,\, 2, \ldots; \quad t^n = n\triangle t, \quad n = 0,\, 1,\, 2, \ldots, \tag{6.1}$$

where the mesh cell x_j is bounded by the boundaries $x_{j-1/2}$, $x_{j+1/2}$ and $x_{j+1/2} = x_j + \triangle x/2$.

For a systematic development of numerical schemes, we start with a homogeneous linear scalar advection hyperbolic conservation law

$$\frac{\partial w}{\partial t} + a\frac{\partial w}{\partial x} = 0, \tag{6.2}$$

where a is a constant. The second term $a\partial w/\partial x$ represents a *flux derivative* $\partial f/\partial x = a\partial w/\partial x$, with the *physical flux* $f = aw$, where w is a conservative variable. Equation (6.2) is discretised by integrating it over the space-time rectangle $[x_{j-1/2},\, x_{j+1/2}] \times [t^n,\, t^{n+1}]$ to obtain

$$\int_{x_{j-1/2}}^{x_{j+1/2}} w(x,\, t^{n+1})\,\mathrm{d}x = \int_{x_{j-1/2}}^{x_{j+1/2}} w(x,\, t^n)\,\mathrm{d}x - \int_{t^n}^{t^{n+1}} \left\{ f(x_{j+1/2},\, t) - f(x_{j-1/2},\, t) \right\} \mathrm{d}t. \tag{6.3}$$

All the schemes that we will present in the sequel will be expressed in terms of the *spatial and temporal mean values* of the conservative variable w and physical flux function f. For

this reason we define these mean values, respectively, as follows

$$U_j^n = \frac{1}{\triangle x}\int_{x_{j-1/2}}^{x_{j+1/2}} w(x,\, t^n)\,\mathrm{d}x, \qquad \mathcal{F}(U;\, j+1/2) = \frac{1}{\triangle t}\int_{t^n}^{t^{n+1}} f(x_{j+1/2},\, t)\,\mathrm{d}t. \tag{6.4}$$

With this definition equation (6.3) reduces to the following discretisation in general form

$$U_j^{n+1} = U_j^n - \frac{\triangle t}{\triangle x}\left\{\mathcal{F}(U;\, j+1/2) - \mathcal{F}(U;\, j-1/2)\right\}, \tag{6.5}$$

where $\mathcal{F}(U;\, j \pm 1/2)$ denote the *numerical flux functions* which are functions of the cell averages of the neighbouring cells on the cell boundaries at $x_{j+1/2}$ and $x_{j-1/2}$, respectively . We will show in the sequel that *these numerical fluxes may have different forms depending on the order of accuracy and types of interpolation.* If the cell averages in the numerical flux function are taken at the time level t^n, one obtains an explicit numerical scheme. This allows to determine U^{n+1} explictly, whereas using cell averages at time level t^{n+1} results in an implicit method. Although implicit methods are useful in solving other types of partial differential equations, they are rarely used for time-dependent hyperbolic equations. In this thesis we will only consider explicit methods. In the following derivations we will set a to be positive, unless otherwise stated explicitly. First, we discuss a first-order scheme.

Upwind-Method

From the initial data $w_0(x) = w(x, t = 0)$ we define the data U^0 for the approximate solution as

$$U_j^0 = w_j^0(x). \tag{6.6}$$

This value can also be defined by cell averages $U_j^0 = \overline{w}_j^0(x)$. We then use a *time-marching procedure* to construct the approximation U^{n+1} from U^n and so on, in a several-levels method. There is a wide variety of finite difference methods that can be used. In many cases the derivatives occurring in (6.2) may simply be replaced by appropriate finite difference approximations, for example, utilising the *low order upwind flux* approximations

$$\mathcal{F}^{UW}(U; j+1/2) = aU_j^n, \quad \mathcal{F}^{UW}(U; j-1/2) = aU_{j-1}^n. \tag{6.7}$$

For these numerical flux functions (6.5) results in the following (low) first-order *upwind* method

$$U_j^{n+1} = U_j^n - \nu(U_j^n - U_{j-1}^n), \tag{6.8}$$

where $\nu = a\triangle t/\triangle x$.

Many of the high-resolution schemes for the approximation of the one-dimensional system of conservation laws are based on upwind differencing. If the conservation law is nonlinear, a more complex situation occurs, particularly, when there is a mixture of both right-going and left-going waves. In this case we need to identify the direction of the wind. The upwind method has the advantage, that it does not result in any spurious oscillation near a discontinuity but it is only of first order accuracy. As we will see later, unphysical oscillations in numerical solutions as obtained with central differences may not be encountered with the upwind method, but such schemes lead to large numerical diffusion in time-dependent problems.

6.3.2 Second-Order Schemes

Lax-Wendroff Method

A large number of second-order methods can be developed to solve the linear system (6.2) by using different finite difference approximations. Most of them are directly based on finite difference approximations of the model equations with the exception of the Lax-Wendroff method. This method is based on the Taylor series expansion of the conservative variable, in which the numerical fluxes are given by

$$\mathcal{F}(U; j+1/2) = a\, U^{n+1/2}_{j+1/2}, \qquad \mathcal{F}(U; j-1/2) = a\, U^{n+1/2}_{j-1/2}. \tag{6.9}$$

Applying Taylor series expansion and retaining only the first order terms, and using the conservation law (6.2) yields

$$w^{n+1/2}_{j+1/2} = w^n_j + \frac{\triangle x}{2}\,(\partial w/\partial x)^n_j + \frac{\triangle t}{2}\,(\partial w/\partial t)^n_j = w^n_j + \frac{\triangle x}{2}\,(\partial w/\partial x)^n_j - \frac{a\triangle t}{2}\,(\partial w/\partial x)^n_j\,. \tag{6.10}$$

By virtue of (6.10) and using central differences, the value of $U^{n+1/2}_{j+1/2}$ for the numerical flux (6.9) is approximated by

$$U^{n+1/2}_{j+1/2} = U^n_j + \frac{1}{2}\left(U^n_{j+1} - U^n_j\right) - \frac{a\triangle t}{2\triangle x}\left(U^n_{j+1} - U^n_j\right) = \frac{1}{2}\left(U^n_{j+1} + U^n_j\right) - \frac{\nu}{2}\left(U^n_{j+1} - U^n_j\right), \tag{6.11}$$

where $\nu = a\Delta t/\Delta x$. Substituting (6.9) and (6.11) into (6.5) yields the Lax-Wendroff scheme in central difference form,

$$U^{n+1}_j = U^n_j - \frac{\nu}{2}\left(U^n_{j+1} - U^n_{j-1}\right) + \frac{\nu^2}{2}\left(U^n_{j+1} - 2U^n_j + U^n_{j-1}\right). \tag{6.12}$$

The Taylor series expansion of the form (6.12) at x_j implies that the Lax-Wendroff method is of second order accuracy in space. Thus, from (6.9) and (6.11) the numerical flux in (6.12) is viewed as the *high order* Lax-Wendroff *flux*,

$$\mathcal{F}^{LW}(U; j+1/2) = \frac{a}{2}(U^n_{j+1} + U^n_j) - \frac{a\nu}{2}(U^n_{j+1} - U^n_j). \tag{6.13}$$

Upwind Beam-Warming Method

This is a one-sided version of the Lax-Wendroff method. This is a high (second) order approximation method with,

$$U^{n+1}_j = U^n_j - \nu\left(U^n_j - U^n_{j-1}\right) - \frac{\nu}{2}(1-\nu)\left(U^n_j - 2U^n_{j-1} + U^n_{j-2}\right), \tag{6.14}$$

in which the numerical fluxes are defined in the same way as in (6.9) but the value of $U^{n+1/2}_{j+1/2}$ is approximated by using (6.10) with an upwind (so one sided) method, i.e.

$$U^{n+1/2}_{j+1/2} = U^n_j + \frac{1}{2}\left(U^n_j - U^n_{j-1}\right) - \frac{a\triangle t}{2\triangle x}\left(U^n_j - U^n_{j-1}\right) = U^n_j + \frac{1}{2}\left(U^n_j - U^n_{j-1}\right) - \frac{\nu}{2}\left(U^n_j - U^n_{j-1}\right). \tag{6.15}$$

All of the methods discussed so far are 2-level methods. For time-dependent conservation laws, 2-level methods are exclusively used. Higher level methods involve additional difficulties, see [74].

Problems with Traditional Schemes

It is well known that traditional second-order central difference methods introduce dispersive effects that lead to unphysical oscillations in the numerical solution for physical problems with large gradients of variables. For hyperbolic equations it is often the case that the numerical oscillations are so large that a stable simulation may not be reached. For such cases, in order to avoid possible (emerging) instabilities or to suppress numerical oscillations to an "acceptable level", certain artificial diffusion must be incorporated. In order to avoid the above problem non-centered upstream difference schemes may be used. However, this introduces alternative difficulties – implicit numerical diffusion.

6.4 Modern Numerical Methods

6.4.1 Total Variation Diminishing Method

Although first-order finite difference methods are monotonous and stable, they are also strongly numerically diffusive, causing the solution to become smeared out. Second-order or higher-order techniques are less dissipative, but susceptible to non-linear, numerical instabilities that cause *non-physical oscillations. The high-resolution methods are a compromise between the traditional first-order and higher-order difference schemes.* Their central idea is, on the one hand, to avoid the introduction of under- and over-shoots (numerical oscillation), and on the other hand, *to maintain the numerical diffusion as small as possible*, that is often achieved by different cell reconstruction techniques.

It is well known that in computing discontinuous solutions the first order method (upwind) gives very smeared solutions while the second order method (Lax-Wendroff or Beam-Warming) gives spurious oscillations (e.g., LeVeque [74]). In order to develop a method that is of higher order and at the same time non-oscillatory and capable of capturing shocks, we need to define a powerful concept called the *Total Variation Diminishing* method.

We define the *total variation* of the mean value U^n as

$$TV(U^n) = \sum_{j=0}^{N-1} |U^n_{j+1} - U^n_j|. \tag{6.16}$$

Any oscillation in the computed result increases the total variation (TV). The *Total Variation Diminishing* condition

$$TV(U^{n+1}) \leq TV(U^n) \tag{6.17}$$

provides a method that gives a solution without spurious oscillations near the discontinuities. Any numerical scheme which fulfils the TVD condition (6.17) for all grid functions U^n is called a *Total Variation Diminishing* (TVD) method. Therefore, any TVD method is automatically *monotonicity preserving.* This means, in particular, that oscillations of the physical quantities like velocity jumps and other sharp gradients can not arise near an isolated propagating discontinuity. As we will see later, another beautiful feature of the TVD requirement is that it is possible to derive higher-order accurate methods that also satisfy (6.17). It can also be shown that the true (i.e., physically relevant weak) solution to a scalar conservation law possesses this TVD property, see [74].

General Criterion for a TVD Method

Let us consider a general two-sided numerical scheme of the form

$$U_j^{n+1} = U_j^n - C_{j-1/2}\left(U_j^n - U_{j-1}^n\right) + D_{j+1/2}\left(U_{j+1}^n - U_j^n\right), \tag{6.18}$$

in which $C_{j-1/2}$ and $D_{j+1/2}$ are data-dependent expressions. The scheme (6.18) is a TVD method if the following conditions are satisfied

$$0 \le C_{j-1/2}, \quad 0 \le D_{j+1/2}, \quad 0 \le C_{j-1/2} + D_{j+1/2} \le 1, \quad \text{for all } j. \tag{6.19}$$

For a proof, see HARTEN, [38]. For example, the low order upwind scheme (6.8) is a TVD method under the COURANT-FRIEDRICHS-LEVY (CFL) condition $|a\triangle t/\triangle x| < 1$, [12, 13], since in an upwind scheme $C_{j-1/2} = \nu = a\triangle t/\triangle x \in [0,\, 1)$ and $D_{j+1/2} = 0$, which satisfy conditions (6.19).

6.4.2 Second Order TVD Schemes

In the sequel we would like to develop some numerical methods that are second order accurate for smooth solutions and yet give well resolved, non-oscillatory discontinuities. The major roles are played by the TVD flux-limiters and TVD slope-limiters.

Flux-Limiter Methods

In order to achieve better resolution of the solutions of hyperbolic conservation equations we can couple a heigh-order flux $\mathcal{F}_H$ (e.g., some central difference methods) that works well in the smooth regions and a low-order flux $\mathcal{F}_L$ (e.g., some monotone methods) that behaves well in the vicinity of discontinuities. The structure of this *coupling*, F say, should be such that F reduces to $\mathcal{F}_H$ for the smooth part of the solution and to $\mathcal{F}_L$ for the discontinuous part of the solution. In this section we couple a (low) first-order upwind scheme with the (high) second-order LAX-WENDROFF scheme with the aid of a flux limiter.

The LAX-WENDROFF scheme (6.12) can be rewritten as

$$U_j^{n+1} = U_j^n - \nu\left(U_j^n - U_{j-1}^n\right) - \frac{\nu}{2}(1-\nu)\left(U_{j+1}^n - 2U_j^n + U_{j-1}^n\right), \tag{6.20}$$

which demonstrates that the *high order* LAX-WENDROFF *flux*, $\mathcal{F}_H$, can be viewed as consisting of the low order upwind flux, $\mathcal{F}_L$ plus a LAX-WENDROFF *correction* $(\mathcal{F}_H - \mathcal{F}_L)$

$$\mathcal{F}_H = \mathcal{F}_L + (\mathcal{F}_H - \mathcal{F}_L). \tag{6.21}$$

The first term on the right-hand side of this equation, $\mathcal{F}_L$, corresponds to the first order upwind scheme (6.8) and thus results in very diffusive solutions. Whereas the correction term, $(\mathcal{F}_H - \mathcal{F}_L)$, is referred as an anti-diffusive flux (SWEBY, [120]), since it will be utilised to act as an agent to capture discontinuities. The low order flux $\mathcal{F}_L$ contains too much diffusion which must be compensated by the correction term $(\mathcal{F}_H - \mathcal{F}_L)$, but this correction must somehow be *controlled* physically, e.g., by a TVD flux-limiter.

Since the upwind method possesses the TVD property at discontinuities, by virtue of

(6.21) one can define a method that enjoys the TVD property at discontinuities and holds second order accuracy on smooth solutions by introducing a *flux-limiter* ϕ_j, that is

$$F = \mathcal{F}_L + \phi_j \left\{ \mathcal{F}_H - \mathcal{F}_L \right\}. \tag{6.22}$$

The flux-limiter $\phi_j = \phi(U; j)$ is chosen near unity if the data U is smooth near U_j, and close to zero when there is a rapid change of the data around U_j. This means that the value of ϕ_j is exclusively determined by the smoothness of the data for which there exists several ways. One possibility is to observe the behaviour of the ratio of the consecutive gradients, θ_j,

$$\phi_j = \phi(\theta_j), \qquad \theta_j = \frac{U_j^n - U_{j-1}^n}{U_{j+1}^n - U_j^n}, \tag{6.23}$$

where θ_j can be seen as a *measure of the smoothness* of the solution. This definition is a natural choice to achieve an approximate TVD condition as we will immediately see below. Notice that this measurement breaks down near the extreme points of U, when the denominator is close to zero and $|\theta_j|$ becomes arbitrarily large or negative even if the solution is smooth.

Remark: *There are some disadvantages of the TVD method. One of them is that one can not maintain second order accuracy at extreme points. At these points the method is only first order accurate. Thus, TVD methods must degenerate to first order accuracy at extreme points.*

Hybridisation Between Upwind and Lax-Wendroff Methods

Now, we will establish a condition on the flux-limiter ϕ_j which must be satisfied so that a hybrid approach between the upwind and Lax-Wendroff methods agrees with the TVD requirement (6.17). Let us consider the combination of first-order upwind and second-order Lax-Wendroff methods. The limited-flux can be written in combination with the flux-limiter as

$$F(U; j+1/2) = aU_j^n + \frac{1}{2}a(1-\nu)(U_{j+1}^n - U_j^n)\phi_j, \tag{6.24}$$

where $\phi_j = \phi_j^{LW} = 1$ indicates the Lax-Wendroff method (6.13). By inspection of (6.14) and (6.24) it follows that $\phi_j^{BW} = \theta_j = (U_j^n - U_{j-1}^n)/(U_{j+1}^n - U_j^n)$ for the Beam-Warming scheme. This is the reason why we have defined the flux-limiter by (6.23). Substituting (6.24) into (6.5) yields

$$\begin{aligned} U_j^{n+1} &= U_j^n - \nu\left(U_j^n - U_{j-1}^n\right) - \frac{\nu}{2}(1-\nu)\left\{\left(U_{j+1}^n - U_j^n\right)\phi_j - \left(U_j^n - U_{j-1}^n\right)\phi_{j-1}\right\} \\ &= U_j^n - C_{j-1}\left(U_j^n - U_{j-1}^n\right) + D_j\left(U_{j+1}^n - U_j^n\right), \end{aligned} \tag{6.25}$$

where

$$C_{j-1} = \nu - \frac{\nu}{2}(1-\nu)\phi_{j-1}, \quad D_j = -\frac{\nu}{2}(1-\nu)\phi_j. \tag{6.26}$$

Formula (6.25) is a TVD method if it satisfies the TVD conditions (6.19). However, this is not the case here since $D_j < 0$ for $\phi_j > 0$. Therefore, we must find some conditions on ϕ_j such that the constraints in (6.19) are satisfied with some manipulation of (6.25). For this reason we rewrite (6.25) in an equivalent form

$$U_j^{n+1} = U_j^n - C'_{j-1}(U_j^n - U_{j-1}^n) + D'_j(U_{j+1}^n - U_j^n), \tag{6.27}$$

where the coefficients of the scheme are given by

$$C'_{j-1} = \nu + \frac{\nu}{2}(1-\nu)\left\{\frac{(U^n_{j+1}-U^n_j)\phi_j - (U^n_j - U^n_{j-1})\phi_{j-1}}{U^n_j - U^n_{j-1}}\right\}, \quad D'_j = 0. \tag{6.28}$$

The TVD condition (6.19) is satisfied by (6.28) under the restrictions

$$0 \le C'_j \le 1, \quad \text{for all} \quad j. \tag{6.29}$$

Condition (6.29) is satisfied provided the following holds true together with the CFL condition $|\nu| \le 1$:

$$\left|\frac{\phi(\theta_j)}{\theta_j} - \phi(\theta_{j-1})\right| \le 2, \qquad \text{for all} \quad \theta_j,\, \theta_{j-1}. \tag{6.30}$$

The requirement (6.30) is satisfied only if the following two inequalities hold

$$0 \le \frac{\phi(\theta_j)}{\theta_j} \le 2 \quad \text{and} \quad 0 \le \phi(\theta_j) \le 2, \quad \text{for all} \quad \theta_j. \tag{6.31}$$

Here comes the critical weakness of the TVD method. If $\phi_j \le 0$ then the slopes at the neighbouring points have opposite signs. This consequently implies the fact that the data then has an extremum near U_j. The total variation certainly increases if the values at such points are accounted for. For this reason, the following condition is imposed to be at a safe position

$$\phi_j = \phi(\theta_j) = 0, \quad \text{for} \quad \theta_j \le 0, \tag{6.32}$$

and use the upwind method alone.

Remark: *It is impossible to satisfy both the higher order accuracy and the* TVD *requirement at the critical grid-values where $\phi_j < 0$. The only way out is that the higher (second) order accuracy requirement must be given up at these critical grid-values. However, any difference scheme with formal higher (second) order accuracy at all but these critical points may be understood as having higher (second) order resolution in the sense that the local truncation error is of order $\mathcal{O}(\Delta x)^3$ almost everywhere, and the overall higher (second) order accuracy does not seem to be degraded in these cases, at least in the L^1-norm, see [85].*

Remark: *On the other hand, this is a weak point of the* TVD *method since if the data is smooth near the extremum one is alway tempted to take the value of the flux limiter to be unity in order to use a high order method. However, in doing so the total variation will generally increase and everything breaks down.*

Fig. 6.1a displays the region for condition (6.31) to be satisfied. The line $\phi(\theta) = 1$ denotes the Lax-Wendroff method and $\phi(\theta) = \theta$ indicates the second order upwind Beam-Warming method. Only a part of these two lines lies in the TVD-region, so both the Lax-Wendroff and Beam-Warming methods do not possess the TVD-property, in general.

The best choice for ϕ is the convex combination of the ϕ^{LW} for the Lax-Wendroff, which is simply $\phi = 1$, and the ϕ^{BW} for the Beam-Warming, which is $\phi = \theta$ as follows

$$\phi(\theta) = (1-\psi(\theta))\,\phi^{LW} + \psi(\theta)\phi^{BW} = 1 + \psi(\theta)(\theta - 1), \quad \text{for } 0 \le \psi(\theta) \le 1. \tag{6.33}$$

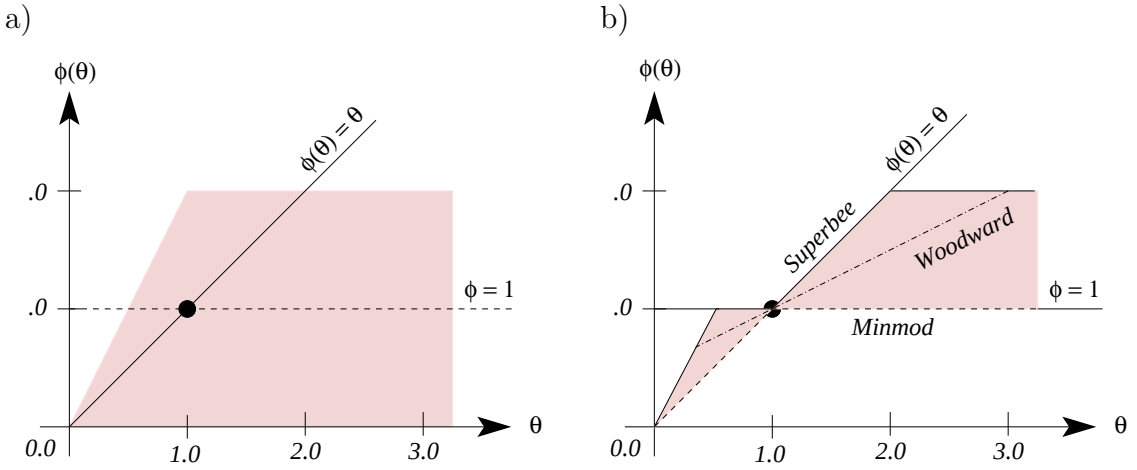

Figure 6.1: a) Region of values which $\phi(\theta)$ can take to possess the TVD property. b) Region of values $\phi(\theta)$ for the second order TVD methods, where the Superbee limiter (solid line) is on the upper boundary, the Minmod limiter (dashed line) lies on the lower boundary and the Woodward limiter (dotted line) lies between them.

With conditions (6.31) and (6.33) SWEBY [120] showed that for second order TVD, $\phi(\theta)$ is confined to lie in the region shown in Fig. 6.1b. Note that the condition $\phi(1) = 1$ is automatically imposed, which indicates that the method is of second order accuracy for $\theta = 1$, i.e., the data is smooth.

Some Special Limiters

There is no hard rule for the quantitative selection of the flux limiter $\phi(\theta)$ and it depends on the particular problem at hand. Nevertheless, its value must lie in a certain $\theta - \phi$ diagram. If $\phi(\theta)$ is defined by the lower boundary of the "second order TVD region", it results in the so-called *Minmod* limiter,

$$^{Minmod}\phi(\theta) = \max(0,\, \min(1,\, \theta)), \tag{6.34}$$

whilst the *Superbee* limiter

$$^{Superbee}\phi(\theta) = \max(0,\, \min(1,\, 2\theta),\, \min(\theta,\, 2)) \tag{6.35}$$

is obtained if $\phi(\theta)$ is defined by the upper boundary of the second order TVD region. The *Woodward* limiter lies between them

$$^{Woodward}\phi(\theta) = \max\left(0,\, \min(2,\, 2\theta,\, 0.5(1+\theta))\right). \tag{6.36}$$

Fig. 6.1b illustrates the values of $\phi(\theta)$ against θ for these three limiters. Since $\phi(\theta)$ determines the value of the *anti-diffusion flux*, different limiters result in different diffusion. The Superbee limiter which lies on the upper boundary of the second order TVD region causes the least diffusion. The Minmod limiter is the most diffusive one. The Woodward limiter lies between them. In fact, the Superbee limiter is not only the least diffusive, it is often anti-diffusive and hence has a tendency to steepen gradients of field variables, as we will see from the corresponding numerical results in Chapter 8. The application of these slope limiters can eliminate unwanted oscillations and gives second-order accurate reconstruction for the smooth solutions (except near critical points) over the cell. One can

therefore develop high-order resolution schemes without spurious oscillations, but with the ability to capture a possible discontinuity.

These limiters should be selected according to the physical diffusivity of the problem. For example, if we consider a linear advection hyperbolic RIEMANN problem with constant coefficient, we must select the most anti-diffusion flux limiter because from the exact analytical solution we know that the initial geometry is advecting with time along the characteristic direction *making the discontinuity undistorted*. As we will see in Chapter 8 while dealing with the computational results, large-scale geophysical flows like avalanches and debris flows can not produce so strong and sharp geometry as in the case of the aforementioned RIEMANN problem. Nevertheless, we must choose the most diffusive-flux, i.e., Minmod. Many other different limiters can be found in e.g., YEE [132], but we are not going to discuss them all.

6.4.3 Cell Reconstruction with Slope Limiters

We define now a so-called "slope-limiter" which is an analog of the flux-limiter defined in (6.23). These slope-limiters are designed in such a way that certain numerical schemes hold the TVD property under appropriate piecewise linear cell reconstructions.

In the above considerations we assumed $a > 0$. For $a < 0$, a similar method can be defined by again viewing LAX-WENDROFF as a modification of the upwind method which is then one-sided in the opposite direction. A mathematically pleasing property is that we can unify these two methods into a single formula. This, to a great extent, helps in generalising the method to linear systems of equations and non-linear problems. Because in more general cases both negative and positive wave speeds can exist simultaneously, we now unconfine the sign of a. So, for a of either sign, the fluxes of the upwind and LAX-WENDROFF methods can be written as

$$\mathcal{F}^{UW}(U; j+1/2) = \tfrac{1}{2}a(U^n_{j+1} + U^n_j) - \tfrac{1}{2}|a|(U^n_{j+1} - U^n_j), \tag{6.37}$$

$$\mathcal{F}^{LW}(U; j+1/2) = \tfrac{1}{2}a(U^n_{j+1} + U^n_j) - \tfrac{1}{2}a\nu(U^n_{j+1} - U^n_j). \tag{6.38}$$

Introducing the flux-limiter as in (6.22) the TVD flux for the LAX-WENDROFF method is given by

$$F(U; j+1/2) = \mathcal{F}^{UW}(U; j+1/2) + \tfrac{1}{2}\phi_{j'}a(\mathrm{sgn}(\nu) - \nu)(U^n_{j+1} - U^n_j). \tag{6.39}$$

This is analogous to (6.24). The flux limiter $\phi_{j'}$ is used to determine the value of F at $x_{j+1/2}$, and $\theta_{j'}$ depends on the sign of the characteristic speed a. For both signs of a we can define $\phi_{j'}$ as

$$\phi_{j'} = \phi(\theta_{j'}), \quad \text{with} \quad \theta_{j'} = \frac{U^n_{j_a+1} - U^n_{j_a}}{U^n_{j+1} - U^n_j}, \qquad j_a = j - \mathrm{sgn}(a). \tag{6.40}$$

For $a > 0$ and $a < 0$ the TVD flux (6.39) can be realised, respectively, as follows

$$\begin{aligned} F(U; j+1/2) &= a\left\{U^n_j + \frac{1}{2}(U^n_{j+1} - U^n_j)\phi_j - \frac{\nu}{2}(U^n_{j+1} - U^n_j)\phi_j\right\} \\ &= a\left\{U^n_j + \frac{\triangle x}{2}\frac{(U^n_{j+1} - U^n_j)}{\triangle x}\phi_j - \frac{\nu\triangle x}{2}\frac{(U^n_{j+1} - U^n_j)}{\triangle x}\phi_j\right\}, \end{aligned} \tag{6.41}$$

$$
\begin{aligned}
F(U; j+1/2) &= a\left\{U^n_{j+1} - \frac{1}{2}(U^n_{j+1} - U^n_j)\phi_{j'} - \frac{\nu}{2}(U^n_{j+1} - U^n_j)\phi_{j'}\right\} \\
&= a\left\{U^n_{j+1} - \frac{\triangle x}{2}\frac{(U^n_{j+1} - U^n_j)}{\triangle x}\phi_{j'} - \frac{\nu\triangle x}{2}\frac{(U^n_{j+1} - U^n_j)}{\triangle x}\phi_{j'}\right\}. \quad (6.42)
\end{aligned}
$$

The oscillations arising in the LAX-WENDROFF scheme can be interpreted geometrically as being caused by a poor choice of slopes between two grid values. This leads to a piecewise linear reconstruction $\tilde{u}^n(x, t_n)$ with *much larger* total variation *than in the given data* U^n. This can be remedied by defining a "slope-limiter". Let us first consider a reconstruction of the cell values by a piecewise linear function of the form

$$\tilde{u}^n(x, t_n) = U^n_j + \sigma_j(x - x_j), \quad \text{on the cell} \quad [x_{j-1/2}, x_{j+1/2}]. \quad (6.43)$$

The slope σ_j in this equation is based on the data U^n. It can be seen easily that for any choice of the slope σ_j the mean value of the cell average $\tilde{u}^n(x, t_n)$ over $[x_{j-1/2}, x_{j+1/2}]$ is equal to the data point U^n_j. The most significant question is the choice of an appropriate slope σ_j which will greatly influence the numerical results of the scheme.

This makes it possible to introduce the *slope limiter* σ_j,

$$\sigma_j = \left(\frac{U^n_{j+1} - U^n_j}{\triangle x}\right)\phi_j. \quad (6.44)$$

With this, the numerical flux (6.39) can be rewritten as

$$F(U; j+1/2) = a\,U^n_{j_1} + \frac{1}{2}|a|\sigma_{j_1}\triangle x - \frac{a}{2}\nu\sigma_{j_1}\triangle x \quad (6.45)$$

with

$$j_1 = \begin{cases} j, & \text{if } a > 0, \\ j+1, & \text{if } a < 0. \end{cases} \quad (6.46)$$

It means that the flux at $x_{j+1/2}$ is approximated for $a > 0$ by U_j together with σ_j and for $a < 0$ by U_{j+1} together with σ_{j+1}. Therefore, with the definition of the slope limiter (6.44), it can be seen that a piecewise linear reconstruction (6.43) over the cell $x \in [x_{j-1/2},\ x_{j+1/2}]$ is defined by the slope limiter. Also note that (6.45) reduces to the LAX-WNEDROFF flux if we use (6.44) to replace σ_{j1}, whereas with $\sigma_{j1} \equiv 0$ (6.45) recovers the upwind method. This justifies the choice of the definition (6.44) as a slope-limiter. The *slope-limiter* will play a *vital-role* in the remaining numerical methods that we are going to present. This is responsible for the order of the resolution and the entire results of the methods.

Thus, any of the flux-limiters presented above can be converted into the corresponding slope-limiter via (6.44) and vice versa. Also note that *slope-limiters* are *geometric features* whereas *flux-limiters* are their *algebraic* counterparts. Finally, the slope limiters can be viewed as an effective tool to make an appropriate piecewise linear cell reconstruction to let the numerical scheme hold the TVD property.

6.4.4 Nonlinear Conservation Law and TVD Methods

Next we will develop a second order accurate TVD method for non-linear hyperbolic conservation laws. Consider a homogeneous non-linear scalar hyperbolic conservation law

$$\frac{\partial w}{\partial t} + \frac{\partial f(w)}{\partial x} = 0 \quad \text{or} \quad \frac{\partial w}{\partial t} + a(w)\frac{\partial w}{\partial x} = 0, \quad (6.47)$$

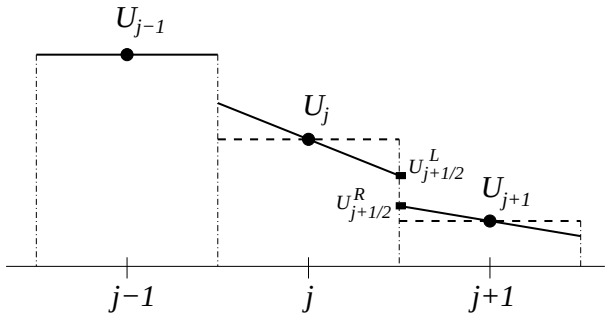

Figure 6.2: Schematic diagram for the cell average physical values U_j (dashed lines) and their linear piecewise cell reconstructions (solid lines). For each interface (e.g. between U_j and U_{j+1}) there are two values: $U^L_{j+1/2} = U_j + U'_j/2$ from the left-side of the cell and $U^R_{j+1/2} = U_{j+1} - U'_{j+1}/2$ from the right-side of the cell with the corresponding approximate derivatives U'_j and U'_{j+1}, respectively

where $a(w) = \partial f(w)/\partial w$ is the characteristic wave speed that depends on the conservative variable w. Because of the generality of a the problem turns out to be more complicated now than for the linear case.

In the upwind method the physical value at the cell boundary $U_{j+1/2}$ is assumed to be one of the adjacent cell averages, either U_j or U_{j+1}. This is equivalent to using a piecewise constant reconstruction, i.e., $\sigma_j = 0$, in the flux function over the cell in the scheme. It therefore only gives first order accuracy. Spatially high-order Monotonic Upstream Schemes for Conservation Laws (MUSCL) are introduced by applying the first-order numerical flux and replacing the arguments U_j and U_{j+1} by $U^L_{j+1/2}$ and $U^R_{j+1/2}$, respectively as

$$U^L_{j+1/2} = U^n_j + \tfrac{1}{2}U'_j, \qquad U^R_{j+1/2} = U^n_{j+1} - \tfrac{1}{2}U'_{j+1}, \tag{6.48}$$

where U'_j denotes the slope-limiter-determined derivative $U'_j = \triangle x\, \sigma_j$, see Fig. 6.2. Since the linear piecewise reconstruction is second order accurate, MUSCL is a spatially second-order scheme. This scheme is convenient for the scalar equation. Since we are interested in solving a system of equations the conservative variables must be transferred into characteristic variables. Detailed knowledge of the characteristics is therefore necessary which makes it difficult for the implementation of the scheme for a non-linear hyperbolic system of shallow avalanche equations. For obvious reasons we will not investigate this scheme any further.

6.4.5 TVD Lax-Friedrichs Method

In the sequel we will develop some schemes that do not require explicit knowledge of characteristics and the model equations can be solved directly in their conservative form. To obtain a spatially high-order differencing a better cell reconstruction is necessary. One possibility is to apply the "TVD limiters" to obtain the linear piecewise reconstruction. The application of the slope limiters can eliminate unwanted oscillations and gives second order accurate reconstruction for smooth solutions (except near the critical points) over the cell. One can therefore develop high-order resolution schemes without spurious oscillation, but with the ability to capture a possible discontinuity.

The Lax-Friedrichs method is a prototype of a central difference approximation. The

main advantage of this method is simplicity. No RIEMANN problems need to be solved. The LAX-FRIEDRICHS method is defined by

$$U_j^{n+1} = \frac{1}{2}\left(U_{j+1}^n + U_{j-1}^n\right) - \frac{\triangle t}{2\triangle x}\left\{f_{j+1}^n - f_{j-1}^n\right\}, \tag{6.49}$$

where $f_j^n = f(U_j^n)$. This scheme can alternatively be written as

$$U_j^{n+1} = U_j^n - \frac{\triangle t}{2\triangle x}\left\{f_{j+1}^n - f_{j-1}^n - \frac{\triangle x}{\triangle t}\left(U_{j+1}^n - 2U_j^n + U_{j-1}^n\right)\right\}. \tag{6.50}$$

This can be realised as a scheme with the numerical fluxes of the kind

$$\begin{aligned} \mathcal{F}_{j+1/2}^{LF} &= \tfrac{1}{2}\left\{f_{j+1} + f_j - \tfrac{\triangle x}{\triangle t}\left(U_{j+1}^n - U_j^n\right)\right\}, \\ \mathcal{F}_{j-1/2}^{LF} &= \tfrac{1}{2}\left\{f_j + f_{j-1} - \tfrac{\triangle x}{\triangle t}\left(U_j^n - U_{j-1}^n\right)\right\}. \end{aligned} \tag{6.51}$$

This method has a *dissipation* term of the form

$$\phi_{j+1/2}^{LF} = \frac{\triangle x}{\triangle t}\left(U_{j+1}^n - U_j^n\right) = \frac{\triangle x}{\triangle t}\triangle U_{j+1/2}^n. \tag{6.52}$$

The LAX-FRIEDRICHS (LF) scheme shows that it requires no information about the characteristic speed which makes it easier to handle in real applications.

Replacing U_{j+1} and U_j by the second order accurate $U_{j+1/2}^R$ and $U_{j+1/2}^L$ from (6.48) (which inherits the slope-limiter determined derivatives) changes the first-order LAX-FRIEDRICHS scheme into a second-order TVD LAX-FRIEDRICHS (TVDLF) scheme,

$$U_j^{n+1} = U_j^n - \frac{\triangle t}{\triangle x}\left(\mathcal{F}_{j+1/2} - \mathcal{F}_{j-1/2}\right), \tag{6.53}$$

with the flux

$$\mathcal{F}_{j+1/2} = \frac{1}{2}\left\{f\left(U_{j+1/2}^R\right) + f\left(U_{j+1/2}^L\right) - \frac{\triangle x}{\triangle t}\triangle U_{j+1/2}^{RL}\right\}, \tag{6.54}$$

where the *dissipative limiter* of the TVDLF scheme is given by

$$\phi_{j+1/2}^{TVDLF} = \frac{\triangle x}{\triangle t}\left(U_{j+1/2}^R - U_{j+1/2}^L\right) = \frac{\triangle x}{\triangle t}\triangle U_{j+1/2}^{RL}. \tag{6.55}$$

6.4.6 Modified TVDLF Scheme

Although the TVDLF scheme can be applied to any system of conservation laws without knowledge of the characteristic variables in contrast to the MUSCL scheme, the dissipative limiter (6.55) in the TVDLF scheme results in large diffusion. TÓTH and ODSTRČIL [126] suggested that the dissipative limiter should be multiplied by the maximum COURANT number $C_{j+1/2}^{max}$ to obtain a *modified dissipative limiter*, i.e.,

$$\phi_{j+1/2}^{MLF} = C_{j+1/2}^{max}\phi_{j+1/2}^{LF} = \left(C_{j+1/2}^{max}\frac{\triangle x}{\triangle t}\right)\triangle U_{j+1/2}^{RL} = a_{j+1/2}^{max}\triangle U_{j+1/2}^{RL}, \tag{6.56}$$

with

$$a^{max}_{j+1/2} = \max\left\{a^{max}(U^R_{j+1/2}),\, a^{max}(U^L_{j+1/2})\right\}, \tag{6.57}$$

where $a^{max}_{j+1/2}$ is the associated maximum wave speed of the hyperbolic equation. Therefore, the modified TVDLF (MTVDLF) flux is expressed by

$$\mathcal{F}^{MLF}_{j+1/2} = \tfrac{1}{2}\left\{f(U^R_{j+1/2}) + f(U^L_{j+1/2}) - a^{max}_{j+1/2}\triangle U^{RL}_{j+1/2}\right\}, \tag{6.58}$$

where the superscript "MLF" stands for the *dissipative limiter* of the modified TVD Lax-Friedrichs scheme.

Upto now we have discussed the methods that are second-order only in space. Furthermore, we can improve the numerical model by using the Hancock *predictor step* (see e.g., [126]) which can be used to introduce an *intermediate state* "$U^{n+1/2}_j$" in order to obtain a method that is second order accurate in space as well as time; explicitly,

$$U^{n+1/2}_j = U^n_j - \frac{\triangle t}{2\triangle x}\left\{f(U^n_{j+1/2}) - f(U^n_{j-1/2})\right\}, \tag{6.59}$$

in which the flux arguments are taken to be $U^n_{j\pm1/2} = U^n_j \pm \frac{\triangle x}{2}\sigma_j$. The full scheme (*corrector-step*) then takes the form

$$U^{n+1}_j = U^n_j - \tfrac{\triangle t}{\triangle x}\left\{\mathcal{F}^{MLF}(U^{n+1/2}_{j+1/2}) - \mathcal{F}^{MLF}(U^{n+1/2}_{j-1/2})\right\}, \tag{6.60}$$

where $\mathcal{F}$ is defined in (6.58). Note that no dissipative limiter appears in the predictor step (6.59). The left and right values, ${U^{n+1/2}_{j+1/2}}^L$ and ${U^{n+1/2}_{j+1/2}}^R$ arising in equation (6.60) can be computed by first-order Taylor series expansion at the gridpoint $(x_j,\, t^n)$ and approximated, respectively as,

$${U^{n+1/2}_{j+1/2}}^L = U^n_j \quad + \tfrac{\triangle t}{2}\left(\partial U/\partial t\right)^n_j \quad + \tfrac{\triangle x}{2}\sigma^n_j \quad = U^{n+1/2}_j + \tfrac{\triangle x}{2}\sigma^n_j \quad , \tag{6.61}$$

$${U^{n+1/2}_{j+1/2}}^R = U^n_{j+1} + \tfrac{\triangle t}{2}\left(\partial U/\partial t\right)^n_{j+1} - \tfrac{\triangle x}{2}\sigma^n_{j+1} = U^{n+1/2}_{j+1} - \tfrac{\triangle x}{2}\sigma^n_{j+1}. \tag{6.62}$$

Thus, we have seen that the main idea of the MTVDLF method is to avoid the dissipative limiter but still maintain the second-order accuracy.

6.5 NOC Schemes

Nessyahu & Tadmor [85], developed the one-dimensional Non-Oscillatory Central Differencing (NOC) scheme which is a *second-order accurate* extension of the classical Lax-Friedrichs scheme [73], but with high-resolution (higher-order) obeying the TVD requirement. In this scheme the TVD limiter is used for the cell reconstructions. If the cell reconstruction is computed, numerical integrations with the NOC schemes can be realized. A main concept of the NOC schemes is the use of a *staggered grid*, which is a *predictor-corrector method* and consists of two steps. At time $t^{n+1} = t^n + \Delta t$, the cell averages $U^{n+1}_{j+1/2}$ are evaluated over the bounded region $[x_j, x_{j+1}]$ (see Fig. 6.3). As a consequence, the *boundaries* of the cells at the new time level are the *centers* of the cells at the old time level. At these boundary points, the piecewise polynomial reconstruction of

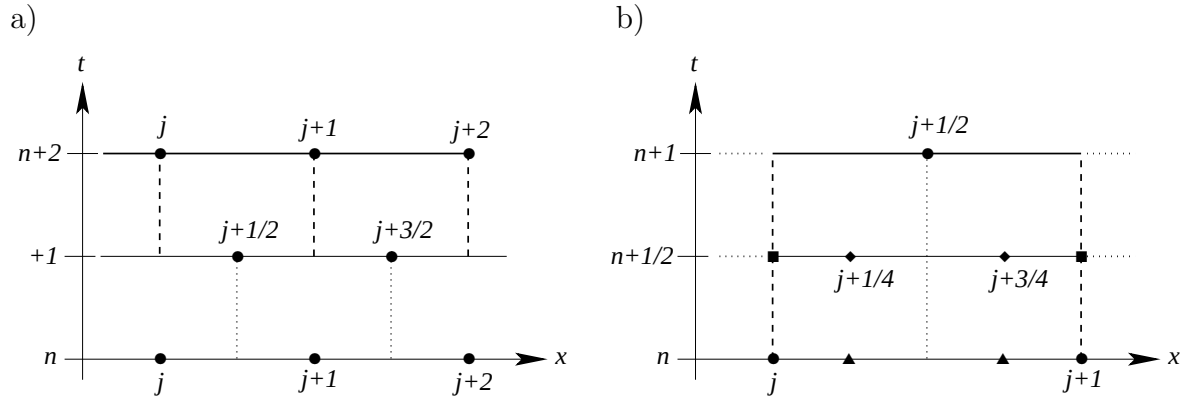

Figure 6.3: Diagram of the NOC scheme. a) Grid points computed in the NOC method. b) NOC computational diagram, where • indicate the grid points at time level n, $n+1$ and $n+2$, ■ represent the positions where the fluxes $\mathcal{F}$ at time level $n+1/2$ are approximated, ♦ are for the source terms s and ▲ denote the quarter and three-quarter points e.g., $U^n_{j+1/4}$, $U^n_{j+3/4}$

the cell averages at the old time level t^n is smooth, and it remains so for $t < t^{n+1}$ under an appropriate restriction of the time step. Therefore, the flux across the boundaries of the cells at the new time level may be evaluated by Taylor extrapolations using the differential equation and standard quadrature rules. Here we use the *midpoint rule* in time to achieve temporally second-order accuracy.

Let us consider a general one-dimensional hyperbolic differential equation

$$\frac{\partial w}{\partial t} + \frac{\partial f(w)}{\partial x} = s(w), \tag{6.63}$$

where $s(w)$ is the source term. Integrating (6.63) over the rectangle $[x_j,\, x_{j+1}] \times [t^n,\, t^{n+1}]$ gives

$$\begin{aligned}\int_{x_j}^{x_{j+1}} w(x,\, t^{n+1})\,\mathrm{d}x = \int_{x_j}^{x_{j+1}} w(x,\, t^n)\,\mathrm{d}x - \int_{t^n}^{t^{n+1}} \{f(x_{j+1},\, t) - f(x_j,\, t)\}\,\mathrm{d}t \\ + \int_{x_j}^{x_{j+1}} \int_{t^n}^{t^{n+1}} s(x,\, t)\,\mathrm{d}t\,\mathrm{d}x.\end{aligned} \tag{6.64}$$

This is discretised by

$$\triangle x\, U^{n+1}_{j+1/2} = \tfrac{\triangle x}{2}\left(U^n_{j+1/4} + U^n_{j+3/4}\right) - \triangle t\left(f^{n+1/2}_{j+1} - f^{n+1/2}_{j}\right) + \tfrac{\triangle t\,\triangle x}{2}\left(s^{n+1/2}_{j+1/4} + s^{n+1/2}_{j+3/4}\right), \tag{6.65}$$

where $U_{j+1/2}$ is interpreted as the cell average over $[x_j,\, x_{j+1}]$. Dividing through by Δx this reduces to a scheme of the type

$$U^{n+1}_{j+1/2} = \tfrac{1}{2}\left(U^n_{j+1/4} + U^n_{j+3/4}\right) - \tfrac{\triangle t}{\triangle x}\left(f^{n+1/2}_{j+1} - f^{n+1/2}_{j}\right) + \tfrac{\triangle t}{2}\left(s^{n+1/2}_{j+1/4} + s^{n+1/2}_{j+3/4}\right), \tag{6.66}$$

as illustrated in Fig. 6.3b. Using the TVD slope limiter σ^n_j for the j^{th} cell at time t^n, the values of $U^n_{j+1/4}$ and $U^n_{j+3/4}$ are determined by the *reconstruction* over the j^{th} and $(j+1)^{th}$ cell, i.e.,

$$U^n_{j+1/4} = U^n_j + \tfrac{\triangle x}{4}\sigma^n_j, \quad U^n_{j+3/4} = U^n_{j+1} - \tfrac{\triangle x}{4}\sigma^n_{j+1}. \tag{6.67}$$

The integral of the transport flux f is approximated by the physical values at $(x_j,\, t^{n+1/2})$ and $(x_{j+1},\, t^{n+1/2})$, i.e.,

$$f_j^{n+1/2} = f\left(U_j^{n+1/2}\right), \qquad f_{j+1}^{n+1/2} = f\left(U_{j+1}^{n+1/2}\right), \tag{6.68}$$

together with the following approximations for the arguments

$$U_j^{n+1/2} = U_j^n + \frac{\triangle t}{2}\left(\partial U/\partial t\right)_j^n, \qquad U_{j+1}^{n+1/2} = U_{j+1}^n + \frac{\triangle t}{2}\left(\partial U/\partial t\right)_{j+1}^n. \tag{6.69}$$

Similarly, the integral of the source s is approximated at $(x_{j+1/4}, t^{n+1/2})$ and $(x_{j+3/4}, t^{n+1/2})$, respectively, by

$$s_{j+1/4}^{n+1/2} = s\left(U_{j+1/4}^{n+1/2}\right), \quad s_{j+3/4}^{n+1/2} = s\left(U_{j+3/4}^{n+1/2}\right), \tag{6.70}$$

in which the grid values are approximated by the cell reconstructions

$$U_{j+1/4}^{n+1/2} = U_j^n + \frac{\triangle t}{2}\left(\partial U/\partial t\right)_j^n + \frac{\triangle x}{4}\sigma_j^n, \quad U_{j+3/4}^{n+1/2} = U_{j+1}^n + \frac{\triangle t}{2}\left(\partial U/\partial t\right)_{j+1}^n - \frac{\triangle x}{4}\sigma_{j+1}^n. \tag{6.71}$$

Finally, the temporal derivative $(\partial U/\partial t)_j^n$ in (6.69) and (6.71) is determined by using the conservation law (6.63) as follows

$$\left(\partial w/\partial t\right)_j^n = -\left(\partial f/\partial x\right)_j^n + s_j^n = -a_j^n\,\sigma_j^n + s_j^n, \tag{6.72}$$

where

$$\left(\partial f/\partial x\right) = \left(\partial f/\partial w\right)\left(\partial w/\partial x\right), \quad a = \partial f/\partial w, \quad \sigma = \partial w/\partial x. \tag{6.73}$$

The CFL Condition

Substituting the TVD *cell reconstruction* by the *midpoint rule* and using the one-step scheme, the scheme (6.66) reduces to

$$U_{j+1/2}^{n+1} = \frac{1}{2}\left(U_j^n + U_{j+1}^n\right) - \frac{\triangle t}{\triangle x}\left(f_{j+1}^n - f_j^n\right), \tag{6.74}$$

which satisfies the TVD requirement (6.17) under the CFL condition:

$$\frac{\triangle t}{\triangle x}\left|\frac{f_{j+1} - f_j}{U_{j+1} - U_j}\right| \le \frac{1}{2}, \quad \Rightarrow \quad \frac{\triangle t}{\triangle x}\left|a^{max}\right| < \frac{1}{2}, \quad \text{for all} \quad j, \tag{6.75}$$

where a^{max} is the maximum wave speed. Nessyahu & Tadmor [85] showed by some numerical examples that with the CFL condition (6.75) the NOC scheme (6.66) possesses the TVD property for a homogeneous scalar conservative law $\partial w/\partial t + \partial f(w)/\partial x = 0$.

6.6 Essentially Non-Oscillatory Scheme

As a generalisation of the TVD method Harten et al. [39] introduced the Essentially Non-Oscillatory (ENO) scheme, in which the cell reconstructions are approximated by an essentially non-oscillatory high-order accurate interpolation of a piecewise smooth function from its cell averages. *The fundamental base of the* ENO *schemes is (i) the use*

of the smoothest polynomial (stencil) among the feasible candidates to approximate the fluxes at the cell boundaries to high order, and, (ii) at the same time to avoid spurious oscillations near shocks and discontinuities of the physical variables. For our purpose of solving avalanche equations this scheme serves quite well, as we will see later. Although there are more higher order schemes, we will not go any further.

Recall that U_j^n is the exact cell average at $t = t^n$. In the last sections the piecewise linear *cell reconstruction* is defined by the TVD limiters. These piecewise linear cell reconstructions are at most of second order accuracy. By using a *primitive function* $p(x,\, t)$ it is possible to construct a polynomial approximation over the cell that is accurate pointwise to higher order. At fixed time t^n, the primitive function is defined by

$$p(x) = \int_{x_{low}}^{x} w(\xi,\, t^n)\mathrm{d}\xi, \tag{6.76}$$

where $w(x,\, t^n)$ is the exact solution at t^n and the variable t^n in $p(x,\, t^n)$ is dropped here for ease. Since the ultimate purpose is to determine the cell reconstruction

$$\widetilde{w}(x,\, t^n) = \partial p(x)/\partial x, \tag{6.77}$$

the lower limit x_{low} in (6.76) is arbitrary. Changing the lower limit only shifts $p(x)$ by a constant and does not influence the reconstruction $\widetilde{w}(x,\, t^n)$. By inspection of (6.77) it implies that one can obtain an r^{th} order accurate cell reconstruction by an appropriate interpolation polynomial of degree r. Integrating over the domain $[x_{low},\, x_{j+1/2}]$ yields

$$P_j = p(x_{j+1/2}) = \int_{x_{low}}^{x_{j+1/2}} w(\xi,\, t^n)\mathrm{d}\xi. \tag{6.78}$$

Note that the value of P_j lies at $x_{j+1/2}$. The choice $x_{low} = x_{1/2}$, with the *cell averages* U_j^n, reduces (6.78) to

$$P_j = \triangle x \sum_{i=1}^{j} U_i^n. \tag{6.79}$$

There are r different r^{th}-order polynomials determined by different data sets

$$\left\{x_{j-r+k+1/2},\, x_{j-r+k+3/2}, \cdots, x_{j+k+1/2}\right\}, \qquad k = 0,\, 1,\, \cdots,\, r-1, \tag{6.80}$$

for interpolating the primitive function $p(x)$ for the j^{th} cell over $[x_{j-1/2},\, x_{j+1/2}]$, where $r \geq 1$ is a positive integer, see Fig. 6.4. These different data sets are called the *stencil candidates*, which determine the corresponding *polynomial candidate* $q_k^r(x)$ by

$$\begin{aligned} q_k^r(x) &= P[x_{j-r+k+1/2}] + P[x_{j-r+k+1/2},\, x_{j-r+k+3/2}](x - x_{j-r+k+1/2}) \\ &+ \cdots + P[x_{j-r+k+1/2}, x_{j-r+k+3/2},\, \ldots,\, x_{j+k+1/2}] \prod_{m=j-r+k+1/2}^{j+k-1/2} (x - x_m). \end{aligned} \tag{6.81}$$

Let us define the divided differences in (6.81) as follows

$$P[x_{i+1/2}] = P_i \tag{6.82}$$

$$P[x_{i+1/2}, \cdots,\, x_{i+n+1/2}] = \frac{P[x_{i+3/2}, \cdots,\, x_{i+n+1/2}] - P[x_{i+1/2}, \cdots,\, x_{i+n-1/2}]}{x_{i+n+1/2} - x_{i+1/2}}, \tag{6.83}$$

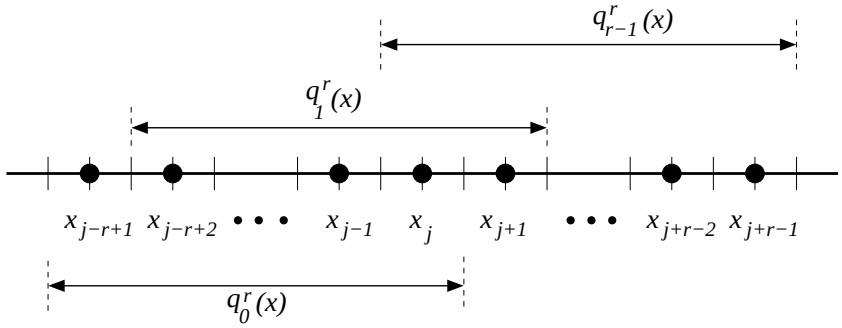

Figure 6.4: Sketch of the r interpolation polynomials, $q^r_k(x)$, by different stencil candidates for the j^{th} cell reconstruction

where $i = j - r + k$ for ease. Let $Q^r_j(x)$ denote the appropriate interpolation polynomial for the j^{th} cell among the r polynomial candidates $q^r_k(x)$ with some k. Applying (6.81) on (6.77), the j^{th} cell reconstruction of r^{th} order can be obtained by

$$\widetilde{w}^r_j(x) = \frac{\partial Q^r_j(x)}{\partial x}, \quad x \in [x_{j-1/2},\, x_{j+1/2}]. \tag{6.84}$$

Therefore, from (6.83), it can be seen that $\widetilde{w}^r_j(x)$ depends upon the cell averages, $\{U^n_{i+1},\, U^n_{i+2},\, \cdots,\, U^n_{i+r+1}\}$, while, e.g.

$$U^n_{i+1} = \frac{P[x_{i+3/2}] - P[x_{i+1/2}]}{x_{i+3/2} - x_{i+1/2}} = P[x_{i+1/2},\, x_{i+3/2}].$$

However, the exact values of P in (6.83) are not necessary because of the presence of the differential operator $\partial(\bullet)/\partial x$.

There are r different stencil candidates $q^r_k(x)$, for the j^{th} cell, see Fig. 6.4. If $p(x) \in C^k$ in $[x_{i+1/2},\, x_{i+k+1/2}]$, by numerical analysis (6.83) it can be put in the form

$$P[x_{i+1/2}, \cdots x_{i+k+1/2}] = \frac{1}{k!}\frac{\mathrm{d}^k}{\mathrm{d}x^k}p(\xi), \quad \xi \in [x_{i+1/2},\, x_{i+k+1/2}]. \tag{6.85}$$

Any large fluctuation among the data within the interval $[x_{i+1/2},\, x_{i+k+1/2}]$ will result in large $P[x_{i+1/2}, \cdots x_{i+k+1/2}]$ (see Sonar, [119]). This helps in avoiding wrong stencil candidates from consideration.

Obviously, the first order interpolation polynomial of the primitive function for the j^{th} cell takes the form

$$Q^1_j(x) := P[x_{j-1/2}] + P[x_{j-1/2},\, x_{j+1/2}](x - x_{j-1/2}). \tag{6.86}$$

Nevertheless, there are two possibilities for the second order polynomial interpolation over the data sets, $\{P_{j-2},\, P_{j-1},\, P_j\}$ or $\{P_{j-1},\, P_j,\, P_{j+1}\}$. *To avoid* the stencil candidate in which *jumps* exist, *the flatter data set is the choice.* This means, if $\big|P[x_{j-3/2},\, x_{j-1/2},\, x_{j+1/2}]\big| < \big|P[x_{j-1/2},\, x_{j+1/2},\, x_{j+3/2}]\big|$, the interpolation $Q^2_j(x)$ is described by

$$\begin{aligned} Q^2_j(x) := {} & P[x_{j-3/2}] + P[x_{j-3/2},\, x_{j-1/2}](x - x_{j-3/2}) \\ & + P[x_{j-3/2},\, x_{j-1/2},\, x_{j+1/2}](x - x_{j-3/2})(x - x_{j-1/2}). \end{aligned} \tag{6.87}$$

Alternatively, for $\big|P[x_{j-3/2},\, x_{j-1/2},\, x_{j+1/2}]\big| > \big|P[x_{j-1/2},\, x_{j+1/2},\, x_{j+3/2}]\big|$ it is defined as

$$\begin{aligned} Q_j^2(x) := {} & P[x_{j-1/2}] + P[x_{j-1/2},\, x_{j+1/2}](x - x_{j-1/2}) \\ & + P[x_{j-1/2},\, x_{j+1/2},\, x_{j+3/2}](x - x_{j-1/2})(x - x_{j+1/2}). \end{aligned} \tag{6.88}$$

At this point we can make a connection between the Minmod limiter and the ENO-cell reconstruction. The criteria (6.87)–(6.88) result in a cell reconstruction *equivalent* to a *Minmod-limiter*-determined cell reconstruction (see LeVeque [74]). Therefore, the ENO-interpolation polynomial of N^{th} order ($N \geq 2$) for the j^{th} cell can be defined as follows

$$Q_j^N(x,\, P) := Q_j^{N-1}(x,\, P) + \min(|a_N|,\, |b_N|) \prod_{m=m_m^{(N-1)}}^{m_M^{(N-1)}} (x - x_m), \tag{6.89}$$

where

$$a_N := P[x_{m_m^{(N-1)}},\, \cdots,\, x_{m_M^{(N-1)}+1}], \quad b_N := P[x_{m_m^{(N-1)}-1},\, \cdots,\, x_{m_M^{(N-1)}}] \tag{6.90}$$

and

$$\begin{aligned} |a_N| < |b_N| : \quad & \begin{cases} m_m^{(N-1)} = m_m^{(N-1)}, \\ m_M^{(N-1)} = m_M^{(N-1)} + 1, \end{cases} \\ |a_N| > |b_N| : \quad & \begin{cases} m_m^{(N-1)} = m_m^{(N-1)} - 1, \\ m_M^{(N-1)} = m_M^{(N-1)} \end{cases} \end{aligned} \tag{6.91}$$

with

$$m_m^{(1)} = j - 1/2, \quad m_M^{(1)} = j + 1/2\,. \tag{6.92}$$

In (6.84) the r^{th} order interpolation polynomial $Q_j^r(x)$ is used to obtain an r^{th} order accurate reconstruction over the j^{th} cell. These cell reconstructions are used to obtain the approximate values at the left and right cell interfaces, and when applied in the TVDLF (modified TVDLF) schemes, i.e., the left- and right-hand values at $x_{j+1/2}$ are, respectively,

$$U_{j+1/2}^L = \widetilde{w}_j(x_{j+1/2}), \qquad U_{j+1/2}^R = \widetilde{w}_{j+1}(x_{j+1/2}). \tag{6.93}$$

Analogously, these high-order cell reconstructions can also be employed in the NOC scheme, which was the main aim of this section.

The numerical methods presented in this chapter are somehow standard and can be found to a large extent in modern and advanced text books dealing with numerical methods for hyperbolic conservation equations, e.g., [69, 74, 124, 125]. Alternatively, essentially similar derivations are presented in [121].

Chapter 7

Two Dimensional Shock-Capturing Scheme for Avalanching Flow

7.1 Two-Dimensional NOC Schemes

The one-dimensional Non-Oscillatory Central Differencing (NOC) scheme of Nessyahu & Tadmor [85] (as discussed in the last Chapter) is a second-order accurate extension of the classical Lax-Friedrichs scheme [73]. Its two-dimensional scheme was first proposed by Jiang & Tadmor [62] and is also modified by Lie & Noelle [75]. This scheme was applied to numerical simulations of granular avalanche flows by Tai [121], Tai et al. [122], Wang et al. [130], Gray et al. [33] and Pudasaini and others [100, 102, 103, 104].

Since in numerical schemes only values of the cell averages are available, with the concept of high-resolution methods the distribution of the physical variables over the cell is reconstructed. As in the one-dimensional case, the two-dimensional NOC scheme is a *predictor-corrector* method which consists of two steps: (i) The grid values are predicted according to the non-oscillatory reconstructions from the given cell averages. (ii) At the second corrector step, a *staggered averaging* is introduced, together with the predicted mid-values, to determine the full evolution of these averages. This results in a high-oder, non-oscillatory central scheme. The key feature of this scheme is that the staggered averages at $(x_{p\pm1/2}, y_{q\pm1/2}, t^{n+1})$ are computed by the cell averages at (x_p, y_q, t^n), see Fig. 7.1a. One important property of this scheme is that it does not necessitate any dimensional splitting. Our main aim in this Chapter is to extend this scheme to a system of non-homogeneous two-dimensional shallow avalanche equations.

Let us start with a general two-dimensional conservation law

$$\frac{\partial w}{\partial t} + \frac{\partial f(w)}{\partial x} + \frac{\partial g(w)}{\partial y} = s(w), \tag{7.1}$$

subject to prescribed initial data, $w(x,\, y,\, t=0) = w_0\,(x,\, y)$. Let $C_{p,q}$ be the $(p,q)^{th}$ cell covered region,

$$C_{p,q} = \left\{ (x,\, y) \,\middle|\, |x - x_p| \le \tfrac{\triangle x}{2},\ |y - y_q| \le \tfrac{\triangle y}{2} \right\}. \tag{7.2}$$

Let, moreover, $U^n_{p,q}$ denote the cell average over this region at time t^n, and let

$$\widetilde{w}_{p,q}(x,\, y,\, t^n) = U^n_{p,q} + \sigma^x_{p,q}(x - x_p) + \sigma^y_{p,q}(y - y_q), \quad \text{for} \quad (x,y) \in C_{p,q}, \tag{7.3}$$

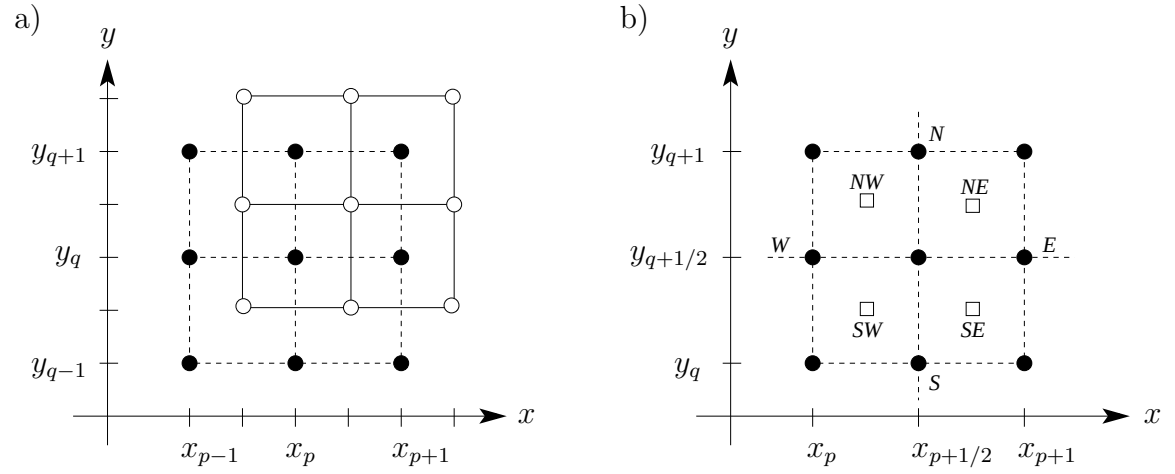

Figure 7.1: a) The two dimensional NOC scheme and the staggered grid: The staggered averages at $(x_{p\pm1/2}, y_{q\pm1/2}, t^{n+1})$, denoted by "$\circ$", are computed by the averages at (x_p, y_q, t^n), represented by "$\bullet$". b) The two dimensional NOC scheme and a floor plan of the staggered grid: The cell $C_{p+1/2,\,q+1/2}$ consists of four intersecting cells with $C_{p,q}$, $C_{p+1,q}$, $C_{p+1,q+1}$ and $C_{p,q+1}$, denoted by $C^{SW}_{p,q}$, $C^{SE}_{p+1,q}$, $C^{NE}_{p+1,q+1}$ and $C^{NW}_{p,q+1}$, respectively. "$\bullet$" indicates the computed cell centre and "$\square$" denotes the centre of the intersecting cell. The numerical fluxes are considered on the values across the corresponding faces, east(E), north(N), west(W) and south(S), respectively

be a piecewise linear reconstruction over the cell, where $\sigma^x_{p,q}$ and $\sigma^y_{p,q}$ denote the discrete slopes of U in the x- and y-directions, respectively, which are determined by a TVD-limiter [74], or a central ENO cell reconstruction [38]. In the TVD schemes they are the TVD slope limiters and in the ENO schemes they are the mean slopes of the high-order interpolations over the cells.

The piecewise linear cell reconstructions are at most of second-order accuracy. With the help of the Essentially Non-Oscillatory (ENO) schemes it is possible to construct a polynomial approximation over the cell that is accurate pointwise to higher order. The ENO schemes were first developed by Harten [38], in which the cell reconstructions are approximated by an essentially non-oscillatory high-order accurate polynomial interpolation of a piecewise smooth function from its cell averages. So, it is a generalisation of the TVD method of piecewise linear cell reconstructions. The second-order ENO scheme results in a piecewise linear cell reconstruction, equivalent to a TVD method with a cell reconstruction determined by the Minmod limiter. In this thesis, the third-order quadratic ENO cell reconstruction is employed and compared with other schemes, for details see [38, 121, 130]. Let $U_{p+1/2,\,q+1/2}$ denote the *staggered average* over $C_{p+1/2,\,q+1/2}$. Integration of (7.1) over $C_{p+1/2,\,q+1/2} \times [t^n,\, t^{n+1}]$ yields

$$\begin{aligned} U^{n+1}_{p+1/2,\,q+1/2} &= \frac{1}{\triangle x\,\triangle y}\int_{x_p}^{x_{p+1}}\int_{y_q}^{y_{q+1}} w(x,\,y,\,t^n)\mathrm{d}x\,\mathrm{d}y \\ &- \frac{1}{\triangle x\triangle y}\int_{t^n}^{t^{n+1}}\int_{y_q}^{y_{q+1}} \{f(x_{p+1},\,y,\,t) - f(x_p,\,y,\,t)\}\,\mathrm{d}y\,\mathrm{d}t \\ &- \frac{1}{\triangle x\triangle y}\int_{t^n}^{t^{n+1}}\int_{x_p}^{x_{p+1}} \{g(x,\,y_{q+1},\,t) - g(x,\,y_q,\,t)\}\,\mathrm{d}x\,\mathrm{d}t \\ &+ \frac{1}{\triangle x\triangle y}\int_{t^n}^{t^{n+1}}\int_{x_p}^{x_{p+1}}\int_{y_q}^{y_{q+1}} s(x,\,y,\,t)\mathrm{d}x\,\mathrm{d}y\,\mathrm{d}t. \end{aligned} \tag{7.4}$$

The first integration on the right-hand side of this equation can be split into four parts as follows:

$$\int_{x_p}^{x_{p+1}}\int_{y_q}^{y_{q+1}} w(x,\, y,\, t^n)\,\mathrm{d}x\,\mathrm{d}y = \iint\limits_{C_{p,q}^{SW}} w(x,\, y,\, t^n)\,\mathrm{d}x\,\mathrm{d}y + \iint\limits_{C_{p+1,q}^{SE}} w(x,\, y,\, t^n)\,\mathrm{d}x\,\mathrm{d}y + \iint\limits_{C_{p+1,q+1}^{NE}} w(x,\, y,\, t^n)\,\mathrm{d}x\,\mathrm{d}y + \iint\limits_{C_{p,q+1}^{NW}} w(x,\, y,\, t^n)\,\mathrm{d}x\,\mathrm{d}y. \tag{7.5}$$

These contributions come from the four intersecting cells, namely, $C_{p,q}^{SW}$, $C_{p+1,q}^{SE}$, $C_{p+1,q+1}^{NE}$ and $C_{p,q+1}^{NW}$. These cells are defined as $C_{p,q}^{SW} := C_{p+1/2,q+1/2} \cap C_{p,q}$, $C_{p+1,q}^{SE} := C_{p+1/2,q+1/2} \cap C_{p+1,q}$, $C_{p+1,q+1}^{NE} := C_{p+1/2,q+1/2} \cap C_{p+1,q+1}$ and $C_{p,q+1}^{NW} := C_{p+1/2,q+1/2} \cap C_{p,q+1}$, respectively, see Fig. 7.1b.

Starting with the intersection cell $C_{p,q}^{SW}$ at the south west corner, using the reconstructed polynomial in (7.3) together with the discrete slopes $\sigma_{j,k}^x$ and $\sigma_{j,k}^y$ of U in the x- and y-directions, respectively, results in

$$\begin{aligned}
&\frac{1}{\triangle x\,\triangle y}\int_{x_p}^{x_{p+1/2}}\int_{y_q}^{y_{q+1/2}} w(x,\, y,\, t^n)\mathrm{d}x\,\mathrm{d}y \\
&= \frac{1}{\triangle x\,\triangle y}\int_{x_p}^{x_{p+1/2}}\int_{y_q}^{y_{q+1/2}} \left[U_{p,q}^n + \sigma_{p,q}^x(x-x_p) + \sigma_{p,q}^y(y-y_q)\right]\mathrm{d}x\,\mathrm{d}y \\
&= \frac{1}{4}U_{p,q}^n + \frac{\triangle x}{16}\sigma_{p,q}^x + \frac{\triangle y}{16}\sigma_{p,q}^y.
\end{aligned} \tag{7.6}$$

Following this procedure and continuing in counterclockwise direction, it follows that

$$\frac{1}{\triangle x\,\triangle y}\int_{x_{p+1/2}}^{x_{p+1}}\int_{y_q}^{y_{q+1/2}} w(x,\, y,\, t^n)\mathrm{d}x\,\mathrm{d}y = \frac{1}{4}U_{p+1,q}^n - \frac{\triangle x}{16}\sigma_{p+1,q}^x + \frac{\triangle y}{16}\sigma_{p+1,q}^y, \tag{7.7}$$

$$\frac{1}{\triangle x\,\triangle y}\int_{x_{p+1/2}}^{x_{p+1}}\int_{y_{q+1/2}}^{y_{q+1}} w(x,\, y,\, t^n)\mathrm{d}x\,\mathrm{d}y = \frac{1}{4}U_{p+1,q+1}^n - \frac{\triangle x}{16}\sigma_{p+1,q+1}^x - \frac{\triangle y}{16}\sigma_{p+1,q+1}^y, \tag{7.8}$$

$$\frac{1}{\triangle x\,\triangle y}\int_{x_p}^{x_{p+1/2}}\int_{y_{q+1/2}}^{y_{q+1}} w(x,\, y,\, t^n)\mathrm{d}x\,\mathrm{d}y = \frac{1}{4}U_{p,q+1}^n + \frac{\triangle x}{16}\sigma_{p,q+1}^x - \frac{\triangle y}{16}\sigma_{p,q+1}^y. \tag{7.9}$$

Next, we compute the four numerical fluxes corresponding to the points $x_{p+1}, x_p, y_{q+1}, y_q$ in (7.4) on the east and west (associated with the flux function f), and north and south (associated with the flux function g) surfaces, respectively, see Fig. 7.1b. They are approximated by the *midpoint quadrature rule* for second-order accuracy of the temporal integral and *second-order rectangular rule* for the spatial integration across the corresponding face. The flux along the east face is then given by

$$\begin{aligned}
&\frac{1}{\triangle x\triangle y}\int_{t^n}^{t^{n+1}}\int_{y_q}^{y_{q+1}} f(x_{p+1},\, y,\, t)\mathrm{d}y\,\mathrm{d}t \\
&= \frac{1}{2}\frac{\triangle t}{\triangle x}\left\{f(x_{p+1},\, y_q,\, t^{n+1/2}) + f(x_{p+1},\, y_{q+1},\, t^{n+1/2})\right\} \\
&= \frac{1}{2}\frac{\triangle t}{\triangle x}\left\{f\left(U_{p+1,q}^{n+1/2}\right) + f\left(U_{p+1,q+1}^{n+1/2}\right)\right\}.
\end{aligned} \tag{7.10}$$

Analogously, the other three fluxes in counterclockwise direction are, respectively, given by

$$\frac{1}{\triangle x \triangle y}\int_{t^n}^{t^{n+1}}\int_{x_p}^{x_{p+1}} g(x,\, y_{q+1},\, t)\mathrm{d}x\,\mathrm{d}t = \frac{1}{2}\frac{\triangle t}{\triangle y}\left\{g\left(U_{p,q+1}^{n+1/2}\right) + g\left(U_{p+1,q+1}^{n+1/2}\right)\right\}, \tag{7.11}$$

$$\frac{1}{\triangle x \triangle y}\int_{t^n}^{t^{n+1}}\int_{y_q}^{y_{q+1}} f(x_p,\, y,\, t)\mathrm{d}y\,\mathrm{d}t = \frac{1}{2}\frac{\triangle t}{\triangle x}\left\{f\left(U_{p,q}^{n+1/2}\right) + f\left(U_{p,q+1}^{n+1/2}\right)\right\}, \tag{7.12}$$

$$\frac{1}{\triangle x \triangle y}\int_{t^n}^{t^{n+1}}\int_{x_p}^{x_{p+1}} g(x,\, y_q,\, t)\mathrm{d}x\,\mathrm{d}t = \frac{1}{2}\frac{\triangle t}{\triangle y}\left\{g\left(U_{p,q}^{n+1/2}\right) + g\left(U_{p+1,q}^{n+1/2}\right)\right\}. \tag{7.13}$$

7.1.1 Predictor-Step

The conservation law (7.1) is employed to evaluate the values of $U_{j,k}^{n+1/2}$ for $j = p,\, p{+}1,\, k = q,\, q+1$ in (7.10)–(7.13):

$$\begin{aligned} U_{j,k}^{n+1/2} &= U_{j,k}^{n} + \frac{\triangle t}{2}\left(\frac{\partial w}{\partial t}\right)_{j,k}^{n} \\ &= U_{j,k}^{n} - \frac{\triangle t}{2}\left(\frac{\partial f(w)}{\partial x}\right)_{j,k}^{n} - \frac{\triangle t}{2}\left(\frac{\partial g(w)}{\partial y}\right)_{j,k}^{n} + \frac{\triangle t}{2} s\left(U_{j,k}^{n}\right) \\ &= U_{j,k}^{n} - \frac{\triangle t}{2}\left(\sigma^f\right)_{j,k}^{n} - \frac{\triangle t}{2}\left(\sigma^g\right)_{j,k}^{n} + \frac{\triangle t}{2} s\big(U_{j,k}^{n}\big), \end{aligned} \tag{7.14}$$

where σ^f and σ^g are one-dimensional discrete slopes of the fluxes f and g in the x- and y-directions, respectively, which are determined by the non-oscillatory TVD limiters or ENO interpolations. Alternatively, they can also be represented by the corresponding Jacobians

$$\left(\sigma^f\right)_{j,k}^{n} = \left(\frac{\partial f(w)}{\partial w}\right)_{j,k}^{n}\sigma_{j,k}^{x}, \qquad \left(\sigma^g\right)_{j,k}^{n} = \left(\frac{\partial g(w)}{\partial w}\right)_{j,k}^{n}\sigma_{j,k}^{y}, \tag{7.15}$$

where $\sigma_{j,k}^{x}$ and $\sigma_{j,k}^{y}$ are the discrete slopes of U in the x- and y-directions, respectively, Jiang & Tadmor [62]. Nevertheless, in this thesis we will employ only the Jacobian-*free* approach [85].

There remains now the integration of the source term. Its integration also combines contributions from the four intersecting cells that is approximated by the *values at the centres* of the four intersecting cells, $(x_{p+1/4}, y_{q+1/4}, t^{n+1/2})$, $(x_{p+3/4}, y_{q+1/4}, t^{n+1/2})$, $(x_{p+3/4}, y_{q+3/4}, t^{n+1/2})$ and $(x_{p+1/4}, y_{q+3/4}, t^{n+1/2})$, see Fig. 7.1b,

$$\begin{aligned} &\frac{1}{\triangle x \triangle y}\int_{t_n}^{t^{n+1}}\int_{x_p}^{x_{p+1}}\int_{y_q}^{y_{q+1}} s(x,\, y,\, t)\mathrm{d}x\,\mathrm{d}y\,\mathrm{d}t \\ &= \frac{\triangle t}{4}\left\{s(x_{p+1/4},\, y_{q+1/4},\, t^{n+1/2}) + s(x_{p+3/4},\, y_{q+1/4},\, t^{n+1/2})\right. \\ &\quad \left. + s(x_{p+3/4},\, y_{q+3/4},\, t^{n+1/2}) + s(x_{p+1/4},\, y_{q+3/4},\, t^{n+1/2})\right\} \\ &= \frac{\triangle t}{4}\left\{s\left(U_{p+1/4,q+1/4}^{n+1/2}\right) + s\left(U_{p+3/4,q+1/4}^{n+1/2}\right) + s\left(U_{p+3/4,q+3/4}^{n+1/2}\right) + s\left(U_{p+1/4,q+3/4}^{n+1/2}\right)\right\}. \end{aligned} \tag{7.16}$$

Taylor series expansion is used to evaluate the values of $U^{n+1/2}_{p+1/4,q+1/4}$ at the south west intersecting cell

$$\begin{aligned} U^{n+1/2}_{p+1/4,q+1/4} &= U^n_{p,q} + \frac{\triangle x}{4}\left(\frac{\partial w}{\partial x}\right)^n_{p,q} + \frac{\triangle y}{4}\left(\frac{\partial w}{\partial y}\right)^n_{p,q} + \frac{\triangle t}{2}\left(\frac{\partial w}{\partial t}\right)^n_{p,q} \\ &= U^{n+1/2}_{p,q} + \frac{\triangle x}{4}\left(\sigma^x\right)^n_{p,q} + \frac{\triangle y}{4}\left(\sigma^y\right)^n_{p,q}, \end{aligned} \tag{7.17}$$

where $U^{n+1/2}_{p,q}$, defined in (7.14), is employed. Continuing in counterclockwise direction, it follows that

$$U^{n+1/2}_{p+3/4,q+1/4} = U^{n+1/2}_{p+1,q} - \frac{\triangle x}{4}\left(\sigma^x\right)^n_{p+1,q} + \frac{\triangle y}{4}\left(\sigma^y\right)^n_{p+1,q}, \tag{7.18}$$

$$U^{n+1/2}_{p+3/4,q+3/4} = U^{n+1/2}_{p+1,q+1} - \frac{\triangle x}{4}\left(\sigma^x\right)^n_{p+1,q+1} - \frac{\triangle y}{4}\left(\sigma^y\right)^n_{p+1,q+1}, \tag{7.19}$$

$$U^{n+1/2}_{p+1/4,q+3/4} = U^{n+1/2}_{p,q+1} + \frac{\triangle x}{4}\left(\sigma^x\right)^n_{p,q+1} - \frac{\triangle y}{4}\left(\sigma^y\right)^n_{p,q+1}. \tag{7.20}$$

7.1.2 Corrector-Step

Collecting all these results from (7.6)-(7.9) and (7.10)-(7.13) we can summerise as follows: The two-dimensional NOC scheme consists of the *first-order predictor* (7.14) and (7.17)–(7.20) and the *second-order corrector* step,

$$\begin{aligned} U^{n+1}_{p+1/2,\,q+1/2} = &\quad \frac{1}{4}\left\{U^n_{p,q} + U^n_{p+1,q} + U^n_{p+1,q+1} + U^n_{p,q+1}\right\} \\ &+\frac{\triangle x}{16}\left\{\sigma^x_{p,q} - \sigma^x_{p+1,q} - \sigma^x_{p+1,q+1} + \sigma^x_{p,q+1}\right\} \\ &+\frac{\triangle y}{16}\left\{\sigma^y_{p,q} + \sigma^y_{p+1,q} - \sigma^y_{p+1,q+1} - \sigma^y_{p,q+1}\right\} \\ &-\frac{\triangle t}{2\triangle x}\left\{f\left(U^{n+1/2}_{p+1,q}\right) + f\left(U^{n+1/2}_{p+1,q+1}\right) - f\left(U^{n+1/2}_{p,q}\right) - f\left(U^{n+1/2}_{p,q+1}\right)\right\} \\ &-\frac{\triangle t}{2\triangle y}\left\{g\left(U^{n+1/2}_{p,q+1}\right) + g\left(U^{n+1/2}_{p+1,q+1}\right) - g\left(U^{n+1/2}_{p,q}\right) - g\left(U^{n+1/2}_{p+1,q}\right)\right\} \\ &+\frac{\triangle t}{4}\left\{s\left(U^{n+1/2}_{p+1/4,q+1/4}\right) + s\left(U^{n+1/2}_{p+3/4,q+1/4}\right) + s\left(U^{n+1/2}_{p+3/4,q+3/4}\right) + s\left(U^{n+1/2}_{p+1/4,q+3/4}\right)\right\} \end{aligned} \tag{7.21}$$

for the cell-mean value at $(x_{p+1/2},\, q_{q+1/2},\, t^{n+1})$. This results in a heigh-order accurate non-oscillatory scheme. As in the one-dimensional case, presented in Chapter 6, the non-oscillatory behaviour of this scheme also strongly depends on the reconstructed discrete slopes, σ^x, σ^y, σ^f and σ^g.

The CFL Condition

A realistic geometric CFL restriction for the scheme given by (7.14) and (7.21) is

$$\max\left(\frac{\triangle t}{\triangle x}\frac{\partial f}{\partial w},\, \frac{\triangle t}{\triangle y}\frac{\partial g}{\partial w}\right) \le 1/2. \tag{7.22}$$

This condition is confirmed by numerical tests by Jiang & Tadmor [62] with the simple linear oblique advection equation, $\partial w/\partial t + \partial w/\partial x + \partial w/\partial y = 0$.

7.2 2D Shock-Capturing Methods Applied to the Extended Savage-Hutter Equations

In this section we will apply the two-dimensional NOC scheme developed in Section 7.1 to the two-dimensional extended model equations for flow avalanches down curved and twisted channels derived by PUDASAINI & HUTTER [101] as a generalisation of the original Savage-Hutter equations. For this purpose let us consider the model equations (4.85)-(4.87) of Chapter 4 in conservative from. These equations can be written in compact vectorial form, see equation (4.94), as follows:

$$\frac{\partial \mathbf{w}}{\partial t} + \frac{\partial \mathbf{f}\left(\mathbf{w}\right)}{\partial x} + \frac{\partial \mathbf{g}\left(\mathbf{w}\right)}{\partial y} = \mathbf{s}(\mathbf{w}), \tag{7.23}$$

where $\mathbf{w}$ denotes the vector of conservative variables, $\mathbf{f}$ and $\mathbf{g}$ represent the transport fluxes in the x- and y-directions, respectively, and $\mathbf{s}$ means the source term. They are

$$\mathbf{w}=\begin{pmatrix} h \\ m_x \\ m_y \end{pmatrix},\ \mathbf{f}=\begin{pmatrix} m_x \\ m_x^2/h+\beta_x h^2/2 \\ m_x m_y/h \end{pmatrix},\ \mathbf{g}=\begin{pmatrix} m_y \\ m_x m_y/h \\ m_y^2/h+\beta_y h^2/2 \end{pmatrix},\ \mathbf{s}=\begin{pmatrix} 0 \\ hs_x \\ hs_y \end{pmatrix}. \tag{7.24}$$

where the source terms in the momentum balance equations, s_x and s_y, and the parameters β_x and β_y are defined in (4.88)-(4.90), and the equations are computed in the conservative variables h, $m_x = hu$ and $m_y = hv$.

By virtue of (7.21), the cell average $\mathbf{w}^{n+1}_{p+1/2,\,q+1/2}$ at $\left(x_{p+1/2}, y_{q+1/2}, t^{n+1}\right)$ is given by

$$\begin{aligned}
\mathbf{w}^{n+1}_{p+1/2,\,q+1/2} &= \frac{1}{4}\left\{\mathbf{w}^{n}_{p,q}+\mathbf{w}^{n}_{p+1,q}+\mathbf{w}^{n}_{p+1,q+1}+\mathbf{w}^{n}_{p,q+1}\right\} \\
&+\frac{\triangle x}{16}\left\{\mathbf{w}^{x}_{p,q}-\mathbf{w}^{x}_{p+1,q}-\mathbf{w}^{x}_{p+1,q+1}+\mathbf{w}^{x}_{p,q+1}\right\} \\
&+\frac{\triangle y}{16}\left\{\mathbf{w}^{y}_{p,q}+\mathbf{w}^{y}_{p+1,q}-\mathbf{w}^{y}_{p+1,q+1}-\mathbf{w}^{y}_{p,q+1}\right\} \\
&-\frac{\triangle t}{2\triangle x}\left\{\mathbf{f}\left(\mathbf{w}^{n+1/2}_{p+1,q}\right)+\mathbf{f}\left(\mathbf{w}^{n+1/2}_{p+1,q+1}\right)-\mathbf{f}\left(\mathbf{w}^{n+1/2}_{p,q}\right)-\mathbf{f}\left(\mathbf{w}^{n+1/2}_{p,q+1}\right)\right\} \\
&-\frac{\triangle t}{2\triangle y}\left\{\mathbf{g}\left(\mathbf{w}^{n+1/2}_{p,q+1}\right)+\mathbf{g}\left(\mathbf{w}^{n+1/2}_{p+1,q+1}\right)-\mathbf{g}\left(\mathbf{w}^{n+1/2}_{p,q}\right)-\mathbf{g}\left(\mathbf{w}^{n+1/2}_{p+1,q}\right)\right\} \\
&+\frac{\triangle t}{4}\left\{\mathbf{s}\left(\mathbf{w}^{n+1/2}_{p+1/4,q+1/4}\right)+\mathbf{s}\left(\mathbf{w}^{n+1/2}_{p+3/4,q+1/4}\right)+\mathbf{s}\left(\mathbf{w}^{n+1/2}_{p+3/4,q+3/4}\right)+\mathbf{s}\left(\mathbf{w}^{n+1/2}_{p+1/4,q+3/4}\right)\right\}.
\end{aligned} \tag{7.25}$$

Here, $\mathbf{w}^{x}_{j,k}$ and $\mathbf{w}^{y}_{j,k}$ for $j = p,\ p+1$ and $k = q,\ q+1$ are the mean discrete deviators (derivatives) over the cell in the x- and y-directions, respectively,

$$\mathbf{w}^{x}_{j,k} = \boldsymbol{\sigma}^{x}_{j,k}, \qquad \mathbf{w}^{y}_{j,k} = \boldsymbol{\sigma}^{y}_{j,k}. \tag{7.26}$$

Applying the conservation law (7.23) the cell average at time level $t^{n+1/2}$, as in (7.14), is given by

$$\mathbf{w}^{n+1/2}_{j,k} = \mathbf{w}^{n}_{j,k} + \frac{\triangle t}{2}\left(\frac{\partial \mathbf{w}}{\partial t}\right)^{n}_{j,k}, \tag{7.27}$$

where the temporal derivative is approximated by

$$\left(\frac{\partial \mathbf{w}}{\partial t}\right)^n_{j,k} = -\left(\frac{\partial \mathbf{f}}{\partial x}\right)^n_{j,k} - \left(\frac{\partial \mathbf{g}}{\partial y}\right)^n_{j,k} + \mathbf{s}\left(\mathbf{w}^n_{j,k}\right) = -\left(\sigma^{\mathbf{f}}\right)^n_{j,k} - \left(\sigma^{\mathbf{g}}\right)^n_{j,k} + \mathbf{s}\left(\mathbf{w}^n_{j,k}\right). \quad (7.28)$$

Here $\sigma^{\mathbf{f}}$ and $\sigma^{\mathbf{g}}$ are the one-dimensional discrete slopes of the fluxes in the x- and y-directions, respectively. The earth pressure coefficients, K_x and K_y arising in the fluxes (via $\mathbf{f}$ and $\mathbf{g}$) $\beta_x = -\varepsilon g_z K_x$ and $\beta_y = -\varepsilon g_z K_y$, can be determined by the velocities on the adjacent cells with the ad hoc definitions, (4.76), (4.77) viz.,

$$(K_x)_{p,q} = K_x(u_{p+1,q},\, u_{p-1,q}), \quad (7.29)$$

$$(K_y)_{p,q} = K_y(u_{p+1,q},\, u_{p-1,q},\, v_{p,q+1},\, v_{p,q-1}). \quad (7.30)$$

Here u and v are the velocities in the x- and y-directions, respectively, which are determined by the definition of the conservative variables,

$$u_{p,q} = (m_x)_{p,q}/h_{p,q}, \quad v_{p,q} = (m_y)_{p,q}/h_{p,q} \quad \text{for} \quad h_{p,q} \neq 0. \quad (7.31)$$

Remark: *Equation (7.31) indicates that the scheme given by (7.25) suffers from the trivial solution, $0 = 0$, at $h = 0$ for the momentum balance equation. There are two remedies of this problem. (i) A first choice is the addition of a very thin layer of material over the whole computational domain. (ii) Alternatively, one may set all the physical variables equal to zero outside the avalanche domain. The results are then acceptable if there are no jumps in K_x and K_y, i.e., the motion is away from $\partial u/\partial x = 0$ and $\partial v/\partial y = 0$,* [121].

Using the cell reconstructions and the predicted values (7.27) the arguments for the source term in (7.25) are given by

$$\begin{aligned}
\mathbf{w}^{n+1/2}_{p+1/4,q+1/4} &= \mathbf{w}^{n+1/2}_{p,q} + \frac{\triangle x}{4}\mathbf{w}^x_{p,q} + \frac{\triangle y}{4}\mathbf{w}^y_{p,q},\\
\mathbf{w}^{n+1/2}_{p+3/4,q+1/4} &= \mathbf{w}^{n+1/2}_{p+1,q} - \frac{\triangle x}{4}\mathbf{w}^x_{p+1,q} + \frac{\triangle y}{4}\mathbf{w}^y_{p+1,q},\\
\mathbf{w}^{n+1/2}_{p+3/4,q+3/4} &= \mathbf{w}^{n+1/2}_{p+1,q+1} - \frac{\triangle x}{4}\mathbf{w}^x_{p+1,q+1} - \frac{\triangle y}{4}\mathbf{w}^y_{p+1,q+1},\\
\mathbf{w}^{n+1/2}_{p+1/4,q+3/4} &= \mathbf{w}^{n+1/2}_{p,q+1} + \frac{\triangle x}{4}\mathbf{w}^x_{p,q+1} - \frac{\triangle y}{4}\mathbf{w}^y_{p,q+1}.
\end{aligned} \quad (7.32)$$

The CFL Condition

As in (6.75) this NOC scheme must obey the CFL condition

$$\frac{\triangle t}{\triangle x}\,|c^{max}| < \frac{1}{2}, \qquad \text{for all} \quad p,\, q, \quad (7.33)$$

with the global maximum wave speed

$$c^{max} = \max_{all\ p,q}\left(|u_{p,q}| + \sqrt{\beta_x h_{p,q}}\,,\ |v_{p,q}| + \sqrt{\beta_y h_{p,q}}\right) \quad (7.34)$$

over the whole computational domain. The wave speeds are computed in (4.101).

In Chapter 8 we will implement the numerical scheme of this section to solve the two-dimensional avalanche equations (4.85)-(4.87) for a number of cases: (i) for different topographies, (ii) different parameter values, (iii) different numerical methods and (iv) different cell reconstructions.

Chapter 8

Avalanche Simulations Over Curved and Twisted Channels

In this chapter we will implement the numerical schemes developed in Chapter 7 into a computer code in order to simulate avalanching masses. We will make use of the two-dimensional avalanche equations (4.85)-(4.87) for a number of cases: (i) for different numerical methods, (ii) different cell reconstructions, (iii) different topographies and (iv) different parameter values.

8.1 Performance of the Various Numerical Schemes

In order to identify the best numerical scheme that fits well the problem of avalanche dynamics, we first consider a very simple geometric situation in which the basal topography varies only in the down-hill direction but is flat laterally. Let us consider the model equations (4.85)-(4.87). By setting $\theta = 0^\circ$ (where θ, in these equations, appears through η and ζ via the net driving force components (4.89)-(4.90); and the factors β_x and β_y in (4.88)) we obtain a torsion free master curve. Indeed, if we set the parameter $\theta = 0^\circ$ then we get a topography that varies only in the down-hill direction and is flat in the cross-slope direction.

In this section, a simulation example of an avalanche of finite granular mass sliding down an inclined plane and merging continuously into a horizontal plane is presented. A hemispherical shell holding the material together is suddenly released so that the bulk material commences to slide on an inclined flat plane at 35° into a horizontal run-out plane connected by a smooth transition. The computational domain is the rectangle $x \in [0, 30]$ and $y \in [-7, 7]$ in dimensionless length units, where the inclined section lies in the interval $x \in [0, 17.5]$ and the horizontal region lies where $x \geq 21.5$ with a smooth change of the topography in the transition zone, $x \in [17.5, 21.5]$. The inclination angle is prescribed by

$$\tilde{\zeta}(x) = \begin{cases} \tilde{\zeta}_0, & 0 \leq x \leq 17.5\,, \\ \tilde{\zeta}_0(1 - (x - 17.5)/4), & 17.5 < x < 21.5\,, \\ 0^\circ, & x \geq 21.5\,, \end{cases} \tag{8.1}$$

where $\tilde{\zeta}_0 = 35^\circ$. The simulation is performed with an internal angle of friction $\phi = 30^\circ$ and a bed friction angle $\delta = 30^\circ$. The material is suddenly released at $t = 0$ from the

hemispherical shell with an initial radius of $r_0 = 1.85$ in dimensionless length units. The centre of the cap is initially located at $(x_0, y_0) = (4, 0)$.

8.1.1 Numerical Performances

Figures 8.1 and 8.3–8.7 illustrate the thickness contours of the avalanche body at nine time slices as the avalanche slides on the inclined plane into the horizontal run-out zone, obtained with different numerical schemes, for more detail see [130]. If the traditional *central difference scheme* is applied to simulate the avalanche flow, stable numerical simulations can not be performed. For such cases, in order to suppress *numerical oscillations* and avoid possible emerging instabilities, *artifical diffusion* must be incorporated. Figure 8.1 shows numerical results obtained with the central difference scheme in which the artifical diffusion term $\mu_x \partial^2 \mathbf{w}/\partial x^2 + \mu_y \partial^2 \mathbf{w}/\partial y^2$ is added to the right-hand sides of (7.23) with viscosities $\mu_x = \mu_y = 0.02$. For smaller viscosities ($\mu_x < 0.018$, $\mu_y < 0.018$) the simulation becomes unstable. The central difference schemes, as well as many other traditional second- or higher-order difference methods, introduce *dispersive effects* that are susceptible to numerical instabilities and lead to unphysical oscillations in the numerical solution. These are usually located behind the advancing front and damped with growing distance from the front (for $t = 3$ to $t = 12$ in Fig. 8.1), although for this case certain artifical diffusion has been incorporated. The corresponding three-dimensional evolution of the avalanche geometry at three different dimensionless times $t = 6$, 9, 12 are shown in Fig. 8.2. The unphysical oscillations behind the moving front are obvious. If sufficiently large artifical diffusion is added to dampen the spurious oscillations, a solution without superimposed numerical oscillations can be reached. However, in such cases, the corresponding solution will be highly diffusive, similar to that obtained with the first-order accuracy upstream scheme (Fig. 8.3), in which additional diffusion is inherent. Although traditional first-order finite difference methods, e.g. the first-order upstream scheme, are monotonic without numerical oscillations and stable, they are strongly dissipative, causing the solution to become smeared out and often grossly inaccurate. Due to the dissipative nature of the upstream difference scheme, the simulated granular flow spreads out over a much wider area than that with high-order difference schemes. At some time levels, e.g. for $t = 9$ and $t = 18 - 24$ in Fig. 8.3, the extents of the granular mass exceed the chosen computational domain. If one would like to study the numerical solution of this upstream scheme more exactly, a relatively larger (lateral) computational domain should be chosen.

The numerical results obtained by the use of the NOC (Non-Oscillatory Central Differencing) scheme with different cell reconstruction methods – three TVD limiters: Superbee, Woodward and Minmod as well as the third-order ENO cell reconstruction, are shown in Figs. 8.4–8.7. Because the Superbee limiter is the least diffusive among the second-order TVD limiters, the solution with this limiter still exhibits oscillations (for $t = 9$ and $t = 12$ in Fig. 8.4). In fact, the Superbee limiter is often anti-diffusive, i.e., it has a tendency to steepen gradients. The deposition in Fig. 8.4 for $t = 18 - 24$ has a steepened border in comparison with the results in Figs. 8.5–8.7 obtained with other high-resolution schemes.

The NOC schemes with the Woodward TVD limiter (Fig. 8.5), the ENO cell reconstruction (Fig. 8.6) or the Minmod TVD limiter (Fig. 8.7) show fairly similar numerical results, in which little numerical oscillations occur and simultaneously numerical dissipation is negligibly small. However, we recommend to apply the NOC scheme with the

Minmod TVD limiter to simulate the granular avalanche flow described by the extended Savage-Hutter theory, because in some other test examples, e.g. with a larger inclined angle of the chute plane, some small numerical oscillations are also visible in the solutions obtained with the Woodward limiter and the ENO cell reconstruction.

From Figs. 8.5–8.7 it can be seen that, once the cap is opened, the avalanche accelerates downslope due to gravity and extends until the front reaches the horizontal run-out zone. The front comes (almost) to rest when $t > 9$ but the part of the tail accelerates further down, and the avalanche body contracts. Once the velocity changes from supercritical to subcritical, a shock wave develops around the end of the transition zone at $x = 21.5$ for $t = 12$. With the approaching mass from the tail, the shock wave propagates backwards from $t = 12$ to $t = 24$. At $t = 24$, the shock front reaches almost the beginning of the transition zone at $x = 17.5$ and the final deposition of the granular mass is nearly attained. Figure 8.8 illustrates the depth profiles of the granular flow along the central line $y = 0$ simulated by the NOC scheme with the Minmod limiter for the same times as in Fig. 8.7. The granular mass released from the cap extends on the inclined plane until the front reaches the horizontal run-out zone. Here the basal friction is sufficiently large to bring the front of the granular flow to rest. At this stage, a *surge wave* is created at $t = 12$, which moves a short distance upward as can clearly be seen by comparing the humps for $t = 12$ to $t = 24$. A more direct overview of the granular avalanche flow can be obtained from the evolution of the three-dimensional avalanche geometries displayed in Fig. 8.9.

8.1.2 Choice of the Numerical Scheme

Thus, we have seen that the NOC scheme with Minmod TVD limiter demonstrates the best numerical performance for simulating avalanche dynamics among all other limiters and the ENO cell reconstructions. For this reason, in the rest of this thesis, we will implement only the NOC scheme together with the Minmod limiter for the numerical simulations of avalanches over different bed topographies and parameter values.

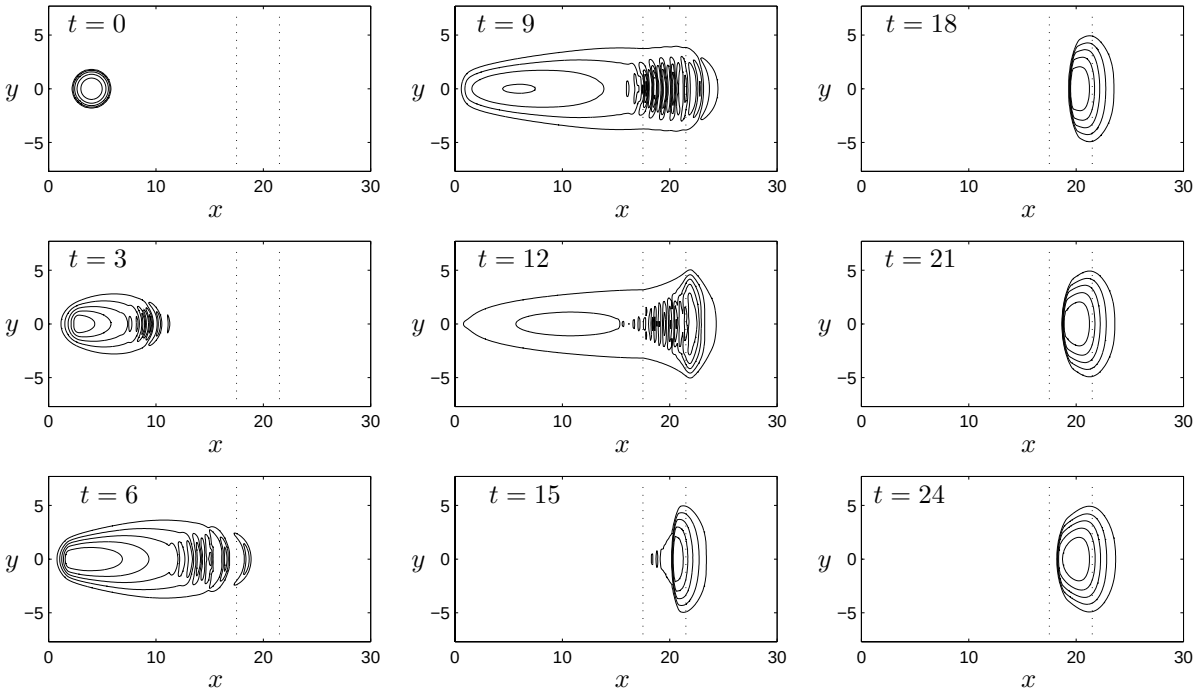

Figure 8.1: Thickness contours of the avalanche at nine different dimensionless times $t = 0$, 3, 6, 9, 12,-15, 18, 21, 24, obtained with the **traditional central difference scheme**. The transition zone from the inclined plane to the horizontal plane lies between the two dotted lines. In order to achieve a stable simulation, the artifical numerical diffusion term $\mu_x \partial^2 \mathbf{w}/\partial x^2 + \mu_y \partial^2 \mathbf{w}/\partial y^2$ must be incorporated in (7.23) with viscosities $\mu_x \geq 0.018$, $\mu_y \geq 0.018$. Here we choose $\mu_x = \mu_y = 0.02$. Nevertheless, large numerical oscillations still exist

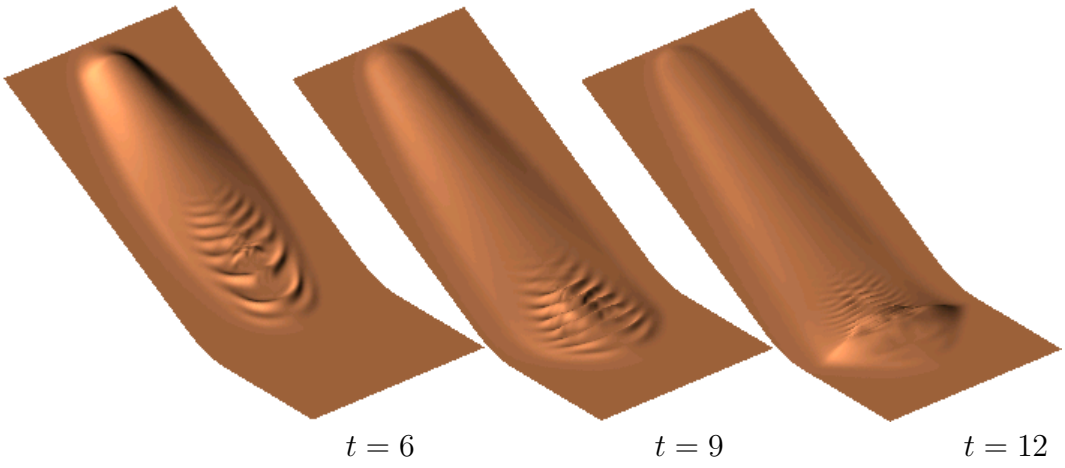

Figure 8.2: Three-dimensional geometries of the avalanche at three different dimensionless times $t = 6$, 9, 12, obtained with the **traditional central difference scheme** as in Fig. 8.1. Considerable numerical oscillations can be observed

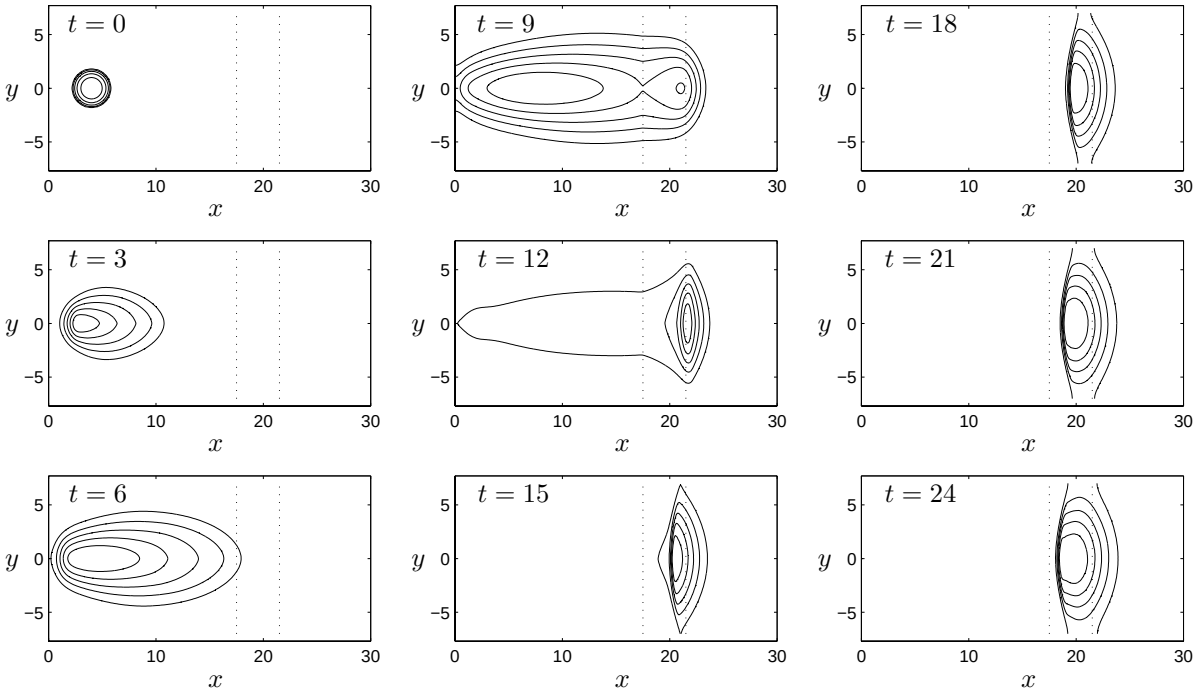

Figure 8.3: Thickness contours of the avalanche at nine different dimensionless times $t = 0$, 3, 6, 9, 12,-15, 18, 21, 24, obtained with the **traditional upstream difference scheme**. The zone between the two dotted lines is the transition zone from the inclined plane to the horizontal plane. The scheme is obviously very diffusive

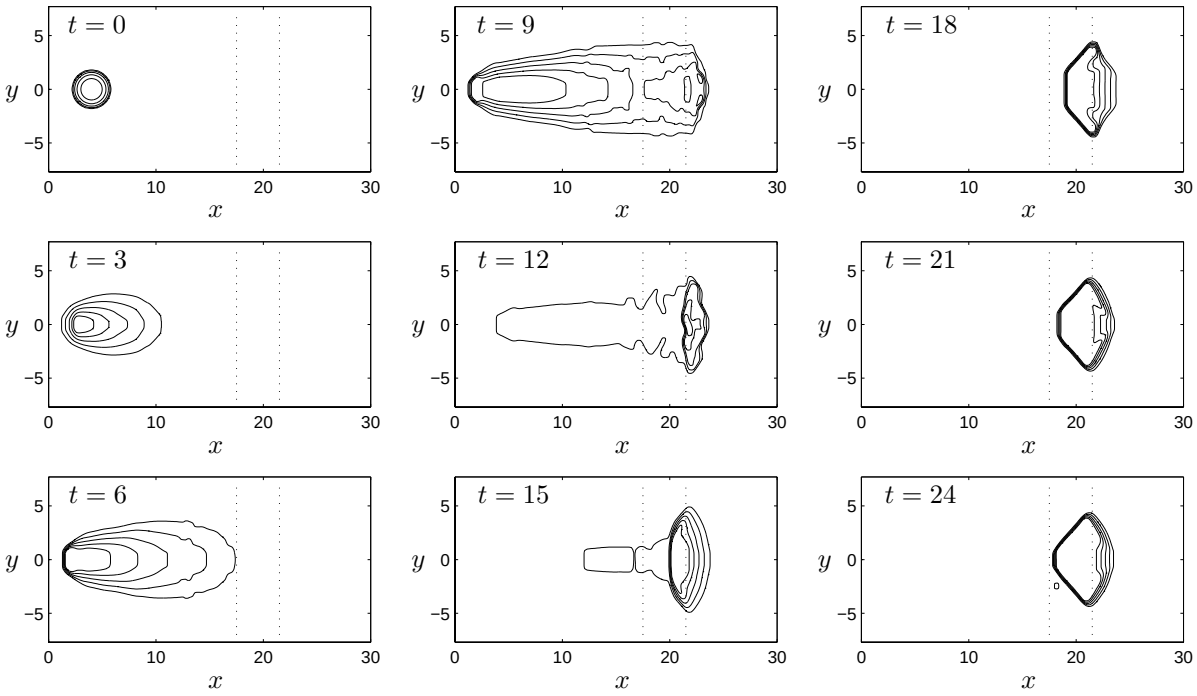

Figure 8.4: Thickness contours of the avalanche at nine different dimensionless times $t = 0$, 3, 6, 9, 12,-15, 18, 21, 24, obtained with the **NOC scheme** and the **Superbee limiter**. The zone between the two dotted lines is the transition zone from the inclined plane to the horizontal plane. Because the Superbee limiter is the least diffusive or even anti-diffusive, some numerical oscillations still occur and even large gradients are recorded

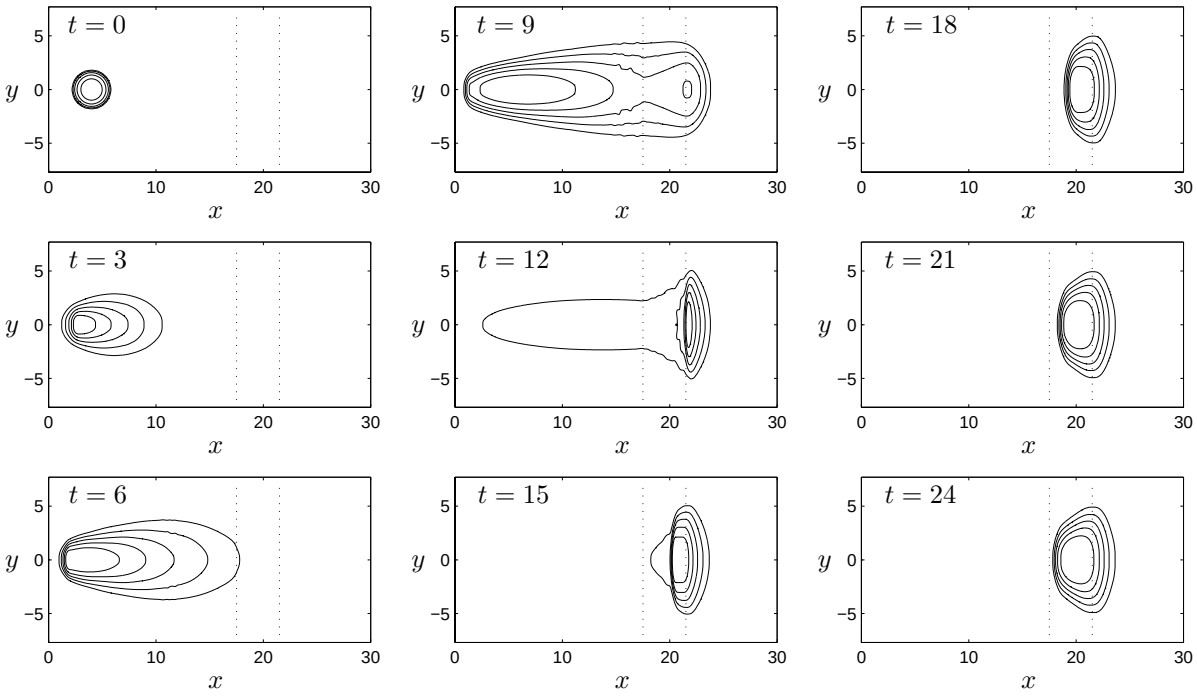

Figure 8.5: Thickness contours of the avalanche at nine different dimensionless times $t = 0$, 3, 6, 9, 12,-15, 18, 21, 24, obtained with the **NOC scheme** and the **Woodward limiter**. The zone between the two dotted lines is the transition zone from the inclined plane to the horizontal plane. With this TVD limiter satisfactory numerical results can be achieved, although some small oscillations still exist

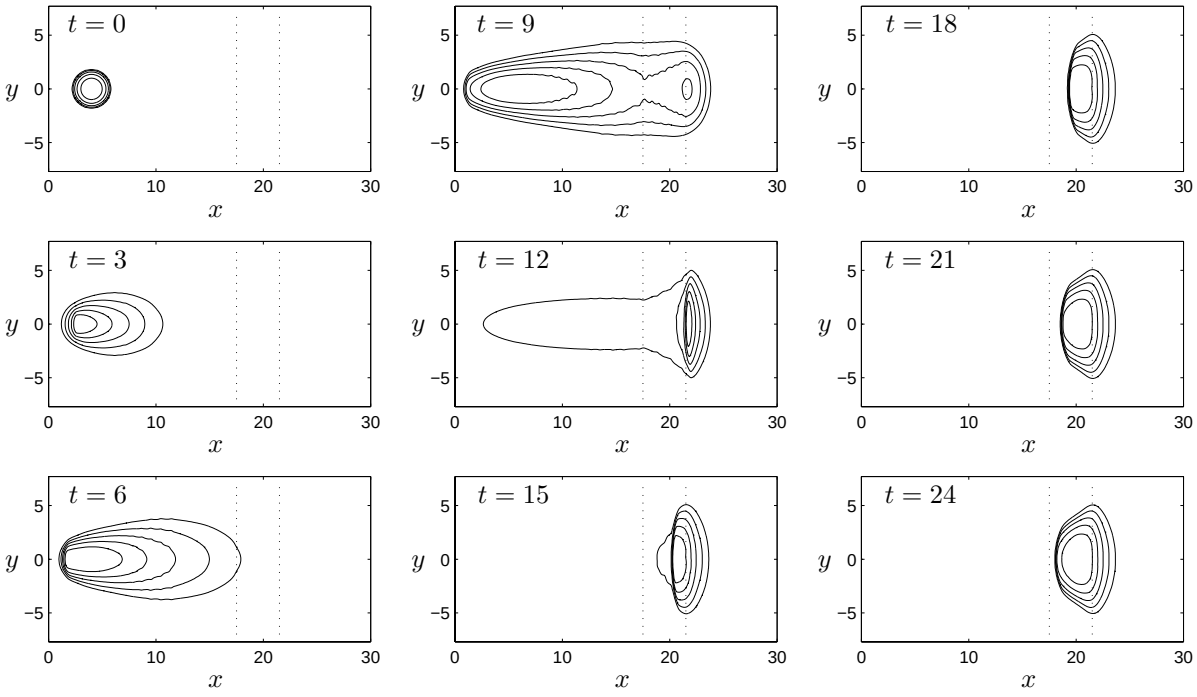

Figure 8.6: Thickness contours of the avalanche at nine different dimensionless times $t = 0$, 3, 6, 9, 12,-15, 18, 21, 24, obtained with the **NOC scheme** and the **third-order ENO cell reconstruction**. The zone between the two dotted lines is the transition zone from the inclined plane to the horizontal plane. This scheme can provide fairly satisfactory numerical results

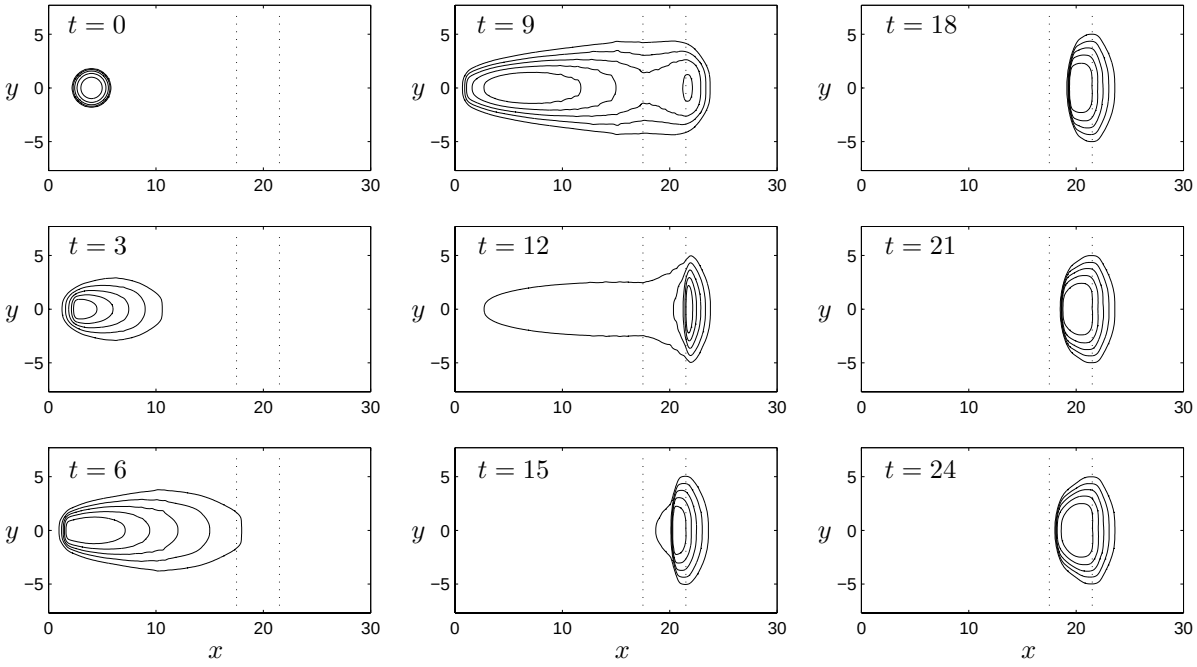

Figure 8.7: Same as in Fig. 8.6 but with the **NOC scheme** and the **Minmod limiter**. The scheme is demonstrated to be the most favourable in treating these hyperbolic avalanche equations, including the cases with various other parameters

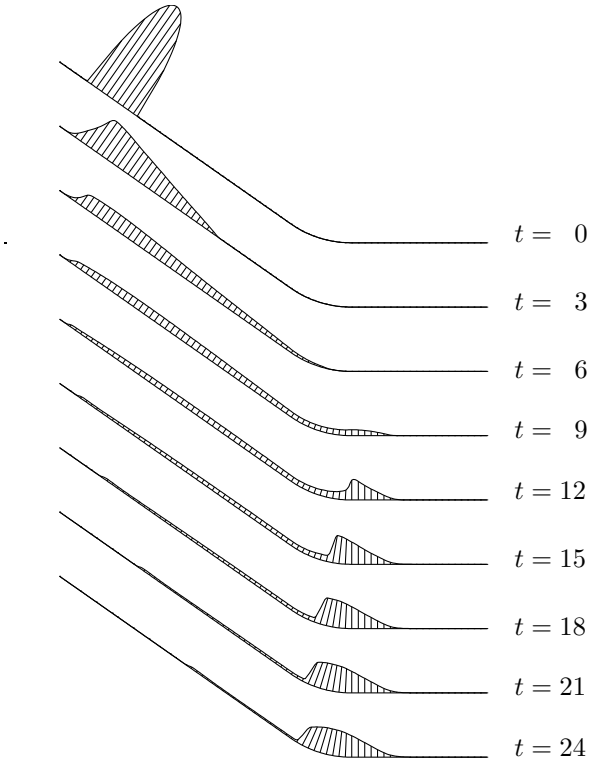

Figure 8.8: Avalanche thickness along the central line of the flow, $y = 0$, at different dimensionless times obtained with the **NOC scheme** and the **Minmod limiter**. Since compared to the length the deposited height of the avalanche is very small, the height is four times exaggerated. As the front reaches the run-out zone and comes to rest, the rear part of the avalanche accelerates further and the avalanche body contracts. When supercritical flow merges into a region of subcritical flow, a shock wave develops, which moves upward. We do not explicitly see here the volume preserving of the material since we have plotted only the central section of the avalanche in the vertical plane that contains the talweg

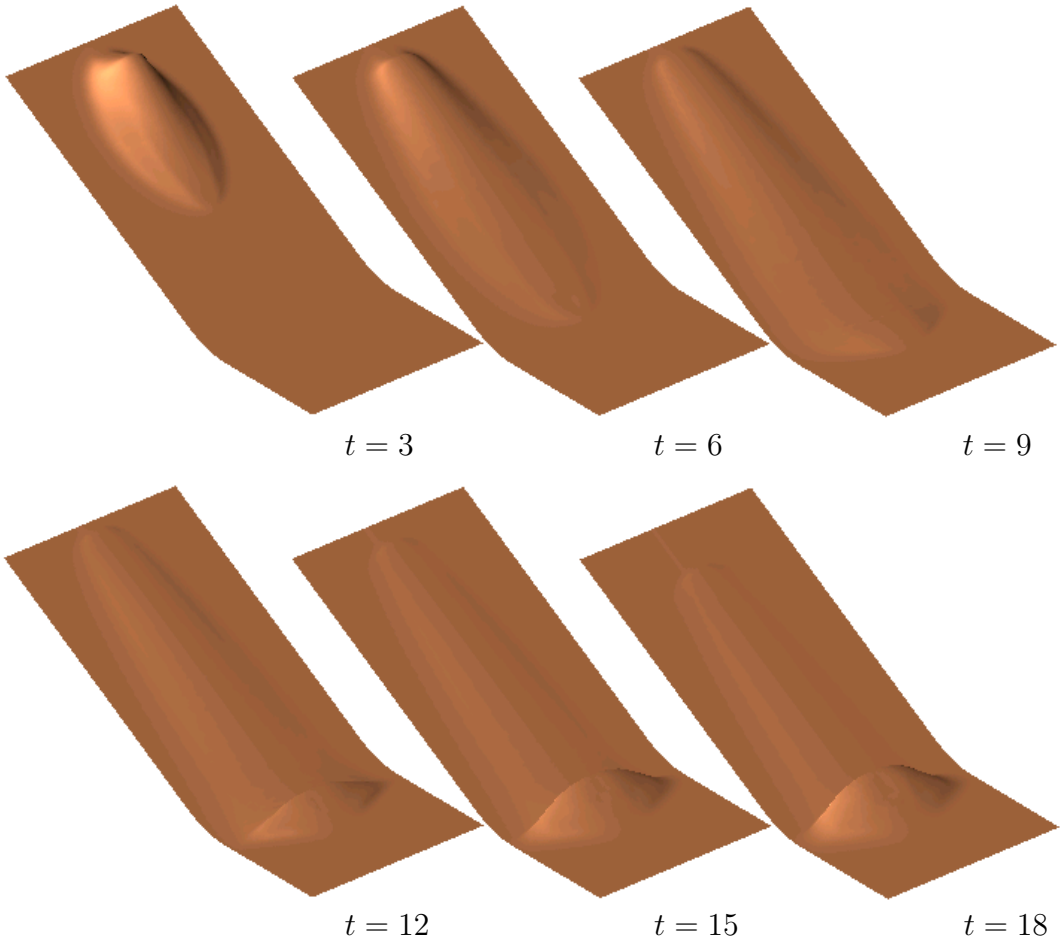

Figure 8.9: Three-dimensional geometries of the avalanche at six different dimensionless times $t = 3, 6, 9, 12, 15, 18$, obtained with the **NOC scheme** and the **Minmod limiter** as in Figs. 8.7 and 8.8

8.2 Effects of Topographic Variations

8.2.1 Constant Cross-Slope Curvature

In order to further test the model equations (4.85)-(4.87) of Chapter 4, we consider an idealised mountain subregion in which the non-twisted talweg is defined by the slope function

$$\tilde{\zeta}(x) = \begin{cases} \tilde{\zeta}_0, & 0 \le x \le x_l, \\ \tilde{\zeta}_0 \left(\dfrac{x_r - x}{x_r - x_l} \right), & x_l \le x \le x_r, \\ 0^\circ, & x \ge x_r, \end{cases} \tag{8.2}$$

where $\tilde{\zeta}_0 = 45^\circ$ is the straight upper part of the talweg which merges into a horizontal run-out plane as shown in Fig. 4.10a, and $x_l = 11.5$ and $x_r = 14.5$ are the (non-dimensional) initial and final points of the continuous transition. The azimuthal angle θ (which includes the cross-slope curvature) is confined to the interval $[-14.32^\circ, 14.32^\circ]$ and the non-dimensional distance is set to $z_T = 20$, corresponding to $y \in [-5, 5]$, see Fig. 4.10b. A hemi-spherical cap with non-dimensional radius $R_0 = 0.98$ holding the granular material in it is placed at $(x_0, y_0) = (3.0, 0.0)$ of the chute and suddenly released. The bulk body commences to slide and deform continuously along the chute unless the bed friction is smaller than the down-slope component of gravity. The values of the material parameters are chosen as $\delta = 33^\circ$ and $\phi = 43^\circ$ which correspond to *marble chips* of mean diameter $2 - 4$ mm [102].

Figure 8.10 depicts the thickness contours of the avalanching body at 10 non-dimensional time steps in a cylindrically curved channel in the down-hill direction, see Fig. 4.10. The first four panels in this figure clearly show that once the cap is opened, the avalanche accelerates and spreads rapidly in the downslope direction due to the channelling effect in the cross-slope direction. The avalanche decelerates rapidly as soon as it enters the run-out zone, from the fourth panel for $t > 4.5$. Due to the continued mass flux from the tail, its front is then able to spread out laterally as seen in panels $5 - 7$. After $t = 7.5$, due to the channelling effect of the cross-section, the tail of the avalanche is reducing in width, but the head of the avalanching body is expanding in width in the run-out zone. The curvature of the transition zone induces a shock associated with the height of the avalanche and moving upstream from time $t = 9.0$ onward. The avalanche comes to rest after $t = 13.5$. The first three panels of Fig. 8.10 indicate that due to the dilatations, the granular body is extending in all directions, mainly in the down-hill direction. Although the front is descending rapidly, the tail moves upward in the beginning because of the earth pressure. At $t = 4.5$ the front reaches the transition zone while the tail also starts to move downward. At $t = 6.0$, the front part of the body has fully reached the transition zone. Therefore the mass at the front is contracting due to the effect of the passive earth pressure coefficient, but the mass in the tail is still extending. At $t = 7.5$, deposition of the mass starts near the vicinity of the lower end of the transition zone. Owing to the effect of the curvature, the flowing body starts contracting longitudinally but extending laterally. After $t = 9.0$, a steep surface (height) gradient starts to develop on the tail side of the avalanche. Although the front of the body is almost at stand still the mass from the tail is continuously flowing down and is deposited on the tail side of the body. This is the main mechanism for the development of the shock front moving upstream. The physical

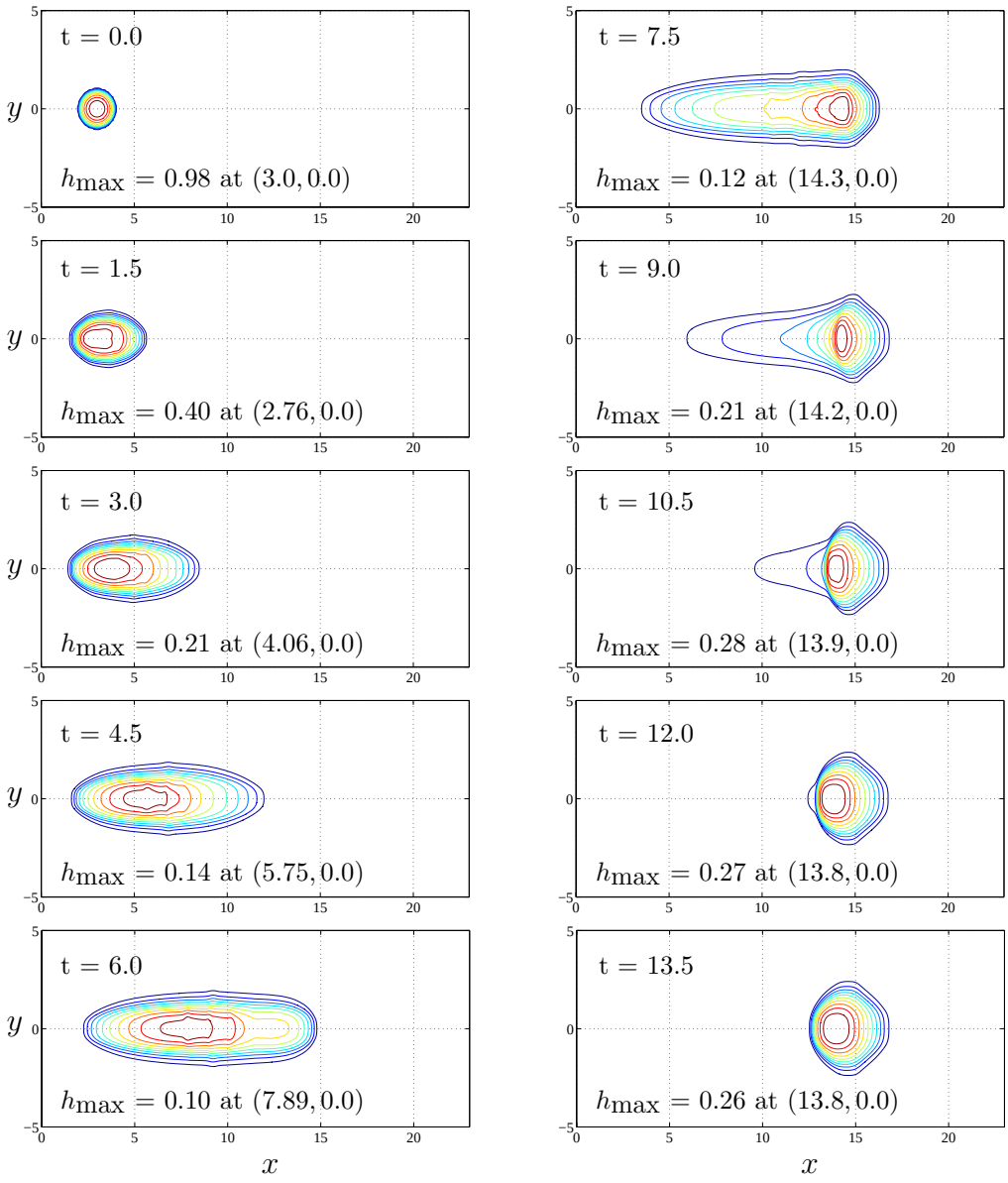

Figure 8.10: A sequence of numerical snapshots of avalanching motion of a granular material with internal and basal friction angles $\phi = 43°$ and $\delta = 33°$, for different time points. The contours of equal thickness are plotted at ten time intervals using "unrolled" projected non-dimensional curvilinear coordinates (x, y). The transition zone lies between $x = 11.5$ to $x = 14.5$. The 45° inclined section lies on the left and the horizontal part lies on the right of each panel. The talweg of the valley is indicated by the line $y = 0$. The panels thus demonstrate the deformation and settling of avalanches in cylindrically curved (both in the down-slope and cross-slope directions) channels

explanation for this is that from the front there is a strong resistive force from the bed which prevents the body from further sliding. So, mass arriving from the upper part of the channel must be deposited at the back side of the body. Consequently, the stopped body must extend upward. The last three panels show the continuous development of the upward moving shock. At the same time, there is almost no motion at the front. Due to the partial lateral confinement, the extension of the body in the cross-slope direction is almost negligible.

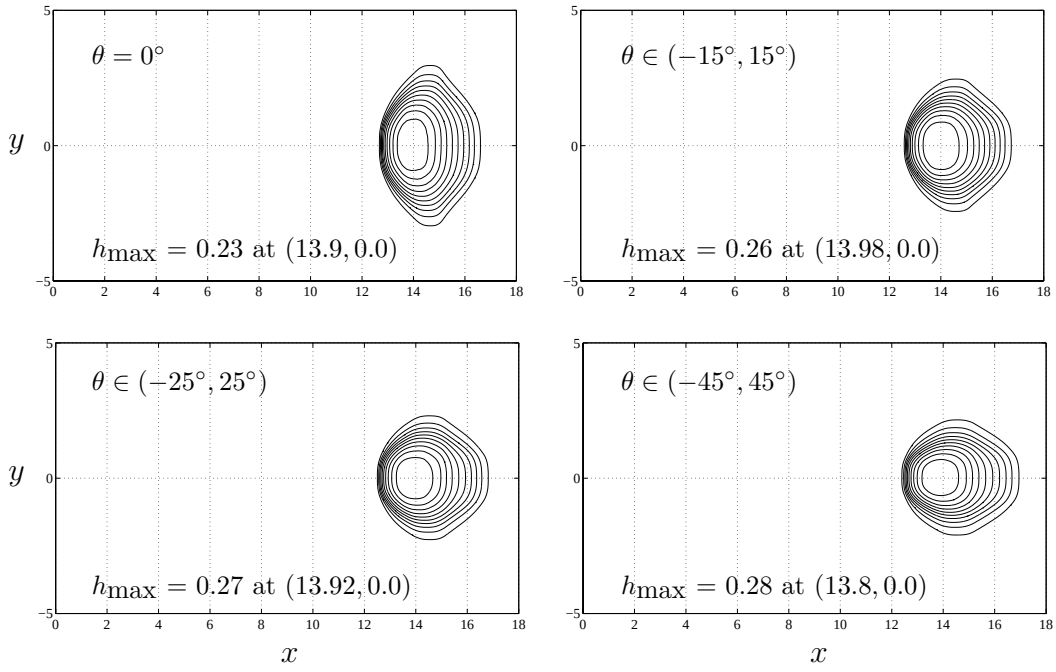

Figure 8.11: Channelling effects: Parameter values are as in Fig. 8.10. The contours represent the final deposits of identical avalanche masses for four different channel widths corresponding to the parameter θ. As the value of the parameter θ increases the width of the channel decreases. Consequently, the granular materials tend to accumulate around and along the talweg of the channel, the geometries of the deposited piles are changed, both the pile heights and the run-out distances increase

Figure 8.11 depicts the channelling effects for different channel widths. Parameter values are as in Fig. 8.10. The contours represent the final deposits of the avalanches for four different channel curvatures. As the value of the parameter θ increases, the lateral curvature increases and the width of the channel decreases. The values of $\theta = 0°$, $15°$, $25°$ and $45°$ correspond to the non-dimensional distances (representing the radius of curvature of the lateral bed profile) ∞, 19.1, 11.46 and 6.4, respectively, while the range of y is kept fixed as before, i.e. $y \in [-5, 5]$. Consequently, with the increase of θ the granular materials tend to accumulate around and along the talweg of the channel, the geometries of the deposited piles are changed, both the pile heights and the run-out distances increase considerably. This effect is directly associated with the lateral component of the gravitational acceleration (g_y) which depends on the lateral curvature (this was always zero in previous extensions of the theory).

Dispersion of the Masses

In order to analyse the dispersion of the avalanching mass quantitatively we consider the total volume ($V = \int h(x, y)\, dx\, dy$) and define the center of the mass as follows:

$$(\overline{x},\ \overline{y}) = \left(\frac{1}{V} \int x\, h(x, y)\, dx\, dy,\ \underbrace{\frac{1}{V} \int y\, h(x, y)\, dx\, dy}_{= 0 \text{ by symmetry}} \right). \tag{8.3}$$

Table 8.1: The center of mass of the avalanching body at different non-dimensional time steps t and azimuthal angles θ. The first and the second coordinates in each column represent the center of mass in the x- and y-directions, respectively, as predicted by formula (8.3)

	$\theta = 0°$	$\theta \in (-15°, 15°)$	$\theta \in (-25°, 25°)$	$\theta \in (-45°, 45°)$
t = 3.0	(4.7, 0.0)	(4.7, 0.0)	(4.6, 0.0)	(4.7, 0.0)
t = 6.0	(8.8, 0.0)	(8.7, 0.0)	(8.7, 0.0)	(8.8, 0.0)
t = 9.0	(13.0, 0.0)	(13.0, 0.0)	(12.9, 0.0)	(13.0, 0.0)
t = 12.0	(14.3, 0.0)	(14.3, 0.0)	(14.3, 0.0)	(14.3, 0.0)
t = 13.5	(14.4, 0.0)	(14.4, 0.0)	(14.4, 0.0)	(14.4, 0.0)

Table 8.2: Same as in Table 8.1 but for the dispersion as predicted by formula (8.4)

	$\theta = 0°$	$\theta \in (-15°, 15°)$	$\theta \in (-25°, 25°)$	$\theta \in (-45°, 45°)$
t = 3.0	(1.60, 0.75)	(1.60, 0.72)	(1.59, 0.70)	(1.63, 0.67)
t= 6.0	(2.99, 0.95)	(3.00, 0.81)	(2.98, 0.76)	(3.04, 0.69)
t= 9.0	(2.53, 1.09)	(2.55, 0.89)	(2.57, 0.82)	(2.59, 0.73)
t= 12.0	(0.97, 1.18)	(1.01, 0.97)	(1.04, 0.91)	(1.10, 0.84)
t= 13.5	(0.86, 1.20)	(0.91, 1.00)	(0.95, 0.95)	(1.02, 0.89)

The dispersion of the deformable granular body can then be computed by the following (standard deviation) formula (where "dis" stands for dispersion):

$$(x_{\text{dis}},\, y_{\text{dis}}) = \left(\sqrt{\frac{1}{V} \int (x - \overline{x})^2 \; h(x,y)\, dx\, dy},\; \sqrt{\frac{1}{V} \int (y - \overline{y})^2 \; h(x,y)\, dx\, dy} \right). \qquad (8.4)$$

Tables 8.1 and 8.2 represent data sets for the center of mass and the dispersion of the sliding and deforming granular body for different non-dimensional time steps and azimuthal angles. Other parameter values are as in Fig. 8.11. Analysing these tables we draw the following conclusions: (i) The center of mass is almost independent of the azimuthal angle θ, at all times. The dispersion along the down-hill direction first increases then decreases but the dispersion in the cross-hill direction increases monotonically for all values of θ. (ii) In general, the dispersion along the down-hill direction increases as θ increases but this relation is reversed for the dispersion in the cross-slope direction, as expected. (iii) Finally, since the channel is flatter around the talweg and has larger cross-slope gradients at the outer rims along the down-hill direction than elsewhere, dispersion relations in both directions are more pronounced in the two panels in the first row than in the two panels in the last row of Fig. 8.11; this is exactly what is quantitatively shown in Table 8.2.

8.2.2 Variable Cross-Slope Curvature

Until now, only numerical results of an avalanche of finite granular mass sliding down an inclined surface were demonstrated, in which there exists no variation of topography in the cross-slope direction. In nature, the events of avalanches often happen in a valley; for

such cases lateral variations of the topography should be considered. In the last section we considered the case in which the bed topography had a constant cross-slope curvature forming a uniform cylindrical channel. In this section we deal with a more general case in which the bed topography contains variable curvature also in the cross-slope direction. The cross-slope curvature can be made variable by defining the parameter θ as a function of x and y. Let us consider a bed topography whose upper part is a cylindrical channel which merges continuously into an open flat run-out zone according to

$$\theta(x,y) = \begin{cases} \dfrac{y}{z_T}, & 0 \le x \le x_l, \\ \dfrac{y}{z_T} f(x), & x_l \le x \le x_r, \\ 0^\circ, & x \ge x_r, \end{cases} \tag{8.5}$$

where z_T is the distance between the master curve and the talweg in the upper inclined part of the channel (hence a constant) and $f(x) = \sin\tilde{\zeta}(x)/\sin\tilde{\zeta}_0$, where $\tilde{\zeta}_0$ is the inclination angle of the upper part of the channel. This implies that $f = 1$ at x_l. Thus, the continuous transition of the parameter θ from its higher value (y/z_T) in the upper part to zero value in the open run-out zone constitutes a required three-dimensional channel which has variable curvature both in the longitudinal as well as lateral direction.

For the numerical simulation we choose the parameter values as follows: $x_l = 15$ and $x_r = 20$ are the (non-dimensional) initial and final points of the continuous transition. The azimuthal angle θ (which includes the cross-slope curvature) in the upper part of the channel is confined to the interval $[-45^\circ, 45^\circ]$ and the non-dimensional distance is set to $z_T = 7.6$, corresponding to $y \in [-6, 6]$, see Fig. 4.10b. A hemi-spherical cap with non-dimensional radius $R_0 = 1.75$ holding the granular material in it is placed at $(x_0, y_0) = (5.0, 0.0)$ of the chute and suddenly released. The bulk body commences to slide and deform continuously along the chute unless the bed friction is smaller than the down-slope component of gravity. The values of the material parameters are chosen as $\delta = 27^\circ$ and $\phi = 37^\circ$ which correspond to *Vestolen*, a sort of plastic particles of lens-like shape and 4 mm diameter on *drawing paper*. The inclination angle of the upper part of the channel with the horizontal is $\tilde{\zeta} = 50^\circ$.

It is interesting to make a comparative study of the avalanching motion among the three channels: (i) a cylindrical channel merging into the run-out zone that always consists of a constant cross-slope curvature (i.e., the constant channel width), (ii) a channel with continuously varying cross-slope curvature given by (8.5) so as to form an open divergent channel that continuously transits to the horizontal run-out area, and (iii) a rolled surface (see, Figs. 3.6 and 4.1) which is curved down-slope as before but entirely flat laterally. The dynamics of the avalanche in the channel with a constant cross-slope curvature is presented in Fig. 8.12. Since there is a strong lateral curvature forming a narrow channel the granular material is not able to spread considerably in the cross-slope direction. However, such a lateral spread is pronounced a bit just after the release (non-dimensional time, $t = 1.5, 3$) and just before the deposit (non-dimensional time, $t = 10.5, 12, 15$, due to the effect of the down-hill curvature) of the bulk material. Therefore, the dynamics is mainly dominated by the extension and contraction of the avalanching and deforming body parallel to the direction of the talweg of the channel. On the other hand, the dynamics is completely different for the flow in the channel with variable cross-slope

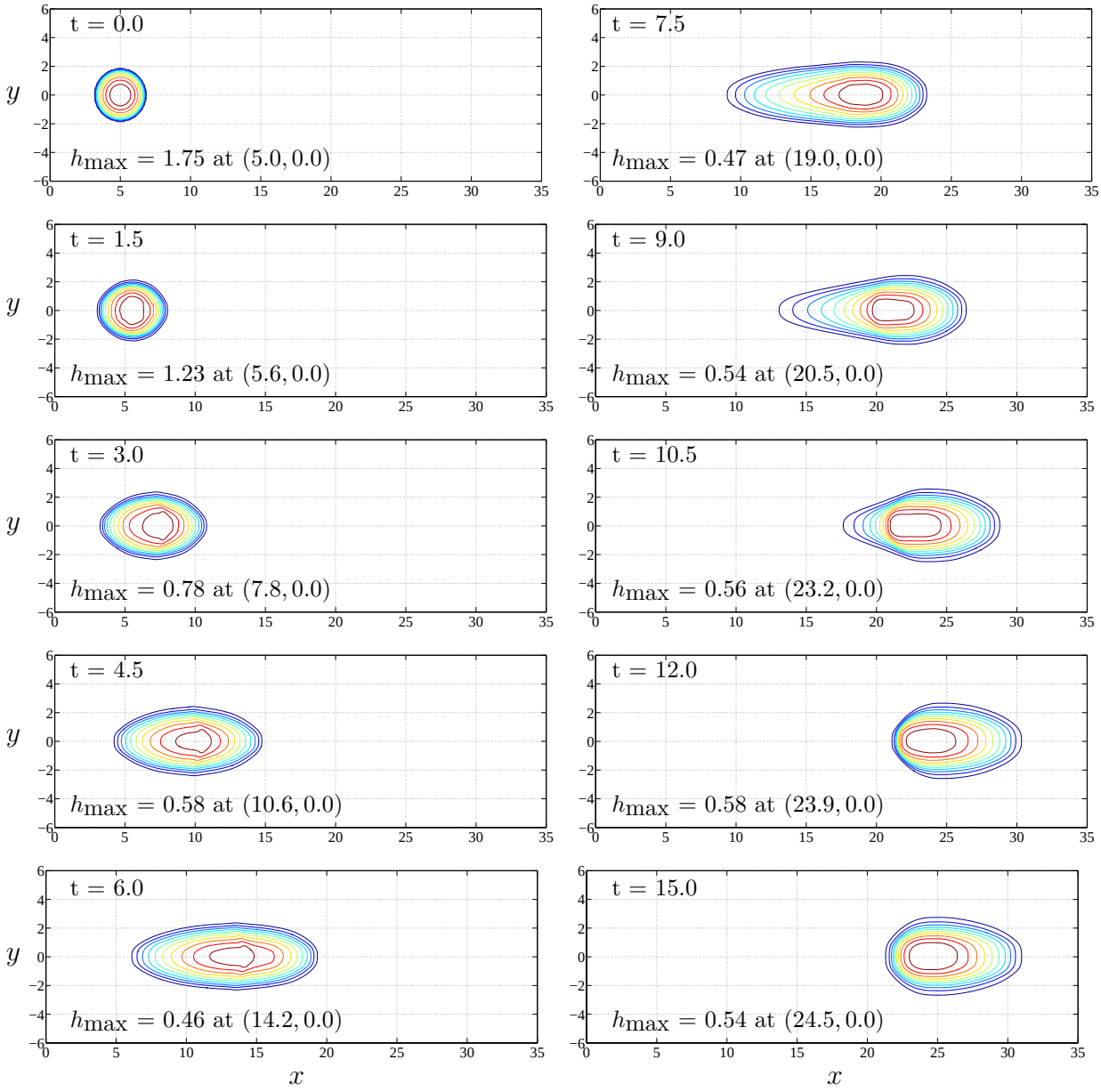

Figure 8.12: A sequence of numerical snapshots of avalanching motion of a granular material with internal and basal friction angles $\phi = 37°$ and $\delta = 27°$, for different time points. The contours of equal thickness are plotted at ten time intervals using "unrolled" projected non-dimensional curvilinear coordinates (x, y). The transition zone lies between $x = 15$ to $x = 20$. The 50° inclined section lies on the left and the horizontal part lies on the right of each panel. The talweg of the valley is indicated by the line $y = 0$. The panels thus demonstrate the deformation and settling of avalanches in cylindrically curved (both in the down-slope and cross-slope directions) channels

curvature. Results are presented in Fig. 8.13. The channel width remains constant in the range $x \in [0, 15]$. It is flattened continuously in the range $x \in [15, 20]$ and, afterward, the section of the bed topography is a part of the horizontal plane. Till time $t = 6$ the contours representing the avalanche geometry are the same as in Fig. 8.12. The results are completely different after time $t = 7.5$. Since the channel is continuously opened and ultimately completely flattened in the lateral direction to the horizontal run-out area, the

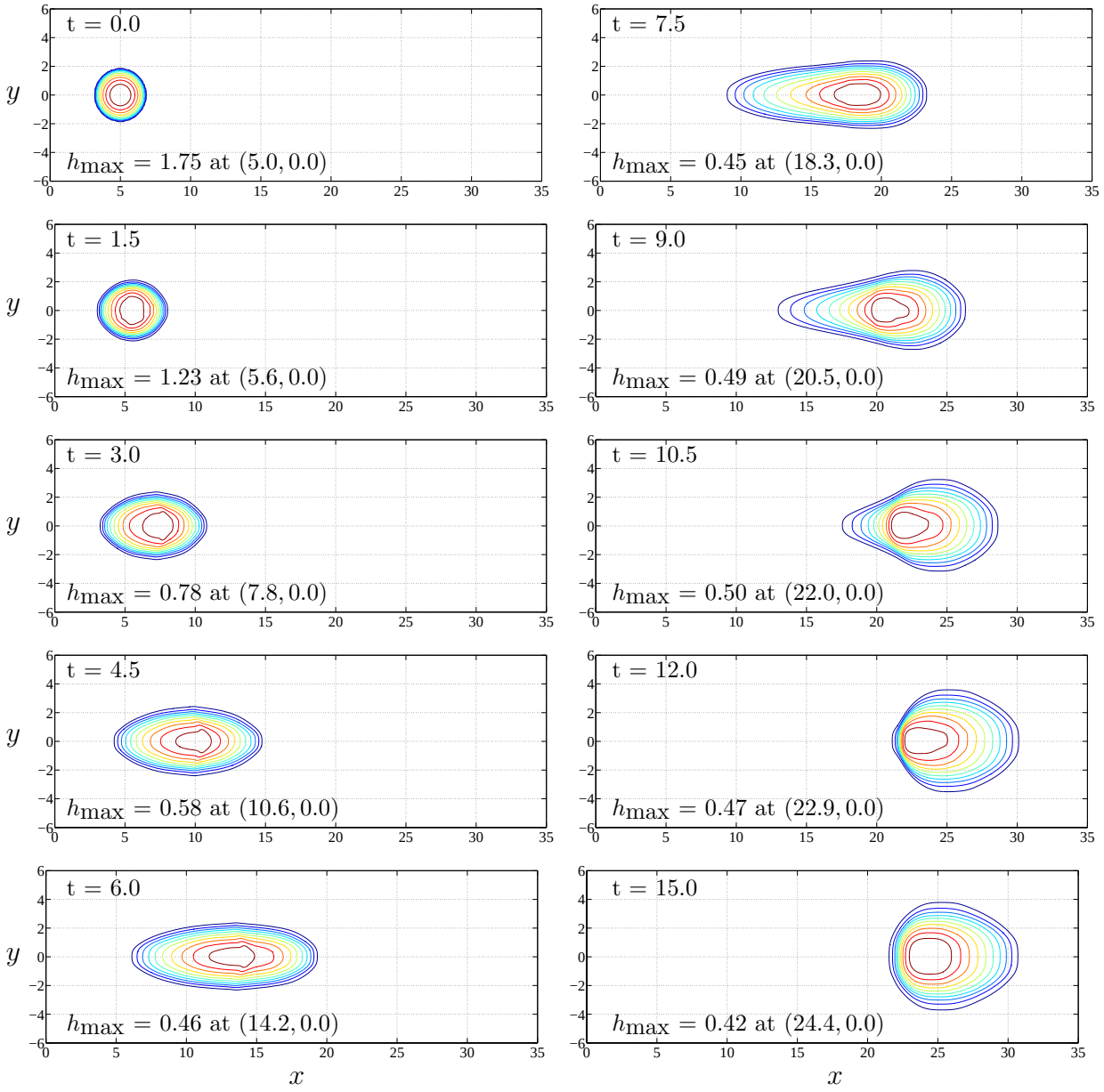

Figure 8.13: Same as in Fig. 8.12 but with variable lateral curvature given by (8.5) so that the upper cylindrical channel merges continuously into an open fan-like horizontal run-out zone

avalanching body spreads rapidly in the lateral direction. However, there is not such a big difference of the dispersion in the longitudinal direction. Similarly, Fig. 8.14 records the motion of an avalanche over the bed topography which is curved down-slope as before but completely flat in the cross-slope direction, i.e., with zero lateral curvature over the whole flow domain. Since the channel is completely unconfined in the lateral direction the avalanching mass is continuously extending in the lateral direction until it comes to rest. Also, the body is extending in the down-hill direction until it reaches the continuous transition zone. Afterwards, as in other cases, the body starts decelerating and comes to rest. A more detailed comparison of the final deposits is presented in Fig. 8.15. It shows the final deposits at time $t = 15$ in Figs. 8.12, 8.13 and of the avalanche over the channel of which the cross-slope curvature is always zero, Fig. 8.14, (i.e., the channel that

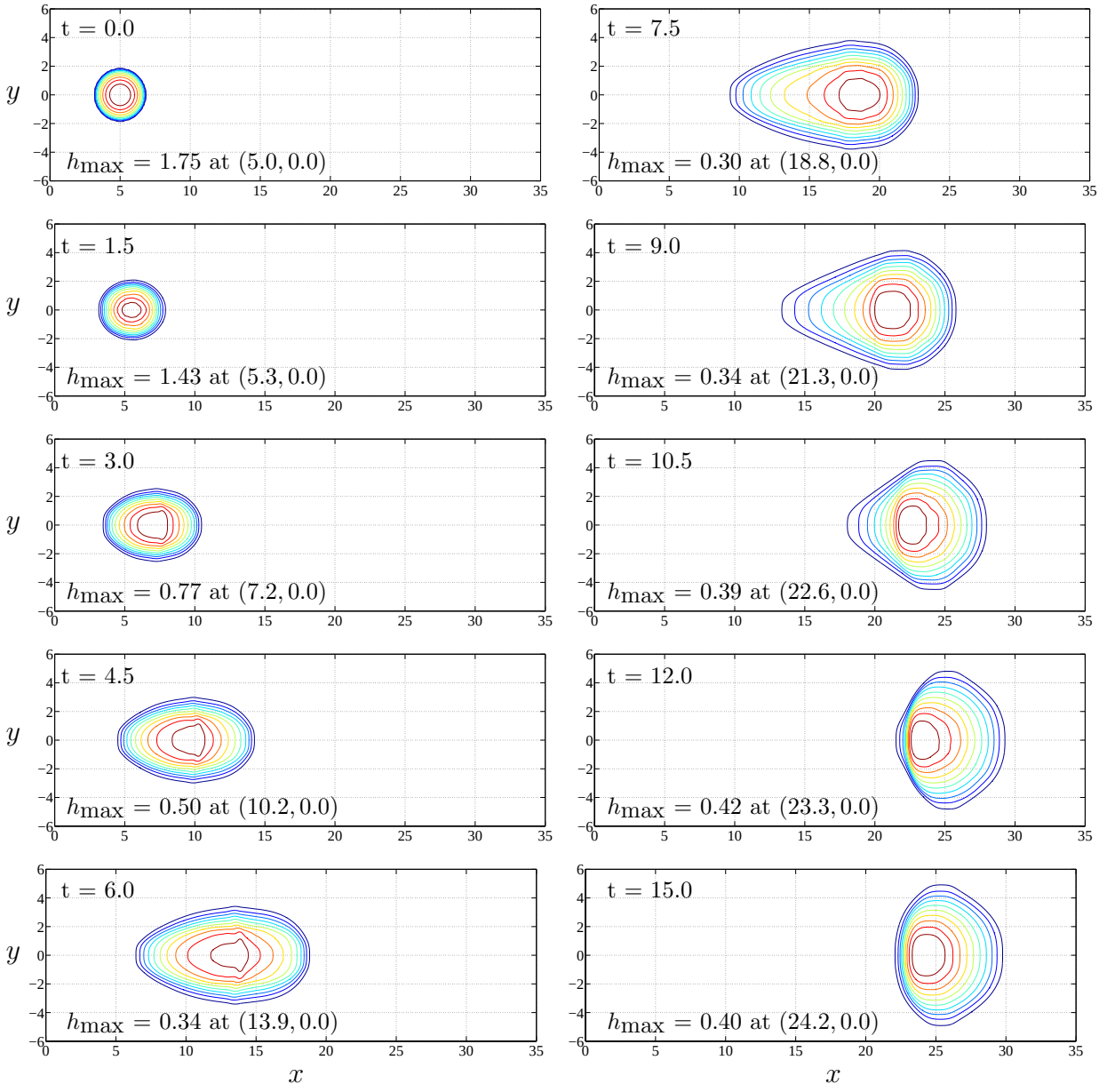

Figure 8.14: Same as in Fig. 8.13 but with the zero lateral curvature

is flat laterally). These comparisons thus demonstrate and highlight the effects of the bed topographies upon the final depositions of the avalanches.

8.3 Superimposed Basal Topography

Until now, we used only the down- and cross-slope coordinates to form a three-dimensionally varying basal topography which is actually just a reference topography. In real applications we need to include local and detailed information about the elevation of the mountain subregion, for instance through GIS digital elevation data. This is usually done by superimposing a basal topography over a reference surface that may be curved or flat both in the lateral- and longitudinal-directions.

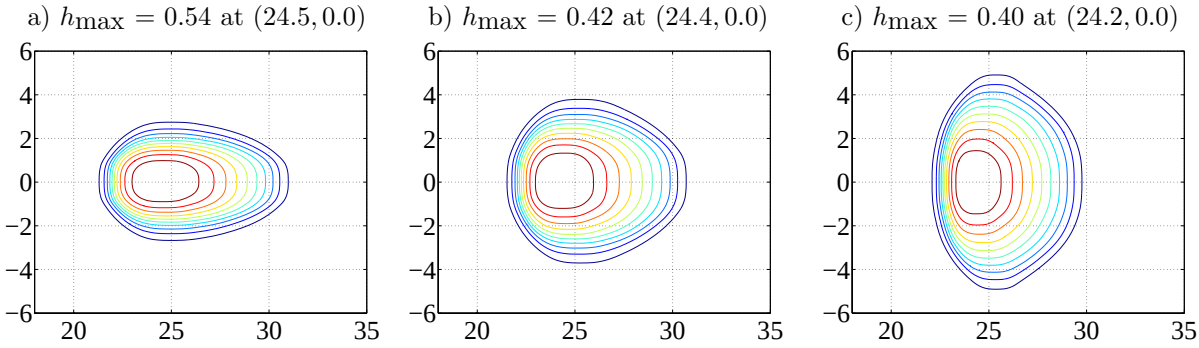

Figure 8.15: Effects of the topographic variation of an avalanche track in the deposits of avalanches: Comparison of the final deposits of an avalanche for a constant cross-slope curvature, $\theta \in (-45°, 45°)$ (left panel, corresponding to Fig. 8.12), a variably flattened bed topography given by (8.5) (middle panel, corresponding to Fig. 8.13) and a completely flat bed topography in the cross-slope direction (right panel, corresponding to Fig. 8.14). The other conditions are exactly the same as explained at the beginning of Section 8.2.2

8.3.1 Laterally Flat Reference Surface

Here, a basal topography varying in the cross-slope direction is considered which is defined by its elevation $b(x, y)$ above a reference surface without lateral variation:

$$b(x, y) = b_0 \left(1 - \cos\left(\frac{\pi}{4}\frac{y}{(B/2)}\right)\right) \sin\tilde{\zeta}(x), \quad \text{for } y \in [-7, 7], \tag{8.6}$$

where $B = 14$ is the width of the computational domain, and multiplication by $\sin\tilde{\zeta}$ ensures that this elevation is smoothly transited from the inclined reference surface (with its maximum) to disappearance on the horizontal run-out plane where the lateral elevation ceases, similar to a basal topography as in Fig. 3.7. The basal topography over which the avalanche flows has a channelling effect on the inclined section of the chute. Two values of b_0, $b_0 = 2$ and $b_0 = 10$, are chosen which correspond to maximum elevations at the lateral boundary of the computational domain on the inclination of the basal surface $b^{\max} = 0.34$ and $b^{\max} = 1.68$, and indicate mean lateral inclinations of 2.8° and 13.5°, respectively. Other parameter values are taken from Section 8.1. Numerical results are depicted in Figs. 8.16 and 8.17. It is surprising that a fairly small lateral curvature can bring obvious influences on avalanche geometries as we can see by comparing Fig. 8.16 (left panel), Fig. 8.17 (upper panels) for $b^{\max} = 0.34$ with Figs. 8.7 and 8.8 for $b^{\max} = 0$, respectively. Comparison of Fig. 8.7 and Fig. 8.17 as well as Fig. 8.8 and Fig. 8.16 shows that partial confinement of the avalanche, in the inclined parabolic-type section of the chute, prevents lateral spreading and strongly channelises the flow. With the increase in the lateral inclination granular materials tend to accumulate around the talweg as a result of the lateral channelling. Consequently, the granular flow becomes thicker and longer along the talweg.

It should be pointed out that the Savage-Hutter equations (3.18)-(3.23) described in Chapter 3 are only suitable for a shallow topographic elevation $b = b(x, y)$ above the reference surface $z = 0$. This reference surface (or equivalently the downslope inclination angle $\tilde{\zeta}$) changes only as a function of the downslope coordinate x and there is no lateral variation in the cross-slope y-direction. For a large lateral variation of the basal topography

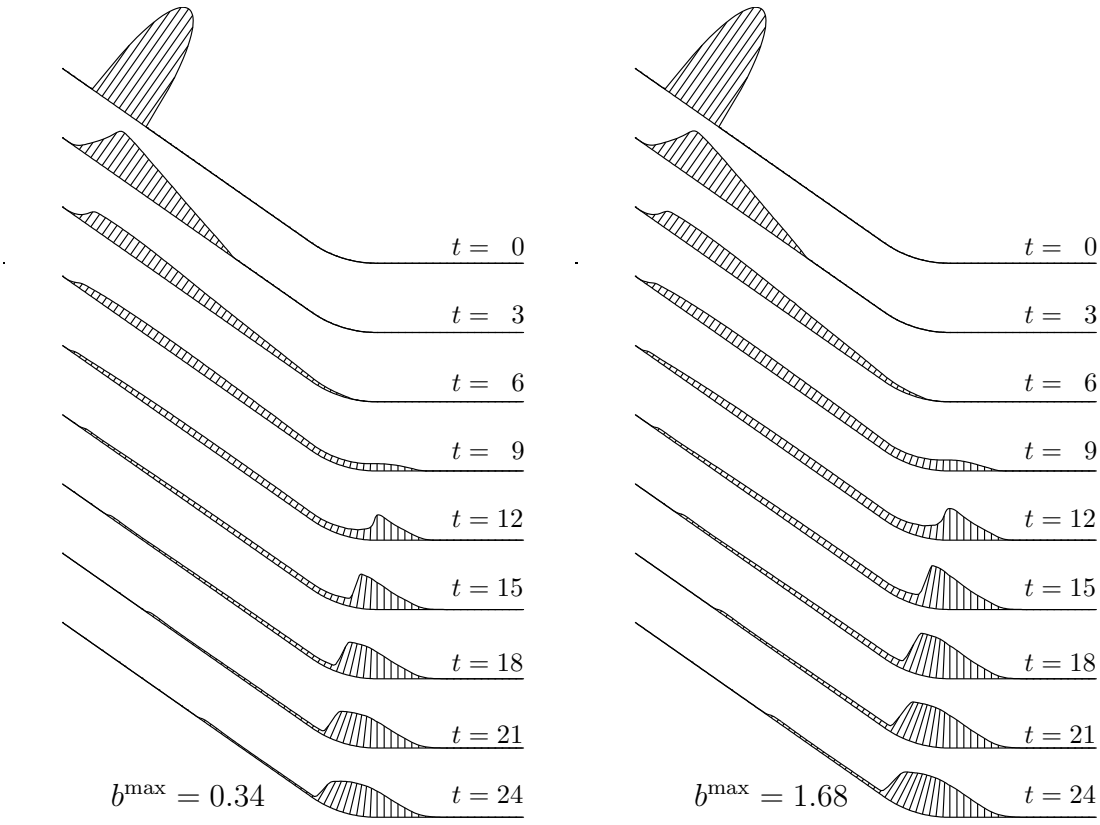

Figure 8.16: Avalanche thickness along the central line of the flow, $y = 0$, at different dimensionless times. The bottom topography varies in the cross-slope direction according to (8.6) with $b_0 = 2$ (left panel), corresponding to a maximum dimensionless elevation $b^{\max} = 0.34$ at the lateral boundaries $y = \pm 7$ within the top inclined region, and $b_0 = 10$ (right panel), corresponding to $b^{\max} = 1.68$

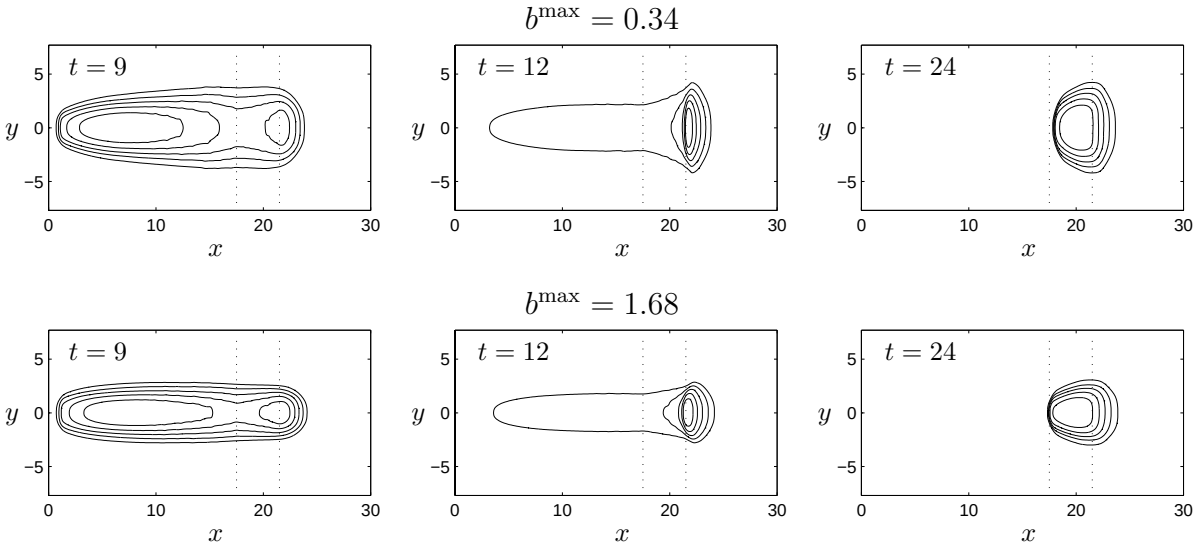

Figure 8.17: Thickness contours of the avalanche at three different dimensionless times $t = 9$, 12, 24. The bottom topography varies in the cross-slope direction according to (8.6) with $b_0 = 2$ (upper panels), corresponding to a maximum dimensionless elevation $b^{\max} = 0.34$ at the lateral boundaries $y = \pm 7$ within the top inclined region, and $b_0 = 10$ (lower panels), corresponding to $b^{\max} = 1.68$

an extended Savage-Hutter theory (equations (4.85)-(4.87)) for rapid shear flows of dry granular masses proposed by PUDASAINI & HUTTER [101] is more suitable, in which the talwegs may be arbitrarily curved and twisted, and the channel geometry may equally be arbitrary.

8.3.2 Laterally Curved Reference Surface

Here we will superimpose a basal topography over a laterally curved reference surface. At this point we would like to demonstrate the effect of the cross-slope component of the gravitational acceleration even in the case of superimposed basal topography. We believe that the gradient of the superimposed basal topography appearing in the last term of the net driving force component s_y in the cross-slope direction alone is not able to correctly include the actual force and that we must incorporate the cross-slope component of the gravitational acceleration g_y, as we have included in the model equations (4.85)-(4.87). The main reason for this is that the term $\varepsilon g_z \, (\partial b/\partial y)$, which appears in the model equation through the kinematic boundary condition and the depth-integration process, includes only the local effect of the topography. There must be some term that represents the global characteristic of the coordinate system and the topography, i.e., g_y. Otherwise, the granular mass will, in the cross slope direction, either be over spread or under spread. Therefore, we must simultaneously incorporate these two terms in order to correctly balance the effect of gravitational acceleration. However, the intensity of such effects must be checked by performing laboratory experiments over laterally curved surfaces to judge the validity of these claims.

Figure 8.18 represents a comparison of the deposits ($t = 24$) of the avalanche sliding over the superimposed basal topography described by (8.6) over a curved reference surface for which the value of $\theta = 14^\circ$ corresponding to $z_T = 30$. All parameter values and other conditions are as in Section 8.3.1 with $b_0 = 10$. The left panel of this figure represents the contours of the deposit of the avalanche for which the lateral component of the gravity force, i.e. g_y, is incorporated. On the other hand, the right panel represents the deposit without g_y. As we can clearly see, there is a big difference in the deposited masses and the run-out areas in these two cases. The right panel underpredicts the lateral spreading of the deposit, as discussed in the last section (see Fig. 8.17), while the left panel corrects this lacking. It must be checked by experiments, whether or not such a large difference occurs in reality.

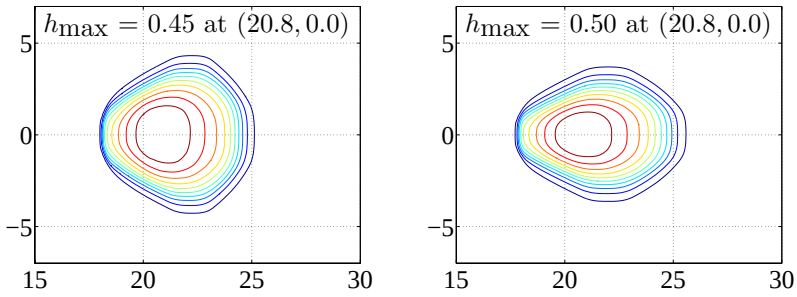

Figure 8.18: Effects of the lateral component of the gravity: The left panel represents the deposit of an avalanche over a superimposed channel described by (8.6) over a cylindrically curved (down-hill) channel together with the lateral gravity component. The right panel presents the deposit without the lateral component of the gravitational acceleration

8.4 Avalanches Down Curved and Twisted Channels

Our main intention while developing the avalanche theory in Chapter 4 was to be able to include the simultaneous effects of the curvature and torsion in the dynamics of an avalanching mass over generally curved and twisted mountain topography. One might expect that there must be not only the effect of curvature but equally also that of torsion on the entire dynamics and the deposit of an avalanche when it slides down over a curved and twisted natural terrain. The model equations (4.85)-(4.87) should be able to predict the flow of an avalanche over a non-uniformally curved and twisted channel in which the cross-slope curvature (or the channel width) may equally be varying. This section is devoted to the numerical simulations, their physical explanations and analysis over such topographic configurations. The main target is the analysis of the joint effects of curvature, torsion, cross-slope curvature (i.e., the channel width) and the "centrifugal" force in the dynamics of the avalanching body down more general channels and topographies. This is an *entirely new aspect* in the field of avalanche research. On the one hand, the simulations, which we are going to present in the sequel, will *disclose the unknown physics* and will discover some fundamental insights of the avalanches, and thus allows us to judge about the applicability of the new-model equations that we have presented in Chapter 4. On the other hand, they will open a wide spectrum of possibilities for the practitioners involved in the hazard mapping, risk management and public safety. This, then leads to the implementation of our theory to realistic mountain topography together with GIS elevation data of some specific mountain sub-regions.

8.4.1 Flows Through Uniformly Curved and Twisted Channels

As an example, we consider a helically curved and twisted channel. On the one hand, this is an academic *test example* that can be (relatively) easily verified by some laboratory experiments. On the other hand, as discussed at the beginning of Chapter 5, there are many industrial applications of granular flows in process engineering scenarios where such flow configurations are practically used. For this reason, we consider a *helix* as a master curve so as to form a helically curved and twisted channel.

Let us consider a circular helix described by

$$\mathbf{R}(\vartheta) = (A\cos\vartheta, A\sin\vartheta, -B\vartheta)\,, \tag{8.7}$$

where ϑ is the azimuthal angle. The arc length, curvature, torsion and pitch of the helix are given by

$$x = \left(A^2+B^2\right)^{1/2}\vartheta, \quad \kappa = A/\left(A^2+B^2\right), \quad \tau = -B/\left(A^2+B^2\right), \quad \mathcal{P} = 2\pi B, \tag{8.8}$$

respectively. Based on the master curve (8.7) we form a helically curved and twisted channel as in Subsection 8.2.1. Since the channel is curved and twisted, we must observe the effects of curvature and torsion in the dynamics of the avalanche. We may expect that the flowing granular mass will deviate continuously outward from the central line (i.e., the talweg) of the channel due to the "centrifugal" force.

Figure 8.20 displays avalanche contours of an avalanche sliding down through a helically curved and twisted channel (see Fig. 8.19 (a)) with uniform curvature and torsion given

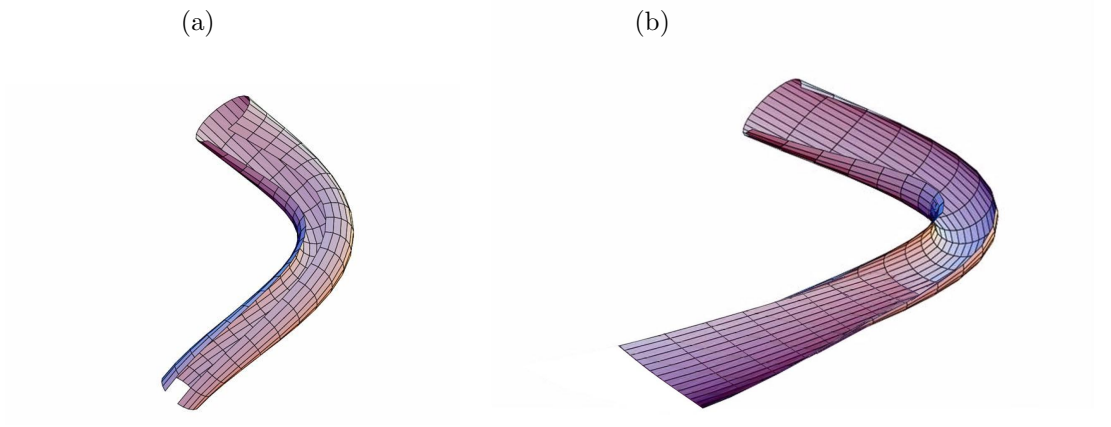

Figure 8.19: (a) Helically curved and twisted channel with uniform curvature and torsion. (b) Curved and twisted channel with a helical talweg. The channel merges continuously into the flat horizontal run-out zone

by (8.8) and a constant cross-slope channel width*. The parameter values are: $A = 13$, $B = 13$, so that the channel is inclined with the horizontal at 45°; the radius of curvature and torsion are each 26, and the internal and bed friction angles are $\phi = 33°$ and $\delta = 27°$, respectively. The radius of curvature in the cross-slope direction is $z_T = 96$. The mass held by a hemi-spherical cap centered at $(23, 0)$ with radius 6.5 is suddenly released with zero initial velocity. These contours are plotted at the time steps $12, 18, 24, 29, 31, 33$, respectively. To clearly observe the effects of curvature, torsion and the "centrifugal" force we either need to use a relatively large mass or a long channel. Here we consider a relatively small mass and a long channel. Until time level $t = 12$ we do not clearly see the effects of curvature, torsion and the centrifugal force. However, note that, if larger masses are used, one can easily see the effects of these factors from the early phase of the motion. After time $t = 12$ the effects of these parameters can very clearly be seen. As time elapses, the avalanching mass is getting less spread laterally, but, it is rapidly moving outwards from the center line of the channel. The speed of the front is much larger than the speed of the tail. This means that the body is accelerating rapidly down- and out-ward of the talweg of the channel. Such behaviour of the deforming mass is the joint effect of the curvature, torsion, and the "centrifugal" force that is modelled in the theory (equations (4.85)-(4.90)) through the gravitational acceleration components g_x, g_y, g_z and the net driving force components s_x, s_y, which include the curvature and torsion of the master curve, bed topography and the cross-slope curvature of the channel. The mass is always extending and accelerating in the down-slope direction, because the channel does not contain the transition- and run-out-zones. In the sequel, we will deal with the cases in which the transition and run-out zones are included in the geometrical part of the model.

*All figures shown for helical chutes are geometrically distorted. The graphs are vertical projections of the chute and granular heaps whose circular-annular geometry are stretched to become straight. Thus, a segment of the annular ring becomes a rectangle of which the top edge is the chute outside and the bottom edge the chute inside boundary. This graphical representation is chosen because it is considered to be relatively easy to program.

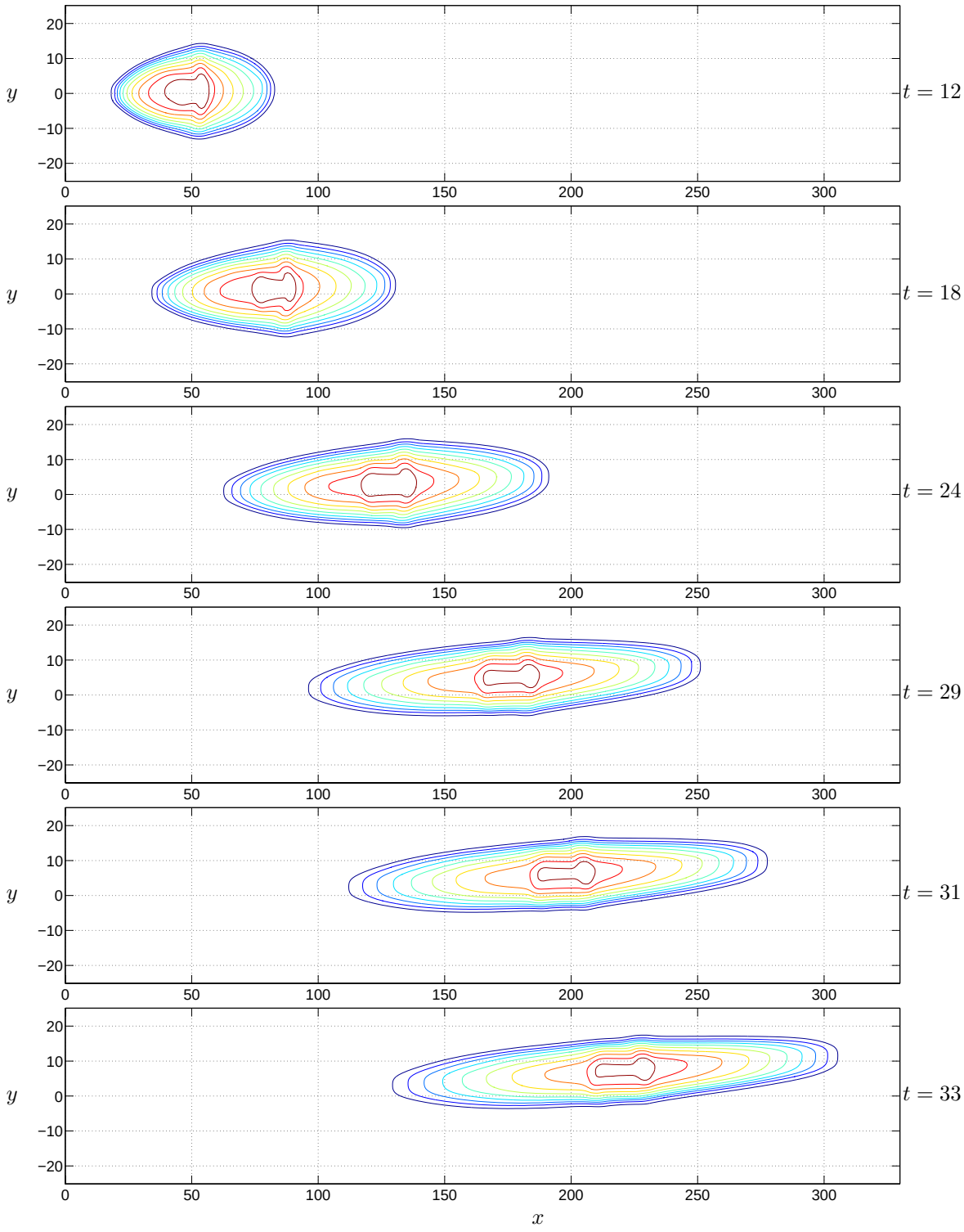

Figure 8.20: Avalanche motion in a helically curved and twisted channel with uniform curvature and torsion and a constant cross-slope channel width. Parameter values: the radius of curvature and torsion are 26, the internal and bed friction angles are $\phi = 33°$ and $\delta = 27°$, respectively. The mass held by a hemi-spherical cap centered at $(23, 0)$ with radius 6.5 is suddenly released with zero initial velocity. These contours are plotted at the time slices $12, 18, 24, 29, 31, 33$, respectively. All quantities are non-dimensional

8.4.2 Avalanching Flows Through Non-Uniformly Curved and Twisted Channels

In reality not all channels are uniformly curved and twisted. Now we march into more complicated situations which deal with non-uniformly curved and twisted channels. Another interesting item is the final deposit. To achieve a mass to be deposited we must be able to include the run-out zone into the geometric part of the model. In this section we will present avalanche simulations through different channels with different run-out zones.

(I) Variable Pitch

One geometric model is such that the pitch defined in (8.8) can be modified as

$$B(x) = \begin{cases} B_0, & 0 \le x \le x_l, \\ B_0\left(\dfrac{x_r - x}{x_r - x_l}\right)^2, & x_l \le x \le x_r, \\ 0, & x \ge x_r, \end{cases} \tag{8.9}$$

so that prior to the left end point, x_l, of the continuous transition zone, the chute is exactly the same as that used in the previous sub-Section. There is a continuous decrease of the pitch from x_l to the right end point, x_r, of the continuous transition of the channel. Then, for $x \ge x_r$ the pitch is always zero, and thus, the subsequent channel is forming a channelised run-out zone.

Avalanche simulations, for this case, are presented in Fig. 8.21. Chosen parameter values are as in Fig. 8.20, only the channel length and the width are increased in order to capture the entire motion, and $B_0 = 13, x_l = 300$ and $x_r = 500$. The first panel corresponds to the last panel of Fig. 8.20. Therefore, the deformation is presented mainly after the avalanche enters into the transition zone. This figure discloses rather interesting results. Since the pitch of the channel is continuously decreasing from x_l, from the third panel (i.e., $t = 43$) onward, the granular mass tends to turn smoothly towards the central line of the channel. Corresponding to the decrease of the pitch, the inclination angle of the chute with the horizontal plane is also continuously decreasing. Ultimately, the channel merges (approximately) into a horizontal circularly curved channel, thus forming a gully-type channelised run-out zone. After $t = 33$ the sidewise pressure from the channelised bed topography exceeds the radial acceleration. This leads to a continuous rotation of the body towards the center of the channel. The sidewise pressure is so strong that after $t = 63$ the mass crosses the talweg of the channel and heads towards the opposite side of the channel. Finally, the body comes to rest at time $t = 75$.

(II) Variable Curvature and Torsion

As a next geometrical model, consider a channel of which curvature and torsion are redefined with the new expression for A in (8.8) as

$$A(x) = \begin{cases} A_0, & 0 \le x \le x_l, \\ A_0 \exp[(x - x_l)^a], & x_l \le x \le x_r, \\ A_0 \exp[(x_r - x_l)^a], & x \ge x_r, \end{cases} \tag{8.10}$$

where a is an exponent that determines the intensity of decrease of the curvature and

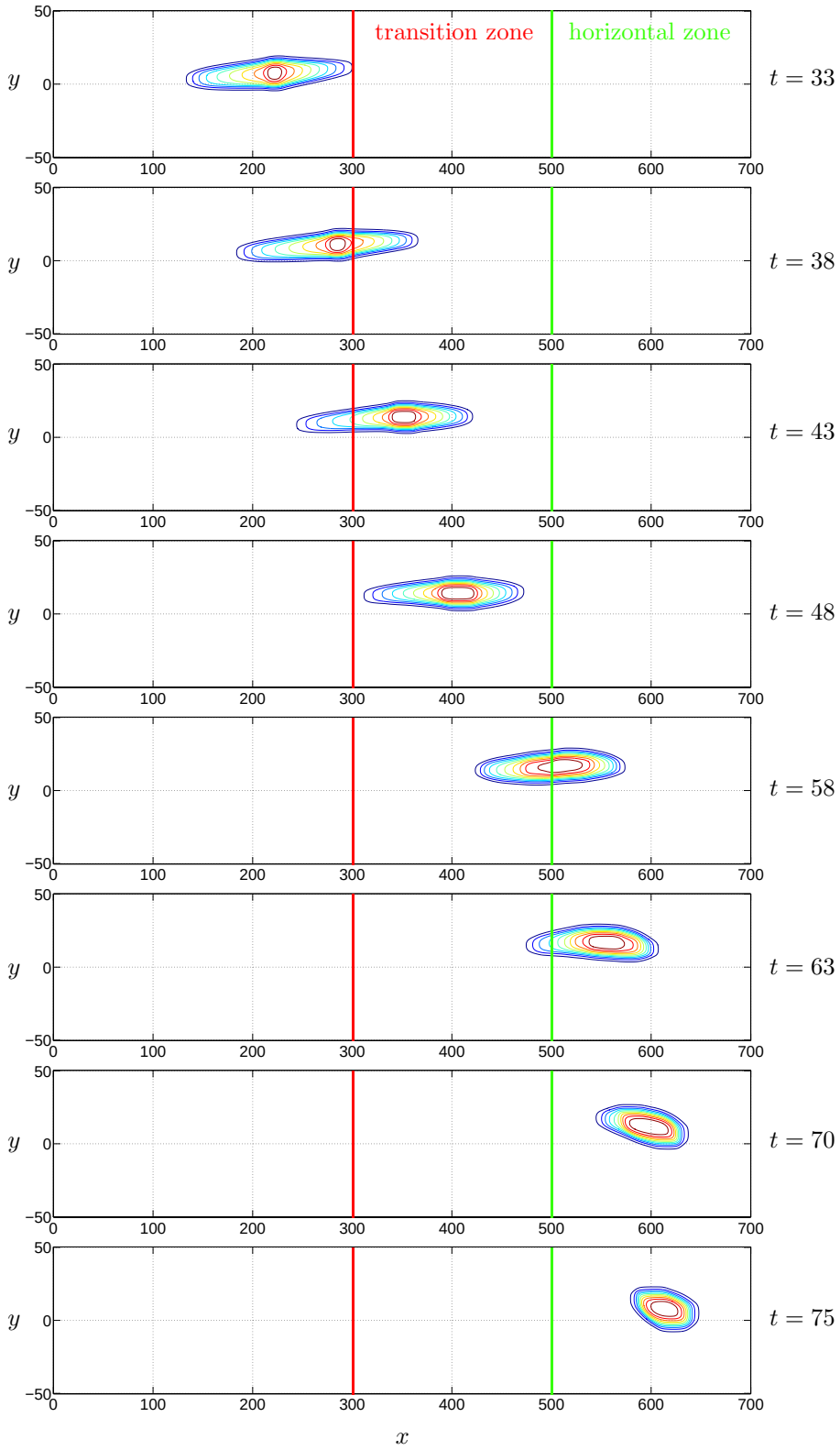

Figure 8.21: Avalanche motion in a helically curved and twisted channel with variable pitch and a constant cross-slope channel width. Parameter values: the internal and bed friction angles are $\phi = 33°$ and $\delta = 27°$, respectively. The mass, held by a hemi-spherical cap centered at $(23, 0)$ with radius 6.5, is suddenly released with zero initial velocity. Contour lines are plotted at the time steps $33, 38, 43, 48, 58, 63, 70, 75$, respectively. The transition zone lies between $x_l = 300$ and $x_r = 500$

torsion. For the simulation, we have set $a = 1$. The other parameters are the same as before with $A_0 = 13$. Equation (8.10) tells us that the radius of the curvature and the torsion of the channel increase rapidly as the arc-length x becomes larger than x_l. Before this transition point, the channel has uniform radius of curvature, torsion and pitch as in the case of variable pitch, (I). This increase of the radius of the curvature and torsion forces the channel quickly to merge (approximately) into an increasingly less curved horizontal channel. This horizontal portion of the channel also forms the run-out zone for the avalanche.

The results of the avalanche simulation for this geometric configuration are presented in Fig. 8.22. There is a great difference in the avalanche motion between Figs. 8.21 and 8.22, specially in the run-out zones. For the present case, since the radius of curvature and torsion increase rapidly from $x = x_l$, the avalanche quickly turns back to the central line of the channel and suddenly comes to rest, much earlier than in Fig. 8.21.

Scrutiny shows that the differences manifest themselves for $t > 48$. In particular, for $t = 58$, the pile in Fig. 8.21 has left the transition zone by more that half of its mass, whereas it is still (almost) inside the transition zone in Fig. 8.22. This can physically be logically understood: The increasing curvature of the channel axis in the transition zone for case (II) effectively reduces the local slope angle of the channel axis much faster than for case (I), so that within the transition zone of case (II) the avalanching mass encounters deposition-prone conditions quicker than in case (I). Comparing the deposits for $t \geq 58$ in the two figures shows that the run-out distance of the avalanche mass is substantially affected.

(III) Decreasing Pitch and Variable Channel Width

In reality, the channels used for the transportation of granular materials in process engineering, or the topographies of mountain terrains may be diverging or converging (with respect to its channel width or cross-slope curvature) as one moves along the down-hill direction. Therefore, the avalanche theory must be able to deal with more general channels and natural valleys or gullies with generally varying cross-slope curvature. At this point, we simulate the avalanche motion in a channel of which the pitch is defined by (8.9), as in the case (I), but, this time, we vary the channel width starting from its transition point from which the pitch starts to decrease. This can be achieved by defining a channel which merges continuously into an open flat run-out zone according to

$$\theta(x,y) = \begin{cases} \dfrac{y}{z_T}, & 0 \leq x \leq x_l, \\ \dfrac{y}{z_T} f(x), & x_l \leq x \leq x_r, \\ 0^\circ, & x \geq x_r, \end{cases} \tag{8.11}$$

where z_T is the distance between the master curve and the talweg in the upper inclined part of the channel (hence a constant) and $f(x) = \left(1 - (x - x_l) / (x_r - x_l)\right)^2$. Thus, the continuous transition of the parameter θ from its higher value (y/z_T) in the upper part to its zero value in the open run-out zone constitutes a required three-dimensional channel which has variable pitch and variable curvature both in the longitudinal as well as in the lateral direction.

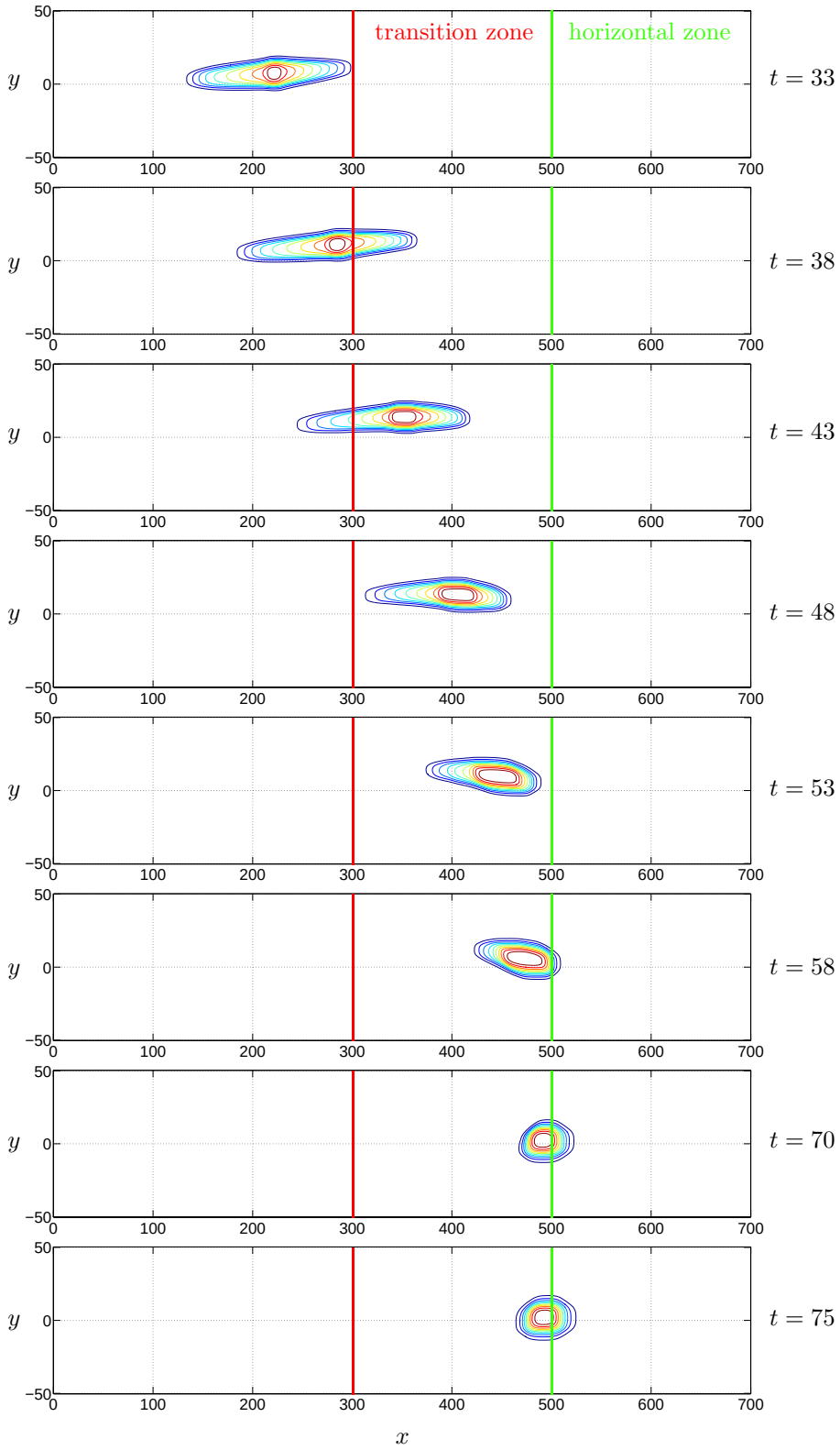

Figure 8.22: Avalanche motion in a "helically" curved and twisted channel with decreasing curvature and torsion and a constant cross-slope channel width. Parameter values: the radius of curvature and the torsion are given by formulae (8.8) and (8.10), the internal and bed friction angles are $\phi = 33°$ and $\delta = 27°$, respectively. These contours are plotted at the time steps $33, 38, 43, 48, 53, 58, 70, 75$. The transition zone lies between $x_l = 300$ and $x_r = 500$

Figure 8.23 depicts the contours of the avalanche motion from its transition to the open run-out zone. The graphs describe the *fantastic* and *fascinating* deformation of the avalanche. Although the pitch is decreasing, after reaching the transition zone the avalanching body is heading radially outwards of the flat run-out zone until it comes to rest and finally deposited in a corner of the chute. The main mechanism for this is that, as soon as the mass enters the run-out zone the radial acceleration decreases rapidly, but, since the chute is flattening in the cross-slope direction, the inherent radial acceleration must drive the mass radially out-ward in the horizontal flat plane. The direction of motion and the process of the deposition is in conformity with our physical intuition and expectation.

(IV) Decreasing Curvature and Torsion, and Variable Channel Width

A further interesting and important geometrical model would be a channel whose radius of curvature and torsion increase from the beginning of the continuous transition zone as described by equation (8.10) and that the channel is opened continuously and merges into the horizontal plane as described by (8.11). This case is more important in the geophysical applications because the radius of curvature and torsion generally increases as one enters into the run-out zone of a mountain valley, see Fig. 8.19b.

The avalanching motion from the transition to the run-out zone in such a channel is presented in Fig. 8.24. The principal mechanism for the deformation and the deposition of the mass is analogous to case (III) (i.e., Fig. 8.23), but it stops quite earlier in time and at a shorter run-out distances than before. Given the results of cases I and II, this was to be expected. In the last two panels of Figs. 8.23 and 8.24, we also observe the formation of upward moving shocks.

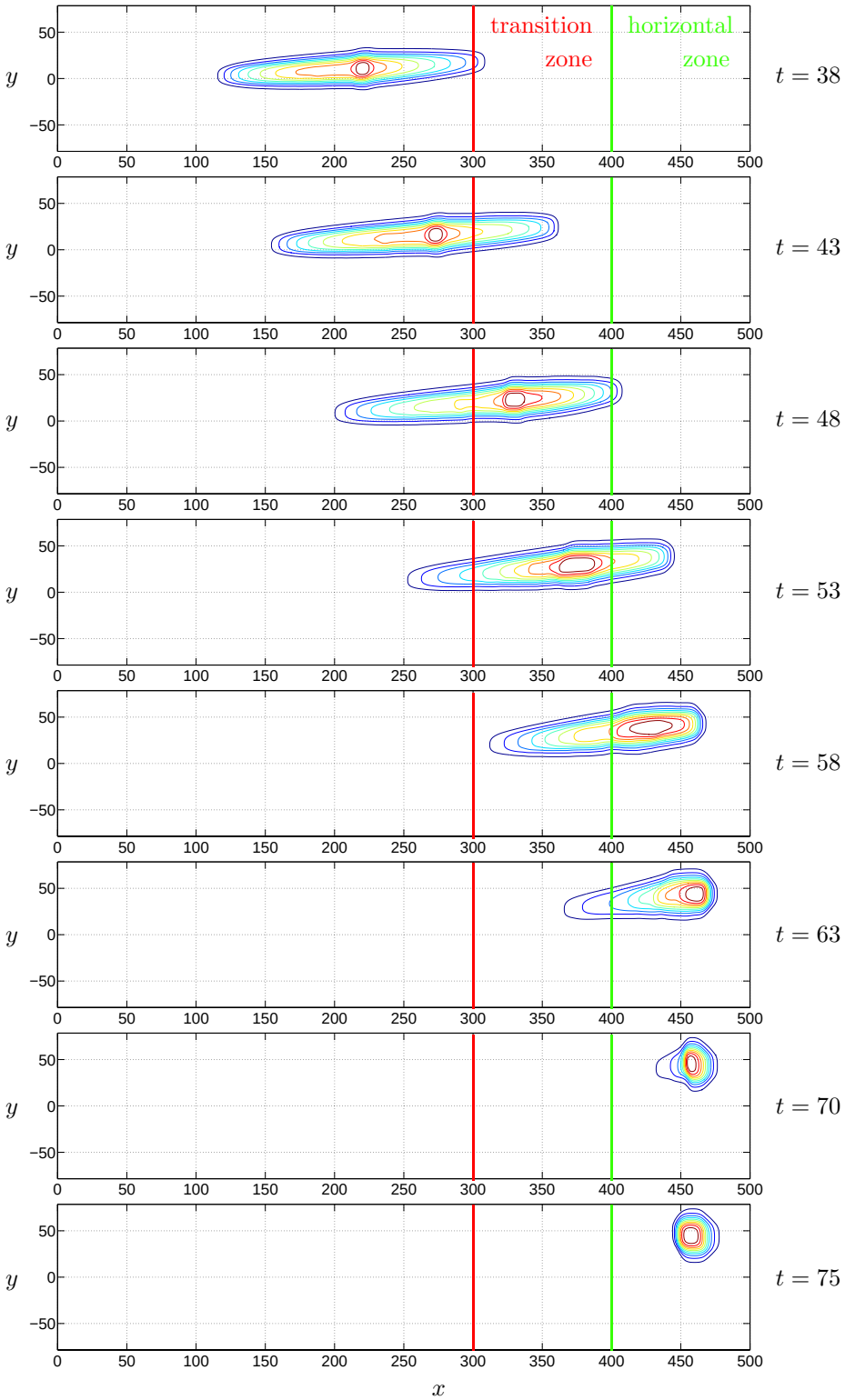

Figure 8.23: Avalanche motion in a "helically" curved and twisted channel with decreasing pitch and increasing cross-slope channel width. Parameter values: The radius of curvature and torsion is given by formulae (8.8), (8.9) and (8.11), the internal and bed friction angles are $\phi = 33°$ and $\delta = 27°$, respectively. These contours are plotted for the time steps $38, 43, 48, 53, 58, 63, 70, 75$. The transition zone lies between $x_l = 300$ and $x_r = 400$

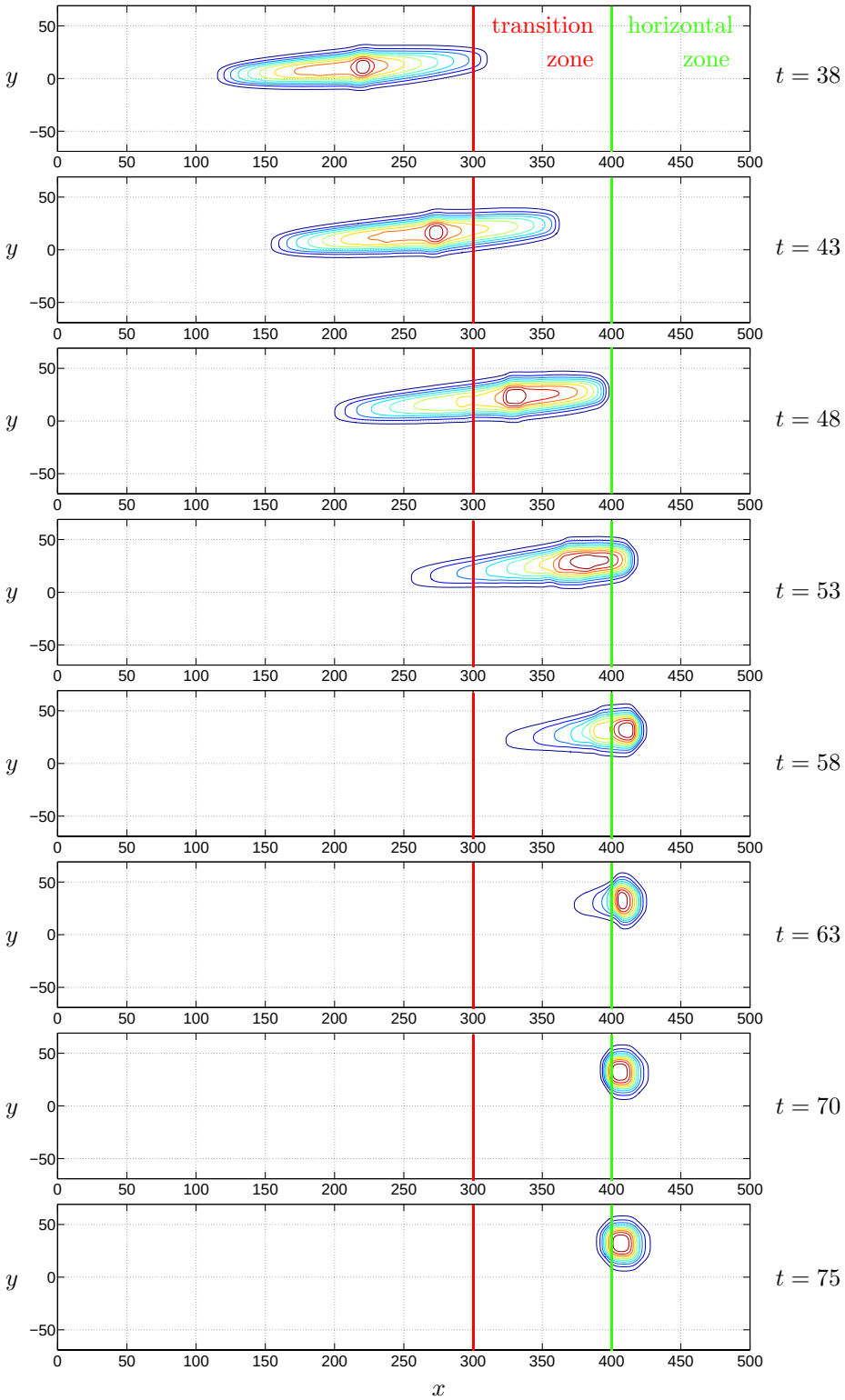

Figure 8.24: Avalanche motion in a "helically" curved and twisted channel with decreasing curvature and torsion and increasing cross-slope channel width. Parameter values: The radius of curvature and torsion is given by formulae (8.8), (8.10), and (8.11), the internal and bed friction angles are $\phi = 33°$ and $\delta = 27°$, respectively. These contours are plotted at the time steps $38, 43, 48, 53, 58, 63, 70, 75$, respectively. The transition zone lies between $x_l = 300$ and $x_r = 400$

8.5 Sensitivity to Phenomenological Parameters

In the last sections the numerical results of the various schemes were compared with respect to different topographies. In this section we will closely investigate the effects of various values of the internal and bed friction angles.

Internal and Bed Friction Angles

In Figs. 8.25 and 8.26 the sensitivity of the extended Savage-Hutter equations to the internal angle of friction, ϕ, and the bed friction angle, δ, in avalanche flows is examined by depicting the evolutions of the avalanching body at various dimensionless time points in a vertical plane along the central line of the flow. The topographic description and other parameters are as in Section 8.1.1. Comparing the numerical results for $\phi = 30°$ (the left panels), $\phi = 32°$ (the middle panels) and $\phi = 37°$ (the right panels) of Fig. 8.25, shows that the avalanche flow is robust against variations of the internal angle of friction. In contrast, the geometries of the avalanching bodies are fairly sensitive to variations of the bed friction angle, as shown by comparing the numerical results for $\delta = 30°$, $\delta = 28°$ and $\delta = 23°$, respectively, in Fig. 8.26. With the decrease of the bed friction angle, the granular body becomes more fluidised. Consequently, the run-out zone is larger and the deposit becomes shallower than for deposits obtained with large values of the bed friction angle. From these simulations we draw the following conclusion: although the geometry and the shape of the deposit of an avalanche depend also on the internal angle of friction the fluidity of the sliding mass is very sensitive to the change of the bed friction angle. This means that we must be very careful when supplying the correct bed friction angle as an input parameter of the model. Otherwise, the computed results are less reliable in comparison to the reality.

8.6 Pressure Dependence of the Friction Angles

A pressure dependence of the internal angle of friction is known to represent the *quantification* of the *pore space* dependence of the internal friction [70]. Such a dependence has also been observed in wall friction experiments for the bed friction angle [92, 123]. So, we must assume $\delta = \delta(p)$ and $\phi = \phi(p)$, where p is the pressure. However, since the SH-theory has only manifested a weak dependence of the avalanche geometry on the values of ϕ as demonstrated in Section 8.5, we shall ignore a pressure dependence of ϕ, so $\phi = const.$ Experiments indicate a decrease of the bed friction angle with pressure [70, 92, 123], the simplest parameterisation is linear and we choose [103]

$$\delta = \delta_0 - \frac{\delta_0 - \delta_1}{p_1} p, \tag{8.12}$$

in which δ_0 is the pressure independent bed friction angle and δ_1 is its value at $p = p_1$. Scaling p and p_1 according to

$$p = \varrho g[H]\hat{p}, \quad p_1 = \varrho g[H_1], \tag{8.13}$$

equation (8.12) takes the form

$$\delta = \delta_0 \left\{ 1 - \frac{[H]}{[H_1]} \frac{\delta_0 - \delta_1}{\delta_0} \hat{p} \right\}, \tag{8.14}$$

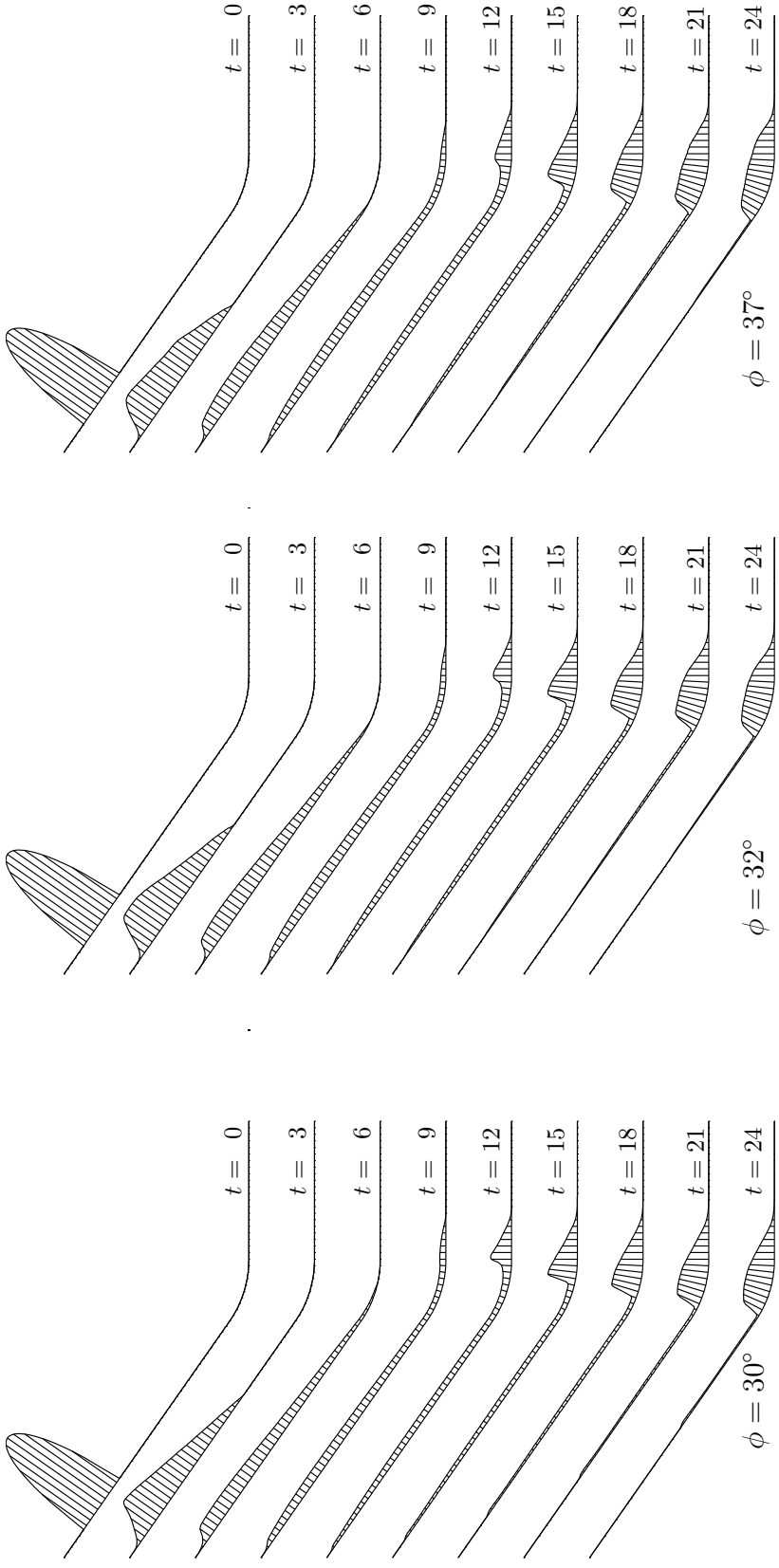

Figure 8.25: Avalanche thickness along the central line of the flow, $y = 0$, at different dimensionless times $t = 0$, 3, 6, 9, 12, 15, 18, 21, 24 for three different internal friction angle ϕ: $\phi = 30°$ (left), $\phi = 32°$ (middle) and $\phi = 37°$ (right). The bottom friction angle remains unchanged, i.e., $\delta = 30°$

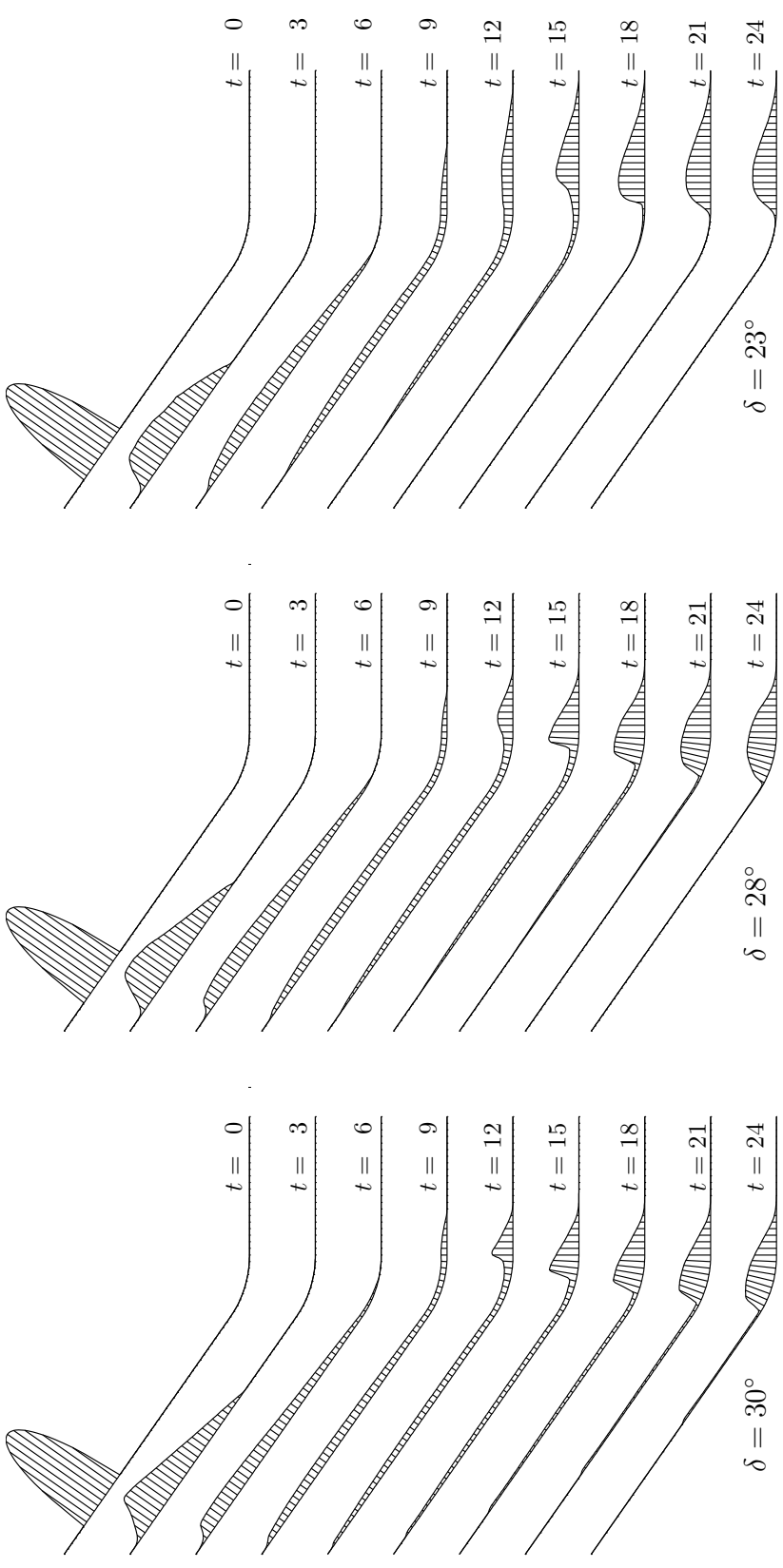

Figure 8.26: Avalanche thickness along the central line of the flow, $y = 0$, at different dimensionless times $t = 0$, 3, 6, 9, 12, 15, 18, 21, 24 for three different bottom friction angle δ: $\delta = 30°$ (left), $\delta = 28°$ (middle) and $\delta = 23°$ (right). The internal friction angle remains unchanged, i.e., $\phi = 30°$

in which $\hat{p}$ at the base

$$\hat{p} = \left(-g_z + \lambda\kappa\eta u^2\right) h \tag{8.15}$$

is the dimensionless pressure. Formula (8.14) is remarkable in the following respect: the pressure dependent term is not scale invariant because it involves the factor $[H]/[H_1]$. We shall choose the following notation and study its influence upon the avalanche motion

$$\Pi = \frac{[H]}{[H_1]} \frac{\delta_0 - \delta_1}{\delta_0}. \tag{8.16}$$

This parameterisation of the bed friction angle δ destroys the scale invariance of the SH-theory. According to the avalanche dynamicists the avalanche dynamics and the run-out distance must be mass dependent for extremely large natural events, typically larger than 10^6 m^3 in volume. A more detailed experimental study on the pressure dependence of the bed friction angle is presently underway.[†]

8.6.1 Parameter Selection

In order to test the mass-dependence of the dynamics and deposits of the avalanche, we consider an ideal mountain subregion in which the talweg is defined by the slope function (8.2), where $\tilde{\zeta}_0 = 50°$ is the straight upper part of the talweg which merges into a horizontal run-out as shown in Fig. 4.10a, and $x_l = 13$ and $x_r = 17$ are the initial and the final points of the continuous transition. The azimuthal angle $\theta \in [-17.9°, 17.9°]$, which accounts for a (shallow) circular variation (cross-slope curvature) of the bed topography in the lateral direction, and the non-dimensional distance $z_T = 16$ corresponding to $y \in [-5, 5]$, Fig. 4.10b. A hemi-spherical cap with radius $R_0 = 1.85$ holding the granular material in it is placed at $(x_0, y_0) = (5.0, 0.0)$ of the chute and suddenly released. The phenomenological parameters are chosen as $\delta_0 = 27°$ and $\phi = 37°$ which correspond to *Vestolen*, a sort of plastic particles of lens-like shape and 4 mm diameter on *drawing paper*.

8.6.2 Mass Independent Bed Friction Angle

At first, the bed friction angle δ is considered to be pressure independent and δ is assumed to be constant, $\delta = \delta_0 = 27°$ corresponding to $\Pi = 0$ in (8.16). Figure 8.27a depicts the evolution of the avalanching body at 10 non-dimensional time steps in a vertical plane containing the talweg of the valley. The first four panels clearly show that once the cap is opened, the avalanche accelerates and spreads rapidly in the downslope direction due to the channelling effect in the cross-slope direction, the gravity and dilatation. Although the front is descending rapidly, the tail moves a bit upward (second panel) because of the fluidisation of the mass and the support of the material from the down-hill (front) side. At $t = 4$ the front reaches the transition zone and the tail also starts to move downward. At $t = 6$, the front part of the body has fully reached the transition zone. Therefore the mass at the front is contracting due to the effect of the passive earth pressure coefficient, but the mass in the tail is still extending. At $t = 7$, the deposition of the mass starts in the vicinity of the lower part of the transition zone. Owing to the effect of the curvature, the flowing body starts contracting. For $t > 8$, a steep surface (height) gradient starts

[†]We are working with Dr. W. Fellin (Institute for Geotechnique and Tunnel Engineering, University of Innsbruck, Austria) to experimentally determine the pressure dependence of the bed friction angle, δ, for different granular materials and different bed roughnesses.

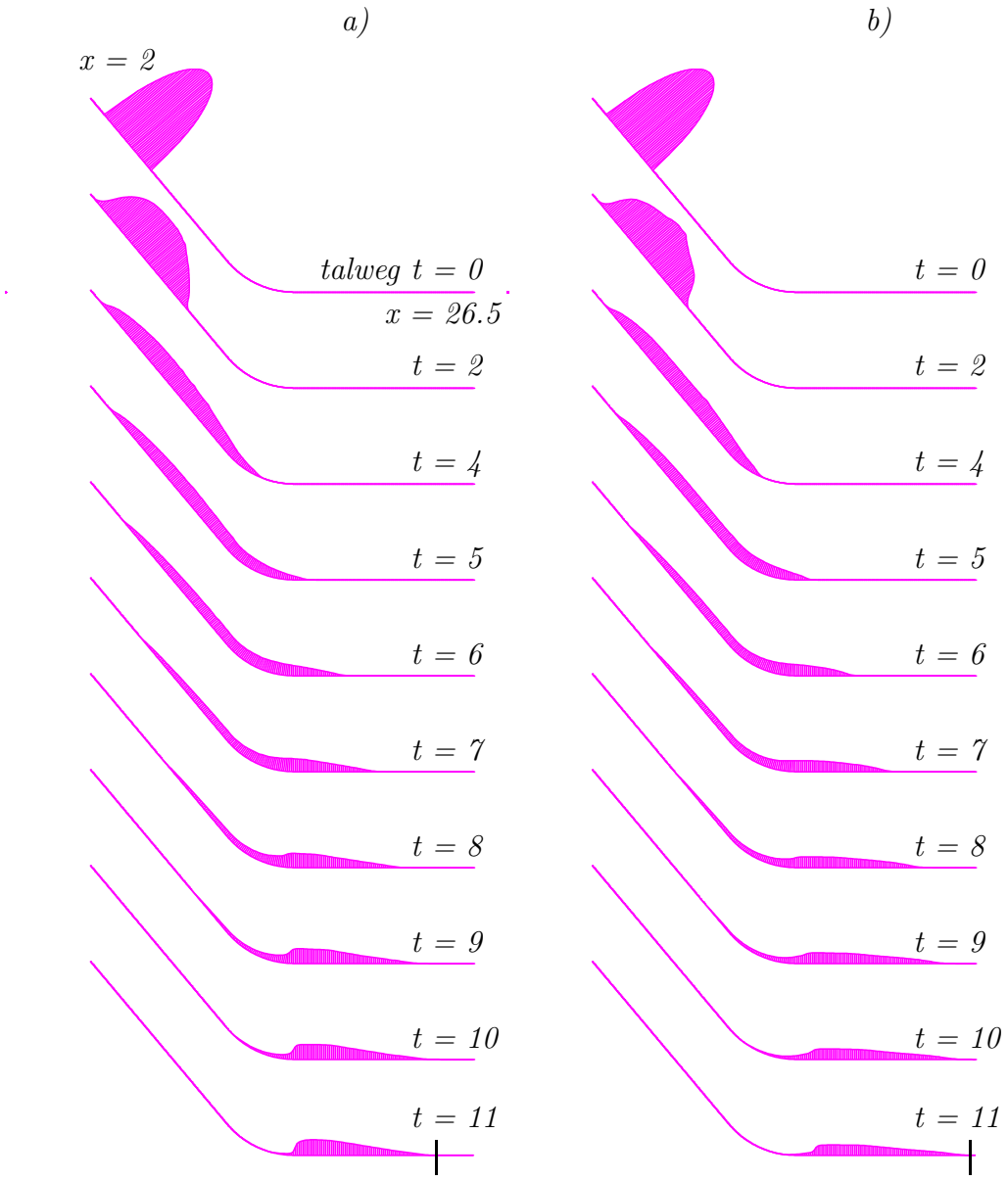

Figure 8.27: a) A series of numerical simulations of avalanche motion with internal and basal friction angles $\phi = 37°$ and $\delta = 27°$, for different time points. The avalanche thickness is plotted using curvilinear coordinate x which runs from left to right along the talweg of length 26.5. We do not explicitly see here the volume preserving of the material since we have plotted only the central section of the avalanche in the vertical plane that contains the talweg. The remaining mass goes in the sidewise direction. b) Same as in a) but with the variable bed friction angle. In this case the avalanche body is more fluidised, the travel distance (indicated by $|$ in the last panels) increases and the height of the deposit decreases considerably

to develop on the tail side of the avalanche. Although the front of the body is almost in stand still the mass from the tail is still continuously flowing down and deposited on the tail side of the body. This leads to the shock front moving upstream. The physical explanation for this is that from the front there is a strong resistive force from the bed which prevents the body from further advecting. So, whatever comes from the upper part of the channel, it must be deposited at the back side of the body. Consequently, the mass body must extend upward. The last four panels show the continuous development of the upcoming shock, while there is no simultaneous motion at the front.

8.6.3 Scale Effects due to the Pressure Dependence of δ

As an example, the value of the parameter Π is taken to be 0.4 which corresponds to the reference values $\delta_1 = 20^\circ$ and $H/H_1 = 1.6$. Figure 8.27b represents a series of numerical results for the same data as in Fig. 8.27a but with the pressure dependent bed friction angle (8.14). The granular body is more fluidised since this angle decreases. Consequently, the run-out distance is larger and the height of the deposit is shallower than for a constant bed friction angle. The last panels indicate that the front of the avalanche for variable bed friction angle is about 20% farther away than for a constant bed friction angle. Similarly, the maximum pile height of the final deposit for variable bed friction angle is about 25% less than in the previous case. These conclusions are also applicable right after the release of the mass, but the comparison is more pronounced as time elapses. Due to the excess fluidity, the formation of the shock is weaker in the last four panels of Fig. 8.27b.

8.7 Applicability of the Extended Theory

So far in this chapter, we presented avalanche simulations over different topographies of which the talweg was curved only in the down-hill direction, or it was curved and twisted in an analytically prescribable way. This means the theory that we developed in Chapter 4, can, in principle, be applied to any kind of topography - from a simply inclined plane to very complicated arbitrarily curved and twisted channels in industrial as well as geophysical flows from initiation to the deposits in the run-out zones.

Similarly, we presented simulations for different phenomenological parameters, for pressure dependent and independent bed friction angles, for flows along the reference surfaces and flows in superimposed channels, for diverging, converging and uniform channels and so on. All these simulations revealed quite reasonable and physically justifiable results for avalanching debris flows of granular materials. Therefore, we may conclude that our theory, which to date is the *most sophisticated and most advanced theory* of flow avalanche dynamics, is able to describe the avalanching motion for diverse situations, mainly with respect to the topography. This thus proves the applicability of the theory under realistic configurations for the flows of granular materials in transportation phenomena in the process engineering and in the geophysical contexts with GIS. More importantly we must compute the functional relations describing the curvature and torsion of the talwegs as well as the function describing the cross-slope geometry of the mountain terrains from GIS digital elevation data. Once this is achieved, we can use our model computer code to simulate avalanching debris down complicated mountain valleys. In this way we serve the purpose of practitioners for hazard mappings and the protection of the life and property of the people.